UNIVERSITY OF CALIFORNIA

Los Angeles

Development of MRI Techniques for Tissue Characterization Using Magnetic Resonance Multitasking

A dissertation submitted in partial satisfaction

of the requirements for the degree

Doctor of Philosophy in Bioengineering

by

Pei Han

2022

ABSTRACT OF THE DISSERTATION

Development of MRI Techniques for Tissue Characterization

Using Magnetic Resonance Multitasking

by

Pei Han

Doctor of Philosophy in Bioengineering

University of California, Los Angeles, 2022

Professor Debiao Li, Chair

Magnetic resonance multitasking (MR Multitasking) is a multi-dimensional imaging framework that was developed recently. With low-rank tensor modeling, signal correlation among images at different time dimensions are exploited in MR Multitasking to resolve motion, accelerate image acquisition, and enhance image quality. Though initially developed for cardiovascular imaging, it has also been extended to many other applications, such as whole-brain multi-parametric mapping, free-breathing abdominal dynamic contrast enhanced imaging, etc. The primary focus of this dissertation is to improve two important MR tissue characterization techniques using MR Multitasking: (1) Electrocardiogram (ECG)-less myocardial T1 and extracellular volume fraction (ECV)

mapping in small animals at 9.4 T, and (2) Fast 3D chemical exchange saturation transfer (CEST) imaging for human studies at 3.0 T.

ECV quantification with cardiovascular magnetic resonance T1 mapping is a powerful tool for the characterization of focal or diffuse myocardial fibrosis. However, it is technically challenging to acquire high-quality T1 and ECV maps in small animals for preclinical research because of high heart rates and high respiration rates. An ECG-less, free-breathing ECV mapping method using MR Multitasking was developed on a 9.4 T small animal MR system. The feasibility of characterizing diffuse myocardial fibrosis was tested in a rat heart failure model with preserved ejection fraction (HFpEF). A 25-min exam, including two 4-min T1 Multitasking scans before and after gadolinium injection, were performed on each rat. It allows a cardiac temporal resolution of 20 ms for a heart rate of ~300 bpm. Elevated ECV found in the HFpEF group is consistent with previous human studies and well correlated with histological data. This technique has the potential to be a viable imaging tool for myocardial tissue characterization in small animal models.

CEST imaging is a non-contrast MRI technique that indirectly detects exchangeable protons in the water pool. It is achieved by performing frequency selective saturation at those protons before acquiring water signal readout. CEST MRI provides a novel contrast mechanism to image important physiological information, such as pH and metabolite concentration. However, long scan time is still a crucial problem in many CEST imaging applications, which makes it difficult to translate current CEST techniques into clinical practice. A novel 3D steady-state CEST method using MR Multitasking was developed in the brain at 3.0 T. This allows the Z-spectrum of 55 frequency offsets to be acquired with whole-brain coverage at 1.7 × 1.7 × 3.0 mm^3 spatial resolution in 5.5 min.

Quantitative CEST maps from multi-pool fitting showed consistent image quality across the volume.

Motion handling in moving organs is another challenge for practical CEST imaging. For instance, breath-holding is currently needed in liver CEST imaging to reduce motion artifacts, which limits not only spatial resolution, but also scan volume coverage. Following the whole-brain CEST protocol, a respiration-resolved 3D abdominal CEST imaging technique using MR Multitasking was developed, which enables whole-liver coverage with free-breathing acquisition. CEST images of 55 frequency offsets with entire-liver coverage and 2.0 x 2.0 x 6.0 mm^3 spatial resolution were generated within 9 min. Both APTw and glycoCEST signals showed high sensitivity between post-fasting and post-meal acquisitions.

The dissertation of Pei Han is approved.

Zhaoyang Fan

Albert M. Thomas

Holden H. Wu

Debiao Li, Committee Chair

University of California, Los Angeles

2022

To my parents

TABLE OF CONTENTS

LIST OF ABBREVIATIONS

Mathematics and Statistics

SD – standard deviation

ICC – intra-class correlation coefficient

CoV – coefficient of variation

LRT – low-rank tensor

SVD – singular value decomposition

HOSVD (MLSVD) – high-order (multilinear) singular value decomposition

Medicine

bpm – beats per minute

cpm – cycles per minute

ECV – extracellular volume

ECG – electrocardiogram

Gd – gadolinium

HCT – hematocrit

LV – left ventricle/left ventricular

GM – gray matter

WM – white matter

HFpEF – heart failure with preserved ejection fraction

GBM – glioblastoma

PDAC – pancreatic ductal adenocarcinoma

Magnetic Resonance Imaging

MRI – magnetic resonance imaging

CMR – cardiovascular magnetic resonance

LGE – late gadolinium enhancement

2D – two-dimensional

3D – three-dimensional

SNR – signal-to-noise ratio

FOV – field of view

ROI – region of interest

B0 – main static magnetic field

B1 – radiofrequency field applied perpendicular to the B0 field

SAR – specific absorption rate

TE – echo time

TR – repetition time

TI – inversion time

FA – flip angle

T1w – T1-weighted

IR – inversion recovery

GRE – gradient echo

EPI – echo planar imaging

FLASH – fast low angle shot

RARE – rapid acquisition with relaxation enhancement

VFA – variable flip angle

MOLLI – modified Look-Locker inversion recovery

SALLI – small animal Look-Locker inversion recovery

SPICE – spectroscopic imaging by exploiting spatiospectral correlation

CAIPIRINHA – controlled aliasing in parallel imaging results in higher acceleration

Chemical Exchange Saturation Transfer

CEST – chemical exchange saturation transfer

ss-CEST – steady-state chemical exchange saturation transfer

APT – amide proton transfer

rNOE – relayed nuclear Overhauser enhancement

DWS – direct water saturation

MT – magnetization transfer

PLOF – polynomial and Lorentzian line-shape fitting

Others

IRB – institutional review board

IACUC – institutional animal care and use committee

LIST OF FIGURES

LIST OF TABLES

ACKNOWLEDGEMENTS

I am most grateful to my PhD advisor Professor Debiao Li, a great scientist in the MRI field, and the best advisor that one can ever expect. I would like to thank him for his overall guidance over the past years. I am fortunate to have been nurtured in such a supportive environment that Professor Li established in the Cedars-Sinai Biomedical Imaging Research Institute (BIRI). Along my PhD journey, he provided me with much freedom to explore the unknown, while he always gave me sharp guidance and warm encouragement when I encountered difficulties. His research philosophy, scientific insights and work attitude have always set high standards for me to pursue, and will benefit my career after my graduation.

I would also like to thank my doctoral committee, Professor Zhaoyang Fan, Professor Albert M. Thomas, and Professor Holden H. Wu, for their valuable advice and instructions on my thesis and defense.

My sincere thanks to the entire group of BIRI, including but not limited to my fellow graduate students (Zhehao Hu, Tianle Cao, Xinheng Zhang, Junzhou Chen, Zihao Chen, Shihan Qiu, Chaowei Wu, Karandeep Cheema, Haoran Sun, and Zengtian Deng), past students (Drs. Zhengwei Zhou, Zixin Deng, Jaime Shaw, Sen Ma, Nan Wang, Yuhua Chen, Eric Johnson, and Xingmin Guan), faculty and scientists (Drs. Zhaoyang Fan, Wafa Tawackoli, Hui Han, Shawn Wagner, Yi Zhang, Anthony G. Christodoulou, Yibin Xie, Randy Yang, Hsu-Lei Lee, and Xianglun Mao), MRI technologists (Laura Smith, Irene Lee, Mike Ngo, Jimmy Fermin, Edward Gill, and Jerry Zink) and supporting staff (Laura Chey, Adis Asaturyan, Cathy Ubaldo-Prado, Rhona Littman, Natalin Aroyan, Eileen Da Vido, Joceline Mota, Joselyn Ricafrente, etc.).

In particular, I would like to thank Dr. Zhengwei Zhou who mentored me during my summer internship in 2016 and my first year of PhD. I would also like to thank Dr. Anthony G. Christodoulou for his guidance on every aspect of MR Multitasking and for all the fruitful discussions on signal processing and image reconstruction algorithms.

Thanks to Dr. Xiaoming Bi and Dr. Fei Han from Siemens Healthineers, who provided me with invaluable support and guidance on Siemens MR pulse sequence programming. I also learned a lot from their perspective in both academia and industry.

Lastly, I would like to express my deepest gratitude to my parents, Shiguang Han and Xiaojie Li, for their consistent support during my PhD and unconditional love throughout my life.

VITA

EDUCATION

- B.S., Engineering Physics (*with Hons.*), Tsinghua University (2017)

JOURNAL PUBLICATIONS

- **Han P**, Cao T, Wang N, et al. Free-breathing 3D CEST MRI of Human Liver at 3.0 T Using MR Multitasking. (In preparation)

- **Han P***, Chen J*, Xiao J, Han F, Hu Z, Yang W, Ling DC, Li D, Christodoulou AG†, Fan Z†. Single projection driven real-time multi-contrast (SPIDERM) MR imaging using pre-learned spatial subspace and linear transformation. *Physics in Medicine & Biology*. (In revision)

- **Han P**, Cheema K, Lee HL, Zhou Z, Cao T, Ma S, Wang N, Han H, Christodoulou AG†, Li D†. Whole-brain steady-state CEST at 3 T using MR Multitasking. *Magnetic resonance in medicine*. 2022 May;87(5):2363-71.

- Li X, Huang S, **Han P**, et al. Nonenhanced chemical exchange saturation transfer cardiac magnetic resonance imaging in patients with amyloid light-chain amyloidosis. *Journal of Magnetic Resonance Imaging*. 2022 Feb;55(2):567-76.

- Pelled G, Salas MM, **Han P**, et al. Intradiscal quantitative chemical exchange saturation transfer MRI signal correlates with discogenic pain in human patients. *Scientific Reports*. 2021 Sep 28;11(1):1-9.

- **Han P***, Zhang R*, Wagner S, Xie Y, Cingolani E, Marban E, Christodoulou AG†, Li D†. Electrocardiogram-less, free-breathing myocardial extracellular volume fraction mapping in small animals at high heart rates using motion-resolved cardiovascular magnetic resonance multitasking: a feasibility study in a heart failure with preserved ejection fraction rat model. *Journal of Cardiovascular Magnetic Resonance*. 2021;23(8):1-11.

- Zhou Z, **Han P**, Zhou B, Christodoulou AG, Shaw JL, Deng Z, Li D. Chemical exchange saturation transfer fingerprinting for exchange rate quantification. *Magnetic resonance in medicine*. 2018 Oct;80(4):1352-63.

AWARDS

- Potchen-Passariello Award Finalist, Society for Magnetic Resonance Angiography (SMRA). 2020.

- 2nd Place for the Best Trainee Abstract Award, International Society of Magnetic Resonance in Medicine (ISMRM). 2020.

- John R. Cameron Young Investigator Competition Finalist, American Association of Physicists in Medicine (AAPM). 2020.

PATENT

- Christodoulou AG, Fan Z, Li D, **Han P**. Systems and methods of on-the-fly generation of 3D dynamic images using a pre-learned spatial subspace. US 63/019,791, issued May 4, 2020.

CHAPTER 1: Introduction

1.1 Motivation

Since its invention in 1970s, Magnetic Resonance Imaging (MRI) has become one of the major medical imaging modalities for non-invasive diagnosis. It can provide both structural and functional information with high-resolution three-dimensional images. The major advantage of MRI is that it offers excellent soft tissue contrast without using any ionizing radiation.

By varying the structure and parameter settings of the MR pulse sequence, images with specific contrasts among different tissues can be generated, which makes MRI a very versatile imaging technique for tissue characterization. For instance, images from the most commonly used T1-weighted and T2-weighted scans are produced by using different TE and TR times. More advanced image contrasts can be generated by performing specific preparation pulses, such as diffusion weighted imaging (DWI), arterial spin labelling (ASL) imaging, and chemical exchange saturation transfer (CEST) imaging, or by injecting contrast agents, such as dynamic susceptibility contrast (DSC) imaging and dynamic contrast enhanced (DCE) imaging. In recent years, research of quantitative MRI methods (such as T1 mapping and T2 mapping protocols) is getting more popular [1, 2]. Unlike conventional qualitative imaging techniques, quantitative parametric maps rather than contrast-weighted images are generated. Those parametric maps can be compared among different imaging sites or different acquisition time points.

Magnetic Resonance Multitasking (MR Multitasking) is a recently proposed imaging framework [3], which uses a low-rank-tensor (LRT) model to exploit the high

correlation among images at different time dimensions (relaxation, motion, etc.), thus can resolve motion and greatly accelerate the acquisition process.

The long-term goal of the dissertation is to improve MRI tissue characterization techniques using MR Multitasking. In this dissertation, we will focus on initial technical development of two important tissue characterization techniques: (1) ECG-free myocardial T1 and ECV mapping in small animals at 9.4 T; (2) Fast 3D CEST imaging for human studies at 3.0 T.

1.2 Aims

Aim 1: To develop an ECG-free myocardial ECV mapping technique in small animals using MR Multitasking to characterize myocardial fibrosis.

Extracellular volume fraction (ECV) quantification with cardiovascular magnetic resonance T1 mapping is a powerful tool for the characterization of focal or diffuse myocardial fibrosis. However, it is technically challenging to acquire high-quality T1 and ECV maps in small animals for preclinical research because of high heart rates and high respiration rates. Therefore, we try to develop an ECG-free T1 and ECV mapping method using MR Multitasking on a 9.4 T small animal MR system.

Aim 2: To develop a fast 3D steady-state CEST imaging method for tissue characterization within a clinically feasible scan time using MR Multitasking.

Conventional CEST imaging, where each image readout is preceded by a frequency selective saturation module with long enough duration to reach the steady state between the exchanging proton pools and the water pool, is usually slow. This makes fast, high-quality 3D CEST imaging quite challenging. Moreover, breath-holding is usually needed when CEST is applied to moving organs such as liver or pancreas. Therefore, we

try to develop a 3D steady-state CEST imaging technique using MR Multitasking to further reduce scan time in brain imaging and to achieve free-breathing acquisition in abdominal imaging.

Aim 2.1: To develop a robust 3D whole-brain steady-state CEST acquisition scheme using MR Multitasking.

We try to develop a fast 3D whole-brain CEST technique using the MR Multitasking framework. No physiological motion is involved in this protocol.

Aim 2.2: To develop a free-breathing 3D abdominal steady-state CEST method of human liver using MR Multitasking.

Based on Aim 2.1, we try to develop a free-breathing 3D abdominal CEST imaging method. This will be the first abdominal CEST protocol with: (1) volumetric coverage, and (2) free-breathing acquisition.

1.3 Structure of the Dissertation

Chapter 2 introduces the background of the work, including principles of magnetic resonance imaging and the MR Multitasking framework. A brief introduction of T1/ECV mapping and CEST imaging—two tissue characterization methods involved in the thesis—are also included.

Chapter 3 describes an ECG-less, free-breathing myocardial T1 and ECV mapping technique in small animals at high heart rates. In this chapter, the proposed technique is validated against the Bruker scanner's built-in T1 mapping method in a phantom. Its feasibility to characterize diffuse myocardial fibrosis in a rat hypertensive heart failure model with preserved ejection fraction (HFpEF) model is tested. The repeatability of ECV quantification is also assessed. (**Aim 1**)

Chapter 4 describes a fast whole-brain steady-state CEST method using MR Multitasking. In this chapter, CEST maps generated from the proposed method are compared with those from conventional 2D single-shot FLASH CEST method in healthy volunteers. The consistency of CEST maps is assessed among different subjects. The intra-session repeatability is also evaluated. (**Aim 2.1**)

Chapter 5 describes a free-breathing 3D abdominal steady-state CEST method using MR Multitasking. In this chapter, the feasibility of the proposed method is tested in healthy volunteers. The sensitivity of APTw and glycoCEST signals generated with the proposed method is tested with fasting experiments. (**Aim 2.2**)

Chapter 6 gives an overall discussion with conclusion and future directions.

CHAPTER 2: Background

2.1 Magnetic resonance multitasking

Magnetic resonance multitasking (MR Multitasking) is a novel imaging framework that initially developed for quantitative multi-parametric cardiovascular imaging [3]. Different sources of image dynamics—both physiological (including cardiac and respiratory motion) and physical (including T1 and T2 relaxation, as well as varying contrasts introduced by preparation pulses) —are conceptualized as different *tasks*. Each 'task' is assigned to a time dimension, and all those dimensions can be resolved using a low-rank tensor (LRT) to exploit the image correlation along each dimension. Rather than 'freezing' some unwanted image dynamics, MR Multitasking 'embraces' all dynamics with a continuous acquisition without ECG triggering/gating, breath-holding or respiratory navigation. In the past few years, MR Multitasking has not only been explored in cardiovascular imaging [4, 5, 6], but also been extended to many other applications, such as whole-brain multi-parametric mapping [7, 8] and free-breathing quantitative dynamic contrast-enhanced (DCE) MRI of the abdomen [9].

The theory and core components of MR Multitasking are summarized in the following sub-sections.

2.1.1 The image model

In MR Multitasking, the image to be reconstructed is represented in a multidimensional function $a(\mathbf{x}, t_1, t_2, \dots, t_N)$, where $\mathbf{x}$ indexes the spatial dimension, and $t_1, t_2, \dots t_N$ index different temporal dimensions (including but not limited to temporal evolution within one recovery period, respiratory motion, cardiac motion, etc.). Given the

high spatiotemporal correlation among different dimensions, the multidimensional image can be discretized and viewed as a low-rank tensor $\mathcal{A}$, which is partially separable, i.e.

$$\mathcal{A} = \mathcal{G} \times_1 \mathbf{U}_\mathbf{x} \times_2 \mathbf{U}_{t_1} \times_3 \mathbf{U}_{t_2} \times_4 \cdots \times_{N+1} \mathbf{U}_{t_N} \tag{2.1}$$

where $\times_i$ denotes the tensor i-mode product; $\mathbf{U}_\mathbf{x} \in \mathbb{C}^{J \times L_0}$ contains L_0 spatial basis functions with J voxels each, $\mathbf{U}_{t_1} \in \mathbb{C}^{K \times L_1}$ contains L_1 basis functions characterizing the first temporal dimension, $\mathbf{U}_{t_2} \in \mathbb{C}^{M \times L_2}$ contains L_2 temporal basis functions characterizing the second temporal dimension, and so on; $\mathcal{G} \in \mathbb{C}^{L_0 \times L_1 \times L_2 \times \cdots \times L_N}$ denotes the core tensor that governs the interaction between different dimensions.

The core tensor and temporal bases can be combined into a temporal factor tensor $\Phi = \mathcal{G} \times_2 \mathbf{U}_{t_1} \times_3 \mathbf{U}_{t_2} \times_{t_3} \cdots \times_{N+1} \mathbf{U}_{t_N}$, in which case Equation (2.1) simplifies to

$$\mathcal{A} = \Phi \times_1 \mathbf{U}_\mathbf{x} \tag{2.2}$$

Equations (2.1) and (2.2) can also be expressed in factorized form as follows:

$$a(\mathbf{x}, t_1, t_2, \ldots, t_N) = \sum_{j=1}^{J} u_j(\mathbf{x}) \phi_j(t_1, t_2, \cdots, t_N) \tag{2.3}$$

$$\phi_j(t_1, t_2, \cdots, t_N) = \sum_{l_1=1}^{L_1} \sum_{l_2=1}^{L_2} \cdots \sum_{l_n=1}^{L_N} g_{JL_1L_2\cdots L_N} \cdot v_1(t_1) \cdot v_2(t_2) \cdots v_N(t_N) \tag{2.4}$$

where $\{u_j(\mathbf{x})\}_{j=1}^{J}$ represent spatial basis functions spanning the spatial subspace, $\{v_i(t_i)\}_{l_i=1}^{L_i}$ are temporal basis functions spanning the N individual temporal subspaces, and $g_{JL_1L_2\cdots L_N}$ are the elements of the core tensor $\mathcal{G}$.

2.1.2 K-space sampling and image reconstruction

Based on Equation (2.2), in which the temporal and spatial information of $\mathcal{A}$ are separated as Φ and $\mathbf{U_x}$, we can reconstruct the multidimensional image by serially solving Φ and $\mathbf{U_x}$, rather than solving the low-rank tensor $\mathcal{A}$ as a whole.

To solve the temporal factor Φ, we need to collect k-space data with enough sampling rate to ensure enough temporal resolution, but we only need very limited spatial information. Therefore, the central k-space line or a very limited number of central k-space lines are frequently and periodically collected, to capture the temporal dynamics with the strongest signal intensity. The frequently sampled subset of k-space as described above, is referred to as "training data" (denoted as $\mathbf{d}_{\mathrm{tr}}$) in the framework of MR Multitasking. Basically, Φ can be reconstructed from $\mathbf{d}_{\mathrm{tr}}$ using singular value decomposition (SVD) thresholding or higher-order SVD truncation. See Section 2.1.3 for more details.

To solve the spatial factor $\mathbf{U_x}$, the whole k-space needs to be sampled to achieve desired spatial resolution and field of view. It is worth noting that the k-space sampling pattern should be designed in a way that incoherence is ensured between the sampling operator and the temporal factor matrices [3]. Thus, the sampling strategy needs to be unsynchronized with any physiological dynamics, such as respiratory or cardiac cycles if involved, or magnetization preparation periods. In this work, randomized Cartesian sampling or radial sampling with golden-angle stack-of-stars spoke reordering are employed for this purpose. To distinguish from the "training data" $\mathbf{d}_{\mathrm{tr}}$, the subset of k-space data acquired to recover $\mathbf{U_x}$ is referred to as "imaging data" (denoted as $\mathbf{d}_{\mathrm{im}}$).

Given Φ reconstructed from $\mathbf{d}_{\mathrm{tr}}$, the spatial factor $\mathbf{U_x}$ can be solved from $\mathbf{d}_{\mathrm{im}}$ by:

$$\widehat{\mathbf{U}}_{\mathbf{x}} = \arg\min_{\mathbf{U_x}} \|\mathbf{d}_{\mathrm{im}} - \Omega(\Phi \times_1 \mathbf{FSU_x})\|_2^2 + \lambda R(\mathbf{U_x}) \tag{2.5}$$

where $\mathbf{F}$ is the Fourier encoding operator, $\mathbf{S}$ is the sensitivity map information for multi-coil acquisition, Ω is the undersampling operator, and $R(\cdot)$ is a regularization functional that additionally exploits compressed sensing.

Figure 2.1 illustrates one example of a possible k-space sampling pattern using radial sampling with golden-angle stack-of-stars spoke reordering.

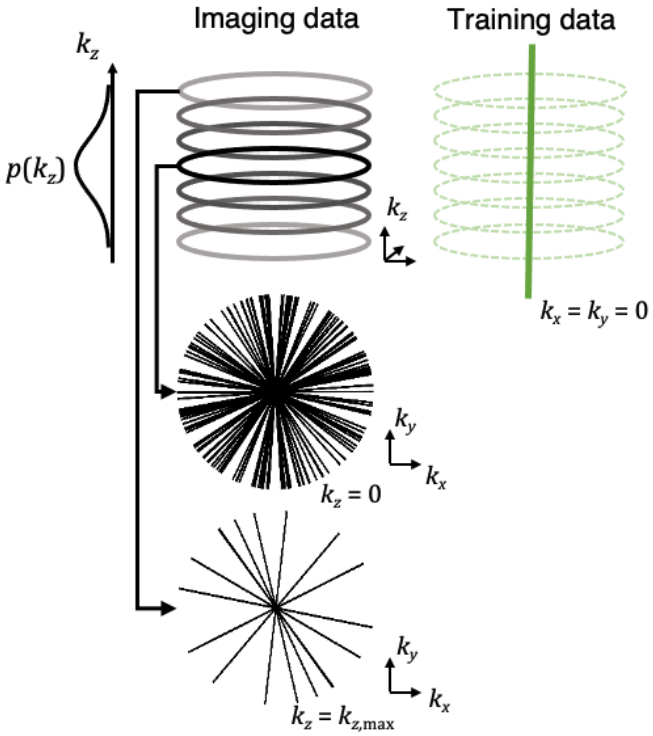

Figure 2.1: A possible k-space sampling pattern for MR Multitasking. The k-space is continuously sampled with fast low-angle shot (FLASH) readouts using a stack-of-stars acquisition with golden angle ordering in-plane and Gaussian-density randomized ordering in the partition direction. In this example, "training data" (central k-space lines) are acquired along the partition direction ($k_x = k_y = 0$) to better capture respiratory motion.

2.1.3 Tensor subspace estimation

As in the previous sub-section, the "training data" $\mathbf{d}_{\mathrm{tr}}$ is acquired continuously and periodically throughout the scan. In order to recover the temporal factor Φ, a tensor $\mathcal{D}_{\mathrm{tr}}$ can firstly be filled from $\mathbf{d}_{\mathrm{tr}}$, i.e., $\mathcal{D}_{\mathrm{tr}}$ is indexed as $(\mathbf{k}, t_1, t_2, \cdots, t_N)$, where $\mathbf{k}$ indicates the

k-space location, and t_i is the index along each temporal dimension, such as the recovery period, respiratory motion or cardiac motion, etc.

For each data point of $\mathbf{d}_{\mathrm{tr}}$, multiple temporal indices may need to be determined. The temporal index within any recovery period (e.g., acquisition between two inversion recovery or any other two magnetization preparation pulses) can naturally be determined according to the chronological order. The temporal index corresponding to motion states can be determined directly from $\mathbf{d}_{\mathrm{tr}}$ using motion identification ("binning") algorithms [3], or from external physiological detection data [10, 11].

However, it is possible that not all combinations of the temporal indices are covered in the training data $\mathbf{d}_{\mathrm{tr}}$, given the limited scan time. Therefore, those data entries from the "missing" index combinations need to be recovered to make the tensor $\mathcal{D}_{\mathrm{tr}}$ complete. This can be achieved with the following LRT completion problem:

$$\widehat{\mathcal{D}}_{\mathrm{tr}} = \arg\min_{\mathcal{D}_{\mathrm{tr}}} \|\mathbf{d}_{\mathrm{tr}} - \Omega_{\mathrm{tr}}(\mathcal{D}_{\mathrm{tr}})\|_2^2 + \lambda \sum_{i=1}^{N+1} \left\|\mathbf{D}_{\mathrm{tr},(i)}\right\|_* + \mu R(\mathcal{D}_{\mathrm{tr}}) \tag{2.6}$$

where $\|\cdot\|_*$ denotes the nuclear norm, $R(\cdot)$ is a regularization functional that exploits other properties of $\mathcal{D}_{\mathrm{tr}}$, λ and μ are weighting parameters, and Ω_{tr} indicates that only the $\mathcal{D}_{\mathrm{tr}}$ with sampled index combinations are considered in the data fidelity term.

Once $\mathcal{D}_{\mathrm{tr}}$ is completed, the temporal factor matrix Φ (or the core tensor $\mathcal{G}$ along with temporal subspace bases along different dimensions $\mathbf{U}_{t_1}, \mathbf{U}_{t_2}, \cdots, \mathbf{U}_{t_N}$) can be recovered with higher-order SVD (HOSVD) of $\widehat{\mathcal{D}}_{\mathrm{tr}}$ [12].

2.2 T1 mapping and Extracellular Volume (ECV) fraction

2.2.1 Late Gadolinium Enhancement

Late Gadolinium Enhancement (LGE) has been the reference standard for characterization of myocardial scar and focal fibrosis in cardiac MRI [13, 14, 15]. It is based on the shortening of T1 in fibrotic areas due to accumulation of extracellular gadolinium contrast agent, which enhances the MR signal of those regions in T1-weighted images.

However, two needs are still unmet with LGE imaging: (1) Diffuse fibrosis is hard to detect with LGE because of the absence of normal references. (2) LGE images are not quantitative, which makes it difficult to compare the results among different subjects or to perform longitudinal therapy monitoring.

2.2.2 Native T1 mapping

T1 mapping is a class of techniques to perform pixelwise measurement of the longitudinal relaxation time (T1). In 1970, a fast T1 measurement technique was proposed by Look and Locker [16], in which the relaxation curve is sampled multiple times (TIs) after an initial inversion recovery (IR) magnetization preparation pulse. Generally, T1 can be fitted with a three-parameter recovery model, i.e.

$$M_z[n] = A\left(1 - (1 - B)e^{-\frac{\mathrm{TI}[n]}{T_1}}\right) \tag{2.7}$$

where $M_z[n]$ is the signal acquired at the *n*-th inversion time $\mathrm{TI}[n]$, B indicates the inversion efficiency, and A is the amplitude factor.

Based on the Look-Locker technique, several cardiac T1 mapping methods were developed, such as MOLLI [17] and ShMOLLI [18]. In those methods, ECG-triggering were introduced, allowing images of difference TIs to be acquired at the same cardiac phase. In this way, a pixelwise T1 map can be generated for a certain cardiac phase.

2.2.3 Contrast-enhanced T1 mapping and Extracellular Volume (ECV) fraction

Similar to native T1 mapping, contrast-enhanced (or post-contrast) T1 mapping can be done after the gadolinium contrast agent is injected and distributed throughout the extracellular space [19, 20]. However, contrast-enhanced T1 values are impacted by not only physiological conditions, but also several experimental factors such as contrast doses, duration between contrast injection and post-contrast image acquisition, etc.

Combining native T1 and post-contrast T1, the extracellular volume (ECV) fraction can be estimated. Assuming the steady state is reached between myocardium and blood pool after administration of contrast agents, the following equilibrium holds [21, 22]:

$$\frac{\mathrm{ECV}_{\mathrm{myo}}}{\Delta R_{1,\mathrm{myo}}} = \frac{\mathrm{ECV}_{\mathrm{blood}}}{\Delta R_{1,\mathrm{blood}}} \tag{2.8}$$

where $\mathrm{ECV}_{\mathrm{myo}}$ and $\mathrm{ECV}_{\mathrm{blood}}$ represent ECV of the myocardial tissue and ECV of the blood pool respectively, and $\Delta R_{1,(\cdot)} = \left(T_{1,(\cdot)\mathrm{post-Gd}}\right)^{-1} - \left(T_{1,(\cdot)\mathrm{native}}\right)^{-1}$.

Given $\mathrm{ECV}_{\mathrm{blood}} = 1 - \mathrm{HCT}$, the myocardial ECV can be calculated as follows:

$$\mathrm{ECV} = (1 - \mathrm{HCT}) \cdot \frac{\frac{1}{T_{1,\mathrm{myo\ post-Gd}}} - \frac{1}{T_{1,\mathrm{myo\ native}}}}{\frac{1}{T_{1,\mathrm{blood\ post-Gd}}} - \frac{1}{T_{1,\mathrm{blood\ native}}}} \times 100\% \tag{2.9}$$

Unlike contrast-enhanced T1 values, ECV is theoretically only dependent on the underlying physiology, thus is more reproducible for myocardial tissue characterization and can be measured longitudinally. Previous studies have shown that ECV can be used to characterize not only focal myocardial fibrosis [23], but diffuse myocardial fibrosis as well [24, 25, 26].

2.2.4 Technical challenges in small animal studies

In preclinical imaging studies of myocardial diseases, rodent have been the most widely used models because of the high reproducibility, short development period and low cost. However, it is technically challenging to acquire high-quality T1 and ECV maps in small animals because of high heart rates and high respiration rates.

In all previous studies with a Look-Locker scheme (see **Section 2.2.2**), ECG triggering was always needed to monitor cardiac motion [22, 27, 28, 29]. Respiratory motion was handled with navigation [28] or simple signal averaging [27, 29]. ECG and respiratory gating setup make the workflow more complicated. Also, ECG triggering at high field strengths and high heart rates is unreliable due to elevated magnetohydrodynamic effects, which can introduce trigger-related motion artifacts and blurring effects [30, 31]. Therefore, quantification of ECV with cardiac MRI is still not well established despite the important unmet needs in preclinical research.

2.3 Chemical exchange saturation transfer (CEST) imaging

Chemical exchange saturation transfer (CEST) is a metabolic imaging technique that indirectly detects exchangeable protons through water signal after they are pre-saturated with selective frequencies [32]. Since Ward et al. published the first CEST paper in 2000 [34], CEST MRI has become an emerging metabolic imaging technique with various clinical applications.

2.3.1 Principles of CEST

Principles of CEST imaging are illustrated in **Figure 2.2**. They can be explained by looking at the full name *chemical exchange saturation transfer* word by word:

Chemical exchange. A simplified two-pool model (solute pool and water pool) is illustrated in **Figure 2.2a** [32]. Protons in the solute pool and the water pool resonate at different frequencies, and they are exchanging all the time.

Saturation transfer. As in **Figure 2.2b** [33], solute protons can be saturated using frequency selective saturation pulses. Some of these saturated protons will be transferred into the water pool, causing water signal loss. The amount of the water signal loss normally indicates the solute proton concentration and the exchange rate. In this way, we can indirectly detect those exchangeable molecules in water signal.

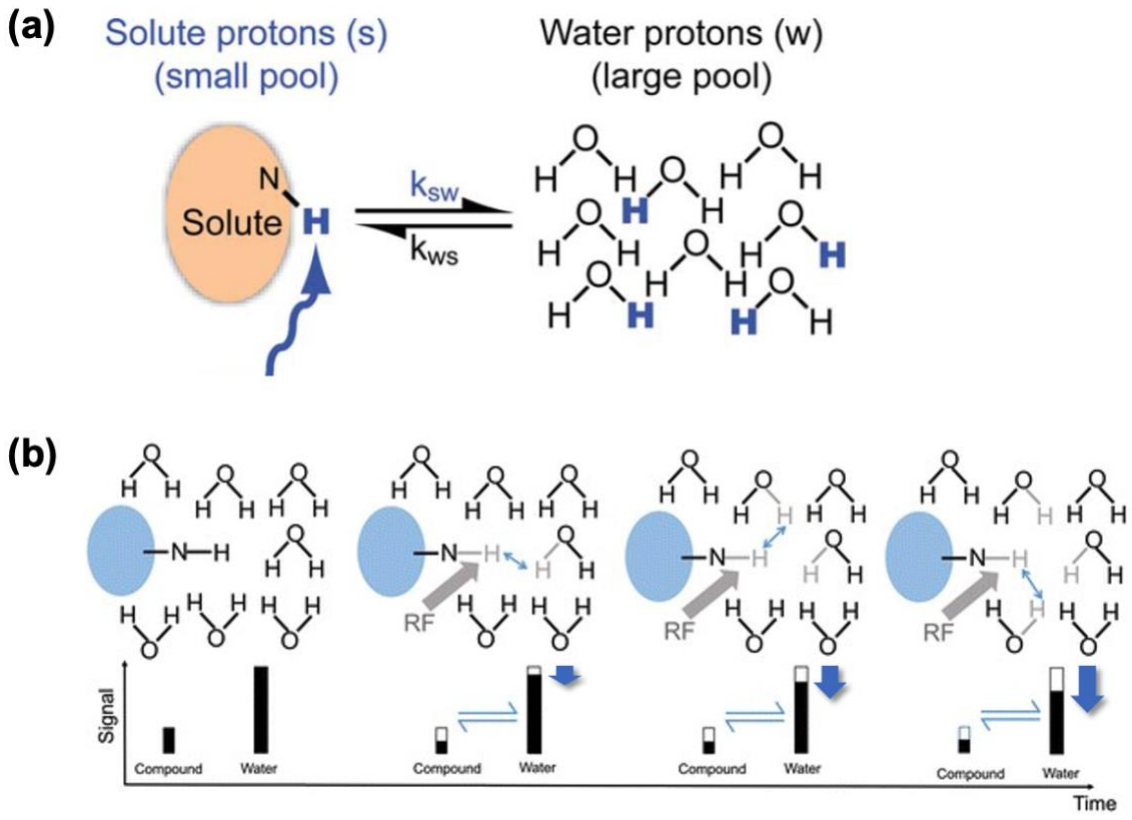

Figure 2.2: Principles of chemical exchange saturation transfer (CEST) imaging. **(a)** and **(b)** were modified from Figure 1a in [32] and Figure 1a in [33] respectively.

If we acquire water signals that are pre-saturated with different frequency offsets, then we will get the CEST spectrum (or Z-spectrum) after normalization using signals acquired without saturation pulses.

Traditionally, a CEST imaging acquisition module consist of three parts: **(1) CEST preparation.** A group of saturation pulses are applied to allow water signal loss. In clinical applications, Gaussian-shaped pulse trains rather than continuous-wave pulses are commonly used to avoid SAR issues. **(2) K-space readout.** Different readout schemes, such as FLASH, TSE, or EPI, can be used. **(3) Recovery delay.** After the readout, a waiting gap is often used for T1 recovery to increase the SNR.

Another CEST imaging acquisition scheme, the steady-state CEST (ss-CEST) method, performs pre-saturation and k-space sampling in an interleaved pattern with repeated modules [69, 70]. A basic module in ss-CEST acquisition consists only a single saturation pulse, followed by readout of several k-space lines, which repeats at a very short period.

2.3.2 Applications

Amide proton transfer (APT) imaging

Developed by Zhou et al. in 2003, the amide proton transfer (APT) MRI is one of the earliest and most commonly used CEST applications [36, 37]. It can detect amide protons of mobile proteins and peptides indirectly from water signal, where the maximum APT effect can be observed at around 3.5 ppm downfield from water.

APT imaging has been studied in various clinical applications. For instance, it has been used for tumor characterization and diagnosis of brain tumors, including tumor grading for differentiation between high-grade and low-grade gliomas [38, 39, 40, 41, 42],

and evaluation of tumor response to therapy [43, 44, 45, 46]. It can also be applied to detect ischemic stroke [47, 48, 49, 50, 51].

Detection of glycogen: glycoCEST and glycoNOE

Glycogen is the storage form of glucose in humans, which are mainly stored in the liver and skeletal muscles. It can be detected with CEST imaging (glycoCEST) from hydroxyl protons in 0.5 to 1.5 ppm downfield from water [52]. The feasibility of detecting glycogen has been demonstrated in the liver [52, 53, 54].

Recently, a new glycogen imaging method called glycoNOE was developed at ultra-high fields. In glyceNOE imaging, the nuclear Overhauser enhancement effects (NOEs) between water protons and glycogen aliphatic protons, with a peak at around 1.0 ppm upfield from water, were detected in the Z-spectrum [55]. In vitro experiments showed that the glycoNOE signal was linearly correlated with glycogen concentration.

Detection of glycosaminoglycan (GAG): gagCEST

Glycosaminoglycan (GAG) plays an important role in supporting human musculoskeletal functions [56]. It can be detected with CEST imaging (gagCEST) from labile hydroxyl protons at 1.0 ppm downfield from water. gagCEST allows detection of GAG concentration and pH change in the articular cartilage, and has already been applied to human knee joints [57, 58] and intervertebral discs [59, 60, 61, 62].

2.3.3 Technical challenges

Long scan time is still a crucial problem in many CEST imaging applications. In conventional CEST acquisitions, each image readout is followed by a pre-saturation module with long enough duration to reach the steady state of chemical exchange. In recent years, advanced Z-spectrum analysis methods such as multi-pool fitting are getting

more popular, in which distinct CEST effects can be separately measured [63, 64, 65]. To achieve this, dense sampling of the wide Z-spectrum is generally required. Therefore, the total imaging time will be prolonged significantly, making fast, high-quality 3D CEST imaging very challenging.

The snapshot-CEST method is recently developed for fast 3D CEST imaging [66]. The scan time is shortened in snapshot-CEST mainly by optimizing the k-space sampling efficiency [67, 68]. The steady-state CEST method is another potential solution to accelerate volumetric CEST imaging [69, 70]. Several fast 3D brain steady-state CEST protocols were developed in recent years [71, 72, 73, 74].

Another technical challenge of CEST imaging is motion handling. All fast CEST imaging techniques mentioned above were developed for brain imaging. They cannot be directly applied to moving organs such as liver, pancreas, or even heart. In human studies, breath-holding is often needed to reduce respiratory motion. However, even with multiple breath holds, 3D CEST imaging is almost impossible to apply in moving organs, because the total scan time would become intolerable in clinical practice. This problem could severely limit the clinical application of CEST imaging in moving organs.

CHAPTER 3: ECG-less, Free-breathing Myocardial ECV Mapping in Small Animals at High Heart Rates

3.1 Background

Cardiac magnetic resonance (CMR) T1 mapping is a powerful diagnostic modality for various abnormalities of the myocardium, such as edema, amyloidosis, and overload of lipid or iron [1, 76, 13]. Combined with gadolinium contrast enhancement, T1 mapping allows extracellular volume fraction (ECV) quantification, which can be used to characterize focal or diffuse myocardial fibrosis [13, 24, 25, 26].

Rodent models are widely used in preclinical studies of myocardial diseases because of the short development period, availability of genetically modified disease models, and low cost. However, it is technically challenging to acquire high-quality T1 and ECV maps in small animals because of high heart rates (usually faster than 300 bpm) and high respiration rates (around 60 cpm). Therefore, CMR quantification of ECV is still not well established despite the important unmet needs in research. Several studies have been done to improve CMR T1 mapping and/or ECV measurement in small animals. Coolen et al. proposed a 3D T1 mapping method of the mouse heart using variable flip angle (VFA) analysis [77]. The method can detect regional differences in myocardium with excellent repeatability, but VFA-based methods have inherent problems with B_1 inhomogeneity, and the long scan time (more than 20 mins) makes it impractical to be used in pre- and post-Gd studies. Messroghli et al. acquired myocardial T1 and ECV maps in rats from a single (unsegmented) dataset using a small animal Look-Locker inversion recovery (SALLI) method [22, 27]. It was able to reconstruct both cine MR

images and T1 maps, and showed the feasibility to detect diffuse myocardial fibrosis, while the spatial resolution was limited due to SNR consideration. Segmented multi-shot FLASH methods were then proposed to acquired images with higher resolution [28, 29].

In all previous studies with a Look-Locker scheme [16, 17], ECG triggering was used to monitor cardiac motion [22, 27, 28, 29]. However, ECG triggering at high field strengths is unreliable due to elevated magnetohydrodynamic (MHD) effects, which can introduce trigger-related motion artifacts and blurring effects [30, 31]. High heart rates may make the situation even worse. Respiratory navigation was used in some studies [28], however, most studies simply used signal averaging, resulting in image blurring [27, 29]. Furthermore, ECG and respiratory gating setup leads to complicated workflow.

In this study, we developed an ECG-less, free-breathing ECV mapping method using MR Multitasking [3] (hereinafter abbreviated as ***ECV Multitasking***) on a 9.4 T small animal MRI system. It allows continuous acquisition without ECG triggering or respiratory gating. The pre- and post-Gd data were acquired separately but reconstructed jointly, to allow image co-registration and direct ECV mapping. The feasibility of characterizing diffuse myocardial fibrosis was tested in a rat hypertensive heart failure model with preserved ejection fraction (HFpEF), which has been shown to have increased interstitial fibrosis in left ventricular [78, 79, 80], and has been recapitulated in recent studies [81, 82, 83].

3.2 Methods

3.2.1 Animal model

All animal experiments were approved by the Cedars-Sinai Institutional Animal Care and Use Committee. Dahl salt-sensitive (DSS) rats can develop hypertension

followed by HFpEF on a high-salt diet [78, 79]. In this model, male DSS rats (Charles River Laboratories, MA) were normally fed (0.3% NaCl) until the age of 7 weeks. Rats were then randomly assigned to a high-salt (HS) diet group (8% NaCl) to induce HFpEF or a normal-salt (NS) diet group (0.3% NaCl) to serve as controls, until the age of 14 weeks [84]. HS rats with heart failure symptoms (including decreased activity, cachexia, labored breathing, and body edema) and detectable diastolic dysfunction by echocardiography were diagnosed as HFpEF.

Nine control rats (control group: n = 9; weight, 335 ± 44 g) and nine HS fed rats diagnosed with HFpEF (HFpEF group: n = 9; weight, 286 ± 47 g) were imaged. Imaging experiments and all measurements were done between the age of 14 weeks and 15 weeks. After the imaging study, animals were euthanized, and the hearts were excised. Mid-ventricular heart tissues of the nine control rats (n = 9) and nine HFpEF rats (n = 9) were sectioned and stained with Masson's trichrome staining.

3.2.2 MRI protocol

All MRI data were acquired on a 9.4 T preclinical system (BioSpec 94/20 USR; Bruker Biospin, Billerica, MA) using a single-channel volume coil. The T1 Multitasking sequence was implemented in Paravision 5.1 by modifying the built-in FLASH sequence.

The rat was anesthetized before the scan, and the tail vein was cannulated for later Gd injection within the scan. During the scan, anesthesia was maintained by ventilation with 1.5% isoflurane-oxygen. After the scan, hematocrit (HCT) level was measured for ECV calculation.

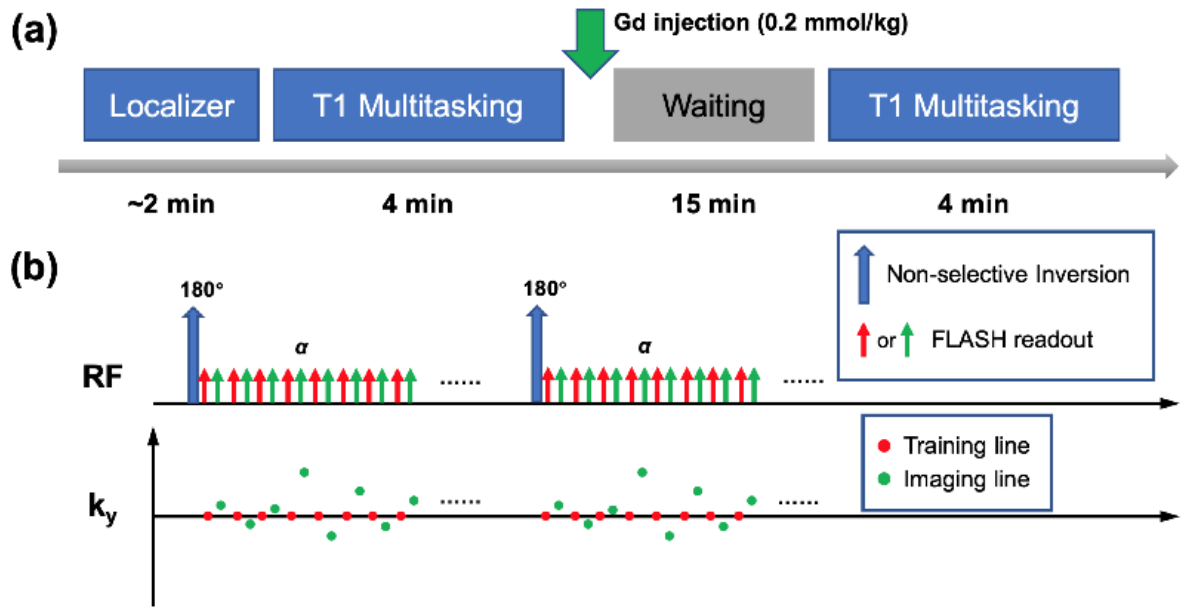

Figure 3.1: Imaging workflow and T1 Multitasking sequence diagram.

Figure 3.1a shows the imaging workflow for one rat study. A self-gated (IntraGate) localizer was used to select a slice with a mid-cavity short-axis view of left ventricle (LV). The T1 Multitasking sequence [4] (**Figure 3.1b**) was then performed. Gd contrast agent (Gadavist, 0.2 mmol/kg; Bayer Schering Pharma, Berlin-Wedding, Germany) was manually injected immediately afterwards. Fifteen minutes later, the T1 Multitasking sequence was repeated on the same slice using identical imaging parameters. The total exam time was around 25 minutes.

T1 Multitasking was performed using a continuous FLASH acquisition with repeated non-selective inversion recovery (IR) magnetization preparation pulses. Odd-numbered readouts followed randomized Gaussian-density sampling in the phase encoding (k_y) direction (used as the imaging data), and even-numbered readouts collected the k-space center line ($k_y = 0$, used as the subspace training data). Imaging

parameters were: matrix size = 128 x 128, FOV = 40 x 40 mm^2, voxel size = 0.31 x 0.31 x 1.5 mm^3, flip angle = 5°, TR/TE = 7.0/2.4 ms, recovery period (time between adjacent IR pulses) = 2.9 s. In each T1 Multitasking module, 85 IR preparation pulses were applied, resulting in a total scan time of 4 min 10 s.

Data acquired from pre- and post-Gd T1 Multitasking sequence was reconstructed and analyzed jointly, as described in the following sections. The joint pre- and post-Gd reconstruction can improve respiratory and cardiac binning and promote image co-registration in native and post-Gd T1 fitting.

3.2.3 Image reconstruction

Images from the proposed ECV Multitasking protocol are represented as a high-dimensional image $A(\mathbf{x}, t_c, t_r, t_{T_1})$ with 2 spatial dimensions and 3 temporal dimensions (cardiac phase t_c, respiratory phase t_r, and T1 recovery time t_{T_1}). The high-dimensional image can be discretized and viewed as a low-rank tensor $\mathcal{A}$, and thus partially separable [85], i.e.

$$\mathbf{A}_{(1)} = \mathbf{U}_\mathbf{x}\mathbf{C}_{(1)}\left(\mathbf{U}_c \otimes \mathbf{U}_r \otimes \mathbf{U}_{T_1}\right)^T \tag{3.1}$$

where columns of $\mathbf{U}_\mathbf{x}$ represents spatial basis functions; columns of $\mathbf{U}_c$, $\mathbf{U}_r$, and $\mathbf{U}_{T_1}$ contain cardiac, respiratory, and T1 recovery temporal basis functions, respectively; $\otimes$ denotes the Kronecker product; and $\mathbf{A}_{(1)}$ and $\mathbf{C}_{(1)}$ are mode-1 matricization of the image tensor $\mathcal{A}$ and the core tensor $\mathcal{C}$ respectively [86].

Equation (3.1) permits $\mathbf{A}_{(1)} = \mathbf{U}_\mathbf{x}\mathbf{\Phi}$, where $\mathbf{\Phi} = \mathbf{C}_{(1)}\left(\mathbf{U}_c \otimes \mathbf{U}_r \otimes \mathbf{U}_{T_1}\right)^T$, in which $\mathbf{\Phi}$ and $\mathbf{U}_\mathbf{x}$ contain separate temporal and spatial bases respectively. Therefore, $\mathbf{\Phi}$ can be first recovered using only the training data $\mathbf{d}_{tr}$, which is frequently sampled in time, via

Bloch-constrained low-rank tensor completion followed by high-order singular value decomposition (HOSVD) [3, 12]. With $\mathbf{\Phi}$ determined, the spatial basis $\mathbf{U_x}$ can then be reconstructed from the imaging data $\mathbf{d}_{\mathrm{im}}$ by solving the following problem:

$$\widehat{\mathbf{U}}_{\mathbf{x}} = \mathrm{argmin}_{\mathbf{U}} \|\mathbf{d}_{\mathrm{im}} - \Omega(\mathbf{E}\mathbf{U}_{\mathbf{x}}\mathbf{\Phi})\|_2^2 + \lambda R(\mathbf{U}_{\mathbf{x}}) \tag{3.2}$$

where $\mathbf{E}$ is the signal encoding operator, including Fourier transformation and coil sensitivities weighting (optional), Ω is the undersampling operator, and R is a regularization functional which was chosen here as a wavelet sparsity penalty in order to additionally exploit compressed sensing [87].

A detailed description of the basic image model and reconstruction scheme used in MR Multitasking can be found in previous work [3, 4]. In this work, it is divided into the following steps:

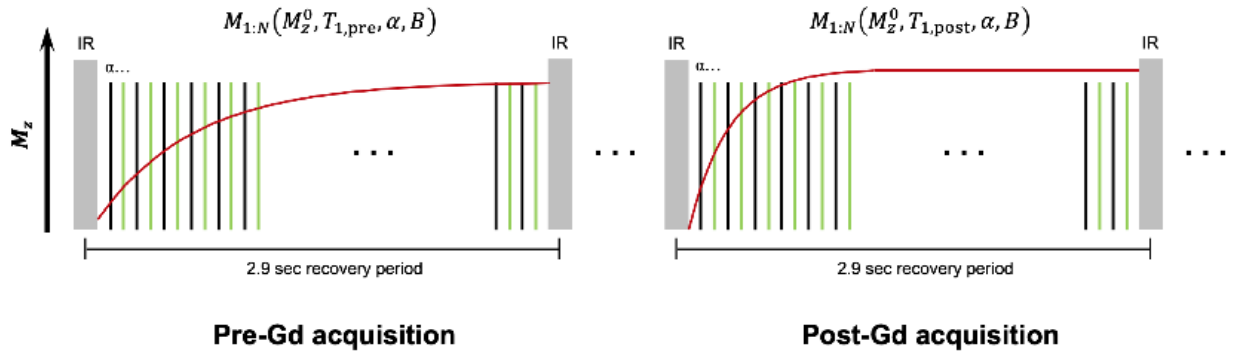

Figure 3.2: Illustration of joint pre- and post-Gd T1 recovery modeling. A pair of single blocks from pre- and post-Gd acquisition are Bloch simulated together, with the same FLASH flip angle α and inversion efficiency B.

1) Determination of T1 recovery basis functions in $\mathbf{U}_{\mathrm{T}_1}$ with Bloch simulation

The IR-prepared T1 recovery process is modeled by Bloch simulations to determine $\mathbf{U}_{\mathrm{T}_1}$. In this work, pairs of pre- and post-Gd T1 recovery curves were jointly simulated as shown in **Figure 3.2**, for the purposes of joint physical modeling during

respiratory and cardiac binning (Step 3) and multidimensional image reconstruction (Step 4). The detailed information of the T1 recovery modeling is available in Section 3.2.4 .

A dictionary was generated with this model using 101 T1 values ranging from 100 ms to 3000 ms ($T_{1,\mathrm{pre}} > T_{1,\mathrm{post}}$ combinations only), 15 FLASH flip angles from 0.5° to 7.5°, and 21 inversion efficiency values from -1 (complete inversion) to 0 (no inversion). The SVD of this dictionary yielded the T1 recovery basis functions $\mathbf{U}_{\mathrm{T}_1}$.

2) Real-time image reconstruction

A “real-time” (i.e., ungated before sorting into multiple time dimensions) image was first generated for motion identification:

$$\mathbf{X}_{\mathrm{rt}} = \mathbf{U}_{\mathbf{x},\mathrm{rt}}\boldsymbol{\Phi}_{\mathrm{rt}} \tag{3.3}$$

where rows of $\boldsymbol{\Phi}_{\mathrm{rt}}$ correspond to the real-time temporal basis functions, and columns of $\mathbf{U}_{\mathbf{x},\mathrm{rt}}$ correspond to the spatial basis functions.

The real-time temporal basis $\boldsymbol{\Phi}_{\mathrm{rt}}$ was estimated from the SVD of the training data $\mathbf{d}_{\mathrm{tr}}$. Then the spatial coefficients $\mathbf{U}_{\mathbf{x},\mathrm{rt}}$ were recovered by solving the least-squares optimization problem:

$$\widehat{\mathbf{U}}_{\mathbf{x},\mathrm{rt}} = \mathrm{argmin}_{\mathbf{U}_{\mathrm{rt}}} \left\| \mathbf{d}_{\mathrm{im}} - \Omega\left(\mathbf{E}\mathbf{U}_{\mathbf{x},\mathrm{rt}}\boldsymbol{\Phi}_{\mathrm{rt}}\right) \right\|_2^2 \tag{3.4}$$

3) Respiratory and cardiac binning

Different time points of $\mathbf{X}_{\mathrm{rt}}$ were assigned to multiple respiratory motion states (“respiratory bins”) and cardiac motion states (“cardiac bins”) based on the real-time images generated in Step 2. A modified k-means clustering method was used to automatically group the data into different bins, incorporating the predetermined low-rank T1 recovery model in $\mathbf{U}_{\mathrm{T}_1}$ to address the contrast change of $\mathbf{X}_{\mathrm{rt}}$ from T1 recovery [3].

4) Tensor formation and multidimensional reconstruction

After cardiac and respiratory binning, each readout time point was assigned three temporal indices: cardiac phase, respiratory phase, and T1 recovery index. A 4-way training data tensor $\mathcal{D}_{\mathrm{tr}}$ with one k-space readout dimension and three temporal dimensions was recovered from the subspace training data $\mathbf{d}_{\mathrm{tr}}$ by solving a Bloch-constrained low-rank tensor completion problem.

After $\mathcal{D}_{\mathrm{tr}}$ is completed, the cardiac basis functions $\mathbf{U}_{\mathrm{c}}$, the respiratory basis functions $\mathbf{U}_{\mathrm{r}}$, and the core tensor $\mathcal{C}$ can be extracted from the HOSVD of $\mathbf{D}_{\mathrm{tr}}$, fully determining $\mathbf{\Phi} = \mathbf{C}_{(1)}\left(\mathbf{U}_{\mathrm{c}} \otimes \mathbf{U}_{\mathrm{r}} \otimes \mathbf{U}_{\mathrm{T}_1}\right)^{\mathrm{T}}$. The spatial coefficients $\mathbf{U}_{\mathbf{x}}$ can then be reconstructed by solving the problem in Equation (3.2).

3.2.4 Parameter fitting and image analysis

One specific respiratory phase and cardiac phase were selected for T1 and ECV map generation, corresponding to end-expiration and end-diastole respectively. A joint pre- and post-Gd T1 recovery model was also used in pixel-wise T1 fitting. By fitting this joint model, we can get the pre- and post-Gd T1 maps simultaneously.

a) Myocardial T1 maps

The z-magnetization within a single recovery period between two adjacent IR pulses can be described as

$$M_n = M_{\mathrm{ss}} + (BM_{N+1} - M_{\mathrm{ss}}) \cdot E^{n-1} \tag{3.5}$$

$$E = e^{-\frac{TR}{T_1}} \cos\alpha \tag{3.6}$$

$$M_{N+1} = M_{ss} \frac{1 - E^N}{1 - BE^N} \tag{3.7}$$

where n is the readout index within each recovery period, $n = 1, 2, \cdots, N$; $M_{\mathrm{ss}} = \frac{1-e^{-TR/T_1}}{1-e^{-TR/T_1}\cos\alpha} M_z^0$ is the z-magnetization at true steady-state ($t \to \infty$); M_{N+1} is the actual final z-magnetization in each recovery period incorporating incomplete relaxation; and $B \in [-1,0]$ represents the inversion efficiency of the IR pulse. Our pulse sequence used $N = 416$, TR = 7 ms; α was prescribed as 5° but was not assumed to be perfectly homogenous during Bloch simulations and during fitting.

Combining Equations (3.5) – (3.7) yields the combined z-magnetization equation

$$\begin{aligned} M_n(M_z^0, T_1, \alpha, B) \\ &= M_{ss}(M_z^0, T_1, \alpha) \\ &\cdot \left[1 + \left(B \frac{1 - e^{-\frac{TR}{T_1}} \cos\alpha}{1 - Be^{-\frac{TR}{T_1}} \cos\alpha} - 1 \right) \cdot \left(e^{-\frac{TR}{T_1}} \cos\alpha \right)^{n-1} \right] \end{aligned} \tag{3.8}$$

Assuming that the B_1 field does not change between pre- and post-contrast acquisitions, the unknown actual FLASH flip angle α and inversion efficiency B can be assumed to be constant for each pixel. Therefore, the paired signal model concatenating the pre- and post-Gd signal evolution is:

$$\begin{aligned} S\left(M_z^0, T_{1,\mathrm{pre}}, T_{1,\mathrm{post}}, \alpha, B\right) \\ &= \left\{ M_{1:N}\left(M_z^0, T_{1,\mathrm{pre}}, \alpha, B\right), M_{1:N}\left(M_z^0, T_{1,\mathrm{post}}, \alpha, B\right) \right\} \cdot \sin\alpha \end{aligned} \tag{3.9}$$

Parameter fitting was done using the joint pre- and post-Gd T1 recovery model in Equation (3.9). $T_{1,\mathrm{pre}}, T_{1,\mathrm{post}}, \alpha, B$, and M_z^0 were fitted using the 832 inversion time images at the selected reparatory and cardiac phase. The pre- and post-Gd myocardial T1 maps were directly generated from the $T_{1,\mathrm{pre}}$ and $T_{1,\mathrm{post}}$ fitting results.

b) Blood T1 fitting

First, the pixels to be used for blood T1 fitting were automatically selected based on the thresholding of the fitted M_z^0 map. Then, the average T1 recovery curve from these pixels was calculated, weighted by the M_z^0 map. Finally, parameters were fitted to the average blood T1 recovery curves using the model in Equation (3.9) without Look–Locker correction (i.e., with $M_n(M_z^0, T_1, \alpha = 0, B)$) to better model the inflow of unexcited blood spins into the imaging slice [4]. The fitted $T_{1,\mathrm{pre}}$ and $T_{1,\mathrm{post}}$ values were then used as the pre- and post-Gd blood T1 values.

c) ECV calculation

The ECV map was generated according to the following equations:

$$\mathrm{ECV} = (1 - \mathrm{HCT}) \cdot \frac{\Delta R_{1,\mathrm{myo}}}{\Delta R_{1,\mathrm{blo}}} \times 100\% \tag{3.10}$$

$$\Delta R_1 = R_{1,\mathrm{post}} - R_{1,\mathrm{pre}} = \frac{1}{T_{1,\mathrm{post}}} - \frac{1}{T_{1,\mathrm{pre}}} \tag{3.11}$$

in which $\Delta R_{1,\mathrm{myo}}$ is the pixel-wise R_1 changes, and $\Delta R_{1,\mathrm{blo}}$ is the change of blood R_1, and HCT is the hematocrit value. All statistical analyses were performed for septal ECV, i.e., where $\Delta R_{1,\mathrm{myo}}$ was calculated as the mean value within the septal myocardium. All image reconstruction and curve fitting were done in MATLAB 2018a (MathWorks, Natick, MA).

3.2.5 Phantom validation

The accuracy of T1 fitting of the pre- or post-Gd T1 Multitasking sequence was tested in an 8-vial water phantom with $GdCl_3$ concentrations of 0, 10, 20, 33, 50, 80, 120 and 200 umol/kg. T1 maps generated by the Bruker built-in RARE-VTR method was used as the reference. The imaging parameters of RARE-VTR were: TE = 19.5 ms, TR array = 8000, 4000, 1500, 800, 400, 200 and 120 ms, RARE factor = 4, matrix size = 128 x 128, FOV = 40 x 40 mm^2, and total scan time = 6 min 1 s.

3.2.6 Histological analysis

Masson's trichrome staining was used to measure the extent of fibrosis. Mid-ventricular heart tissues were sectioned and stained following the manufacturer's protocol (Sigma-Aldrich, St. Louis, MO, USA). Quantitative histological analysis was done with ImageJ 1.52a (National Institutes of Health; http://imagej.nih.gov/ij). In each section, the extent of myocardial fibrosis was quantified by the percentage of total fibrosis area, which was calculated as the number of blue-stained pixels divided by the total number of pixels in the ventricular area (excluded: intramural vascular structures, perivascular collagen, endocardium, and LV trabeculae) [80, 88]. For each rat, the average percentage from five different sections was reported.

3.2.7 Statistical analysis

Welch's t-test was performed to compare ECV values between the control group and HFpEF group. The Pearson coefficient was measured to evaluate the correlation between ECV values and quantitative fibrosis percentages. A two-tailed value of $P < 0.05$ was considered to be statistically significant. Statistical graphs were generated using GraphPad Prism 8 (GraphPad Software, La Jolla, California, USA) and Microsoft Excel.

3.3 Results

The reference T1 of the phantoms measured by RARE-VTR ranged from 333 to 2433 ms, with a corresponding R_1 range from 0.41 to 3.00 s^{-1}. **Figure 3.3** shows the linear regression result of R_1 values measured by Multitasking and RARE-VTR, in which a strong linear relationship can be found ($R = 0.9983$, $P < 0.0001$).

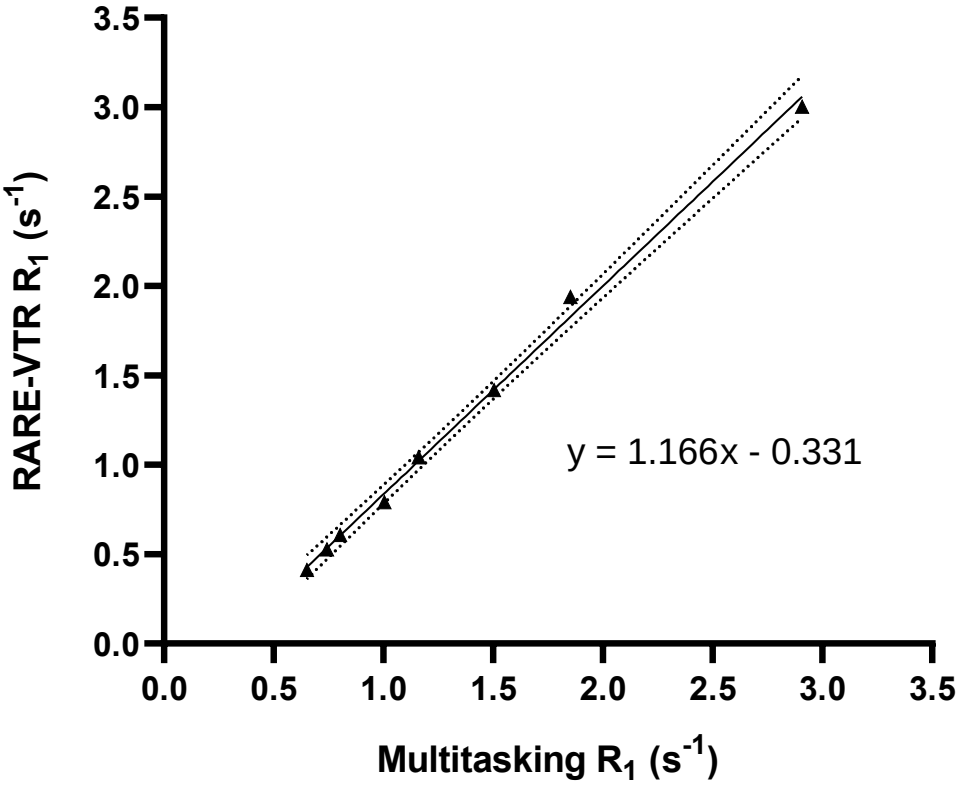

Figure 3.3: Linear regression of Multitasking and RARE-VTR R_1 values. The dotted line shows the 95% confidence bonds.

Five respiratory bins and ten cardiac bins were used for respiratory and cardiac binning, corresponding to a cardiac temporal resolution of 20 ms for a heart rate of ~300 bpm. **Figure 3.4** shows the images of the heart from a representative healthy subject right before the inversion recovery preparation pulse, generated from different cardiac and respiratory phases, i.e. $\mathcal{A}(\mathbf{x}, n_{\mathrm{c}}, n_{\mathrm{r}}, n_{\mathrm{T}_1})\big|_{n_{\mathrm{c}}=1:10,\ n_{\mathrm{r}}=1,\ n_{\mathrm{T}_1}=N=416}$ (**Figure 3.4a**) and $\mathcal{A}(\mathbf{x}, n_{\mathrm{c}}, n_{\mathrm{r}}, n_{\mathrm{T}_1})\big|_{n_{\mathrm{c}}=6,\ n_{\mathrm{r}}=1:5,\ n_{\mathrm{T}_1}=N=416}$ (**Figure 3.4b**). The diastole and the systole, or the end-expiration phase and the end-inspiration phase can be clearly differentiated in the figure.

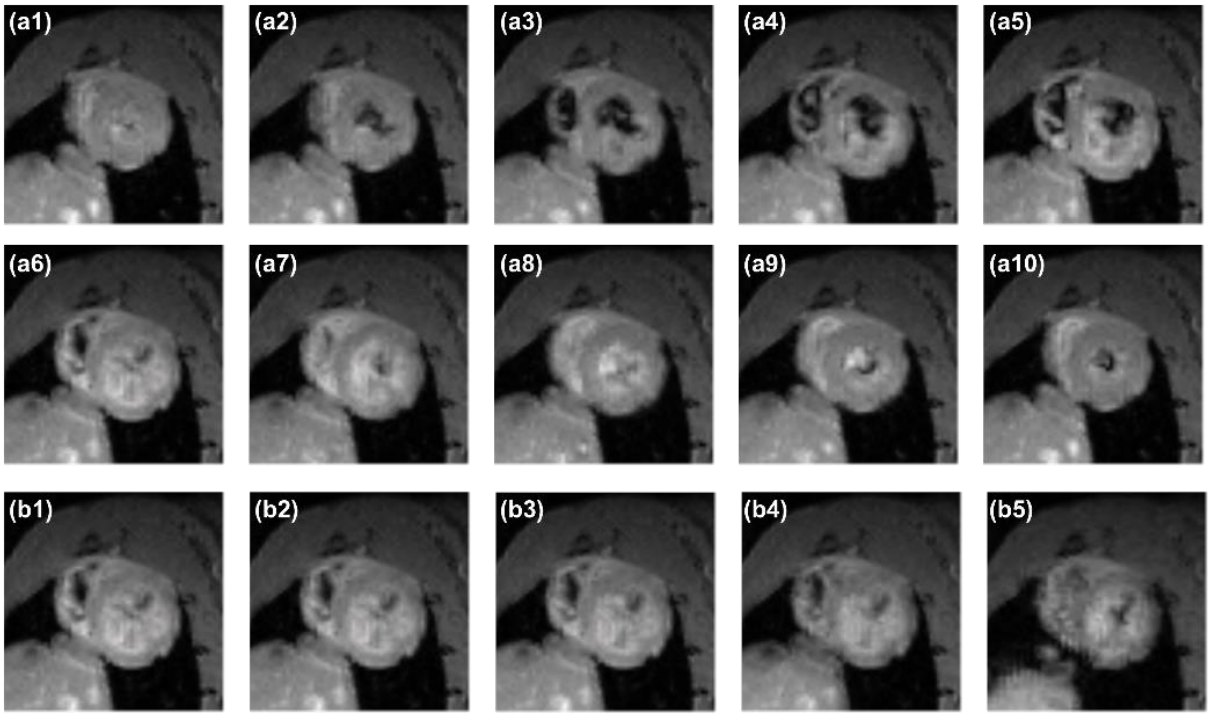

Figure 3.4: Images of different cardiac and respiratory bins.

Figure 3.5a/b shows representative native and post-Gd T1 maps from the control group and HFpEF group. T1 maps were smooth and homogeneous within the LV myocardium, except for areas in the inferior and lateral walls with imperfect fitting results (as indicated by white arrows in **Figure 3.5a**). The native myocardial T1 values (mean ± SD, in ms) were 1534 ± 151 in the control group, and 1662 ± 152 in the HFpEF group. There was no significant difference in native T1 between the control group and the HFpEF group (P = 0.09). **Figure 3.5c** shows the corresponding ECV maps. In this study, signal from the aorta rather than the LV was usually selected for blood T1 fitting, because of the signal loss resulting from LV inflow in this single slice setup; and the septal myocardium areas selected for $\Delta R_{1,\mathrm{myo}}$ calculation were indicated by red arrows. Welch's t-test

showed that ECV was significantly higher in the HFpEF group (22.4% ± 2.5%) compared with those in the control group (18.0% ± 2.1%), *P* = 0.0010, as displayed in **Figure 3.5d**.

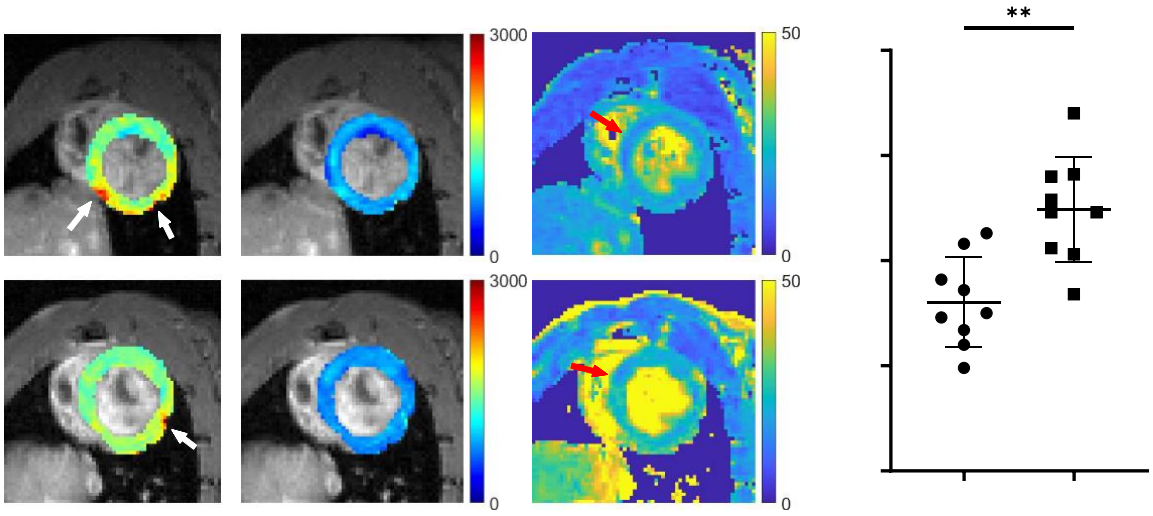

Figure 3.5: Representative T1 and ECV maps (local) from the control and HFpEF group.

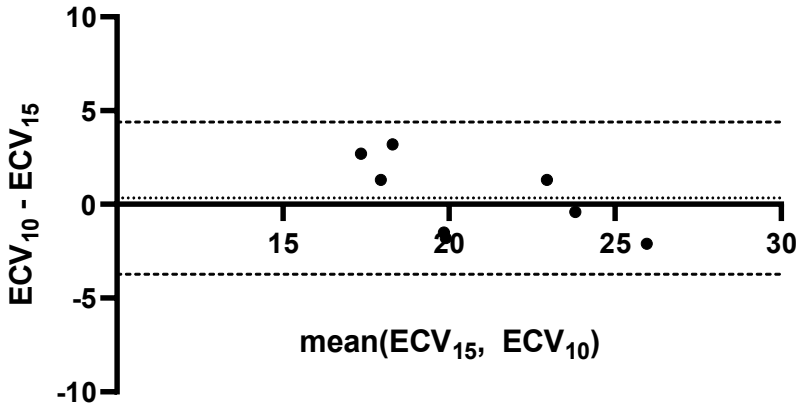

Figure 3.6: The Bland-Altman plot evaluating the repeatability of ECV measurement. The dotted and dashed lines indicate the mean bias and the 95% limit of agreement, respectively.

In eight rats (4 control + 4 HFpEF), an additional post-Gd T1 Multitasking sequence was run 10 minutes after the Gd injection, with identical imaging parameters. ECVs were

also calculated using this separate post-Gd T1 measurement. **Figure 3.6** shows the Bland-Altman plot comparing the ECVs measured from the 15-min post-Gd T1 (ECV_{15}) and the 10-min post-Gd T1 (ECV_{10}). The interclass correlation coefficient (ICC) was 0.817. The root-mean-square within-subject standard deviation was 1.4, yielding a coefficient of variation of 6.7%. There was no significant difference between ECV_{15} and ECV_{10} (P = 0.66).

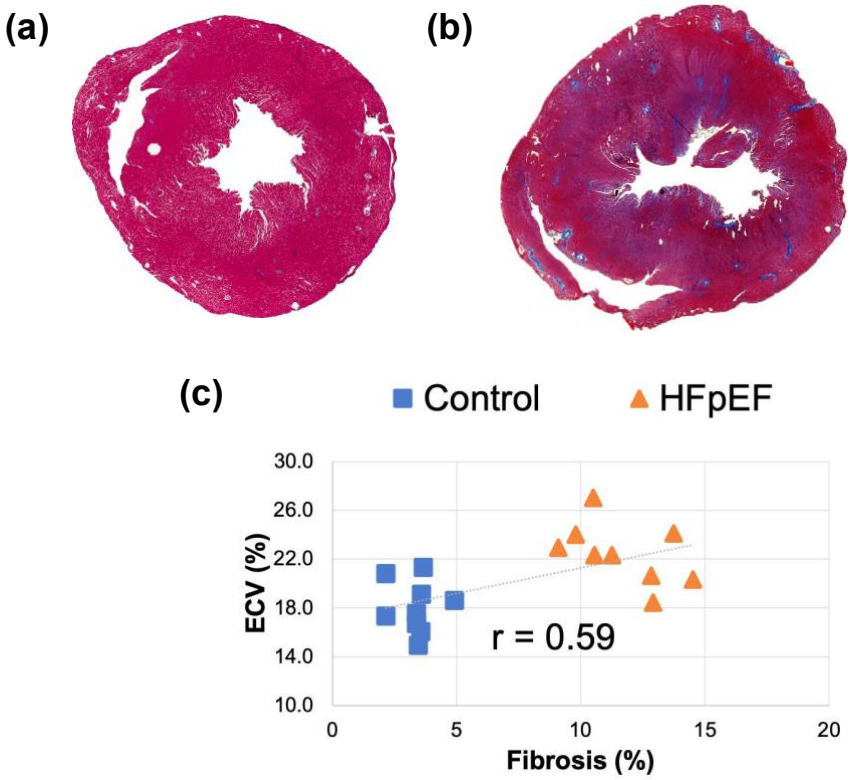

Figure 3.7: Representative histological sections and ECV(%)-fibrosis(%) scatterplot.

Figure 3.7a/b shows representative Masson trichrome-stained sections of the control and HFpEF rats. The myocardial fibrosis can be clearly seen as the diffused dark blue areas in **Figure 3.7b**. The extent of fibrosis significantly increased in HFpEF hearts (11.69% ± 1.88%) than in control hearts (3.37% ± 0.83%), $P < 0.0001$. **Figure 3.7c** shows

the relationship between the ECV value and the extent of fibrosis, in which a moderate correlation can be found (R = 0.59, P = 0.0098).

3.4 Discussion

We developed a novel ECV Multitasking protocol which can map ECV at high heart rates without ECG triggering or respiratory navigation. To test its feasibility to characterize diffuse myocardial fibrosis, a HFpEF rat model was chosen in this study. Although ECV has not previously been measured in a HFpEF rat model, there has been increasing clinical interest in T1 and ECV characterization of patients with HFpEF in recent years. Several publications showed elevated ECV in HFpEF patients versus control subjects. Su et al. reported that patients with HFpEF had elevated ECV compared with control subjects (28.9% vs. 27.9%, P = 0.006) [26]. Rommel et al. reported similar results (32.9% vs. 28.9%, P < 0.01) [25], and Mordi et al. also confirmed this finding (35.9% vs. 27.0%, P < 0.001) [24]. A modified Look-Locker inversion recovery (MOLLI) sequence was used to perform T1 mapping in all these studies. In the present study, ECV characterization was performed for the first time in a rat model with HFpEF. The elevated ECV found here in rats with HFpEF (22.4% vs. 18.0%, P = 0.0010) is consistent with previous human studies. Though so far only tested in the DSS rat model for HFpEF diagnosis [78, 79], this newly developed technique can easily be extended to other small animal applications. More importantly, the non-invasive quantitative imaging protocol not only provides a diagnostic tool, but also a method for longitudinal therapy monitoring of the same subject [89].

In the control group, native T1 values were 1534 ± 151 ms and ECV values were 18.0% ± 2.1% (both calculated from the septal area). Previous rodent studies have

reported variable myocardial T1 values, depending on field strength and T1 encoding schemes, both of which are known to affect T1 estimates. At 7.0 T, T1 values were reported as 1620 ms (Vandsburger et al.) and 1638 ms (Zhang et al.) [28, 90]. At 9.4 T, reported T1 values ranged from ~1200 ms to 1764 ms (Kim et al., Li et al., and Coolen et al.) [77, 91, 92]. ECV, a physiological quantity in principle unaffected by field strength or T1 encoding scheme, allows more direct comparison. In healthy rats, myocardial ECV was previously reported as 16% [21], 18% [93], 17.2% [22], and 15.5% [92], comparable with the 18.0% value measured in our study. A direct comparison to these previous methods on the same scanner and in the same subjects was not performed in the present study, but would be a useful future validation step.

One major technical novelty of this work compared with previous MR Multitasking work is the joint reconstruction of pre- and post-Gd data and the paired modeling of the pre- and post-Gd T1 recovery. This has two primary benefits. First, it allows the respiratory and cardiac binning to be done in the concatenated pre- and post-Gd data. In this way, the data with a similar motion state—no matter whether from pre-Gd or post-Gd—will be clustered into the same respiratory or cardiac bin, removing the need for respiratory co-registration between pre- and post-Gd T1 maps. Second, it can improve the robustness of T1 fitting by constraining pre- and post-Gd images to share the same thermal equilibrium magnetization M_z^0, FLASH flip angle α and inversion efficiency B, exploiting internal *a priori* knowledge and reducing the total number of fitting parameters from 8 to 5.

The phantom study found that the Multitasking based T1 fitting results showed a strong linear correlation with the RARE-VTR reference. If calibrated using the linear

correlation ($\tilde{R}_1 = LC(R_1) = 1.166R_1 - 0.331$), the relative R_1 difference between Multitasking method and RARE-VTR reference would be 2.7% ± 3.6%. Note that ECV measurements are insensitive to linear transformation: the ECV value is calculated by the ratio of R_1 changes of myocardial and blood pool, so both the intercept (–0.331) and slope (1.166) of the linear transformation LC will be canceled, leaving the final ECV quantification result unchanged.

Ten bins were used to separate different cardiac phases in the current protocol for ECV Multitasking reconstruction, corresponding to a cardiac temporal resolution of 20 ms for a heart rate of 300 bpm. As shown in **Figure 3.4**, the diastolic and systolic phases can be differentiated at this temporal resolution. However, for higher heart rates, such as those in mice (around 450 bpm), more cardiac bins may be required, which may have an impact on SNR and ECV homogeneity. A nearly-significant negative correlation (R = –0.44, P = 0.06) was found between the septal SNR of the ECV map and the heart rate. This may be an effect of increased intra-bin motion at higher heart rates. More cardiac bins can possibly be achieved by shortening the echo spacing, or by acquiring k-space training line and imaging lines in separate echoes after each FLASH flip angle [94].

In this work, blood T1 was extracted by fitting the weighted average T1 recovery curve of the selected blood pool. The FLASH flip angle α in Equation (3.6) was fixed as 0 to remove Look-Locker correction and better model the inflow of unexcited blood spins. This approach is particular to 2D slice-selective excitation, for which blood spins flow through the slice quickly enough that Look-Locker correction is not required. For a volumetric 3D variation of our method, the blood spins would be driven towards steady-state, and the Look-Locker correction could be retained in blood.

T1 inhomogeneity was present in the inferior and lateral walls due to potential B_1 issues at high B_0 field, as visible in **Figure 3.4**. In diffuse myocardial disease, it does not affect the ECV calculation from septal area. However, it will affect the accuracy of the ECV map in the inferior and lateral walls. This may reduce the reliability of the method in the diagnosis of focal myocardial disease, such as focal myocardial infarction. Further sequence improvements, such as a dual-flip-angle acquisition [95], should be made to address this problem.

The method described here did not include bulk motion compensation, as anesthesia and additional immobilization setup did not result in any apparent bulk motion. However, bulk motion compensation is compatible with the MR Multitasking framework, as described in [9], where a translational inter-bin registration to k-space data was applied prior to joint reconstruction. Similar motion compensation could be incorporated into the proposed method if used with different experimental setups more susceptible to bulk motion.

Currently, a total of 85 IR preparation pulses were applied in each T1 Multitasking module, resulting in a single-slice scan of just over 4 minutes. However, the minimum required scan time was not systematically explored, so further shortening of the scan time may yet be possible.

Future work will include optimizing the number of cardiac bins, expanding spatial coverage with 3D volumetric imaging, as well as addressing B_1 and B_0 issues affecting T1 homogeneity in the inferior and lateral walls. Further imaging tests will also include using ECV Multitasking for longitudinal therapy monitoring, such as the cardiosphere-derived cell (CDC) treatment of HFpEF [89].

3.5 Conclusion

In this work, we developed an ECG-less, free-breathing CMR Multitasking ECV mapping method at high heart rates. The pre- and post-Gd data were concatenated and reconstructed using a joint T1 recovery model to generate ECV maps. Elevated ECV found in the HFpEF group agrees well with previous human studies and shows a moderate correlation with the histological data. This technique can serve as a viable MR imaging tool for myocardial tissue characterization in small animal models.

This chapter previously appeared as an article in Journal of Cardiovascular Magnetic Resonance. The original citation is as follows:

Han P, Zhang R*, Wagner S, Xie Y, Cingolani E, Marban E, Christodoulou AG†, Li D†. Electrocardiogram-less, free-breathing myocardial extracellular volume fraction mapping in small animals at high heart rates using motion-resolved cardiovascular magnetic resonance multitasking: a feasibility study in a heart failure with preserved ejection fraction rat model. Journal of Cardiovascular Magnetic Resonance. 2021;23(8):1-11.*

CHAPTER 4: Whole-brain Steady-state CEST at 3.0 T

4.1 Background

Chemical exchange saturation transfer (CEST) is a non-contrast MR imaging technique that indirectly detects exchangeable protons in the water pool by pre-saturation at different frequency offsets [34, 36, 32]. CEST MRI provides a novel contrast mechanism to image important physiological information, such as pH and metabolite concentration [96, 97]. It can be applied to detect and diagnose various pathologies, such as cancer [98], ischemia [36, 99], and lymphedema [100].

In conventional CEST imaging, each image readout is preceded by a frequency selective saturation module with long enough duration to reach the steady state between the exchanging proton pools and the water pool. Collecting images at different saturation frequency offsets generates the so-called Z-spectrum, which reflects the steady-state signal at sampled frequency offsets for a given saturation power. Wide, symmetric coverage of the Z-spectrum allows multi-pool analysis [63, 65], simultaneously revealing different CEST effects such as amide protein transfer (APT), relayed nuclear Overhauser enhancement (rNOE) effect, and other application-specific effects such as glycoCEST [52], CrCEST [101] and glycoNOE [55]. To achieve a reliable multi-pool analysis, dense sampling of the wide Z-spectrum is generally performed. Given the several dozen frequency offsets typically sampled, the acquisition duration (including the long saturation module) per frequency offset should ideally be limited to a few seconds in order to keep scan times acceptable for clinical practice. This time constraint typically allows only a single-shot k-space acquisition for each frequency offset after the saturation module. This

single-shot scheme makes fast, high-quality 3D CEST imaging a challenging technical goal.

One fast approach, the snapshot-CEST method [66], shortened scan times by optimizing the k-space sampling efficiency, such as using spiral-centric reordered k-space acquisition for snapshot gradient-echo (GRE) readout [67, 102] or 3D echo-planar-imaging (EPI) readout with CAIPIRINHA undersampling [68, 103]. It can provide 1.7 x 1.7 mm^2 in-plane resolution with an FOV of 220 x 180 x 54 mm^3 acquired in 7 sec per offset using 3D GRE readout, and 1.8 mm isotropic resolution with and FOV of 256 × 224 × 156 mm^3 acquired in 4.3 sec per offset using 3D EPI readout.

A potentially faster approach, the steady-state CEST (ss-CEST) method, performs pre-saturation and k-space sampling in an interleaved pattern with repeated modules [69, 70, 71, 35]. It ensures that the saturation exchange steady state is maintained most of the time within each frequency offset, and the interleaved pattern provides more flexibility in sequence design and possible acceleration. However, initial ss-CEST methods required more than 12 min to acquire the whole Z-spectrum, which is still too long for practical use. Recently, faster ss-CEST was explored in several studies. For instance, a new ss-CEST method combining the radial readout with multilinear singular value decomposition was proposed to further reduce the total scan time to be less than 5 min [72, 73]. Compared with previous ss-CEST approaches, the acquisition time per frequency offset was reduced from more than 10 sec to 7.6 sec [71]; however, the spatial coverage and in-plane resolution was compromised (from 2 x 2 x 2 mm^3 with >40 slices to 5 x 3 x 3 mm^3 with 15 slices). Another work explored fast 3D ss-CEST using segmented

3D EPI with incoherent undersampling in the k-ω space [74], generating whole-brain 1.8 mm isotropic CEST maps within 4 min.

Compared with EPI acquisition, ss-CEST with GRE acquisition is still slow despite its robustness to off-resonance and distortion. Therefore, we focus on the acceleration of GRE based ss-CEST in this work. In this study, we propose a novel 3D ss-CEST method at 3.0 T using MR Multitasking [104]. MR Multitasking is a low-rank-tensor (LRT) imaging strategy initially developed for quantitative cardiovascular imaging. We extend its application to CEST imaging in this work. With LRT modeling, the correlations among images acquired at different frequency offsets and among data during the approach to steady state are exploited to both reduce the scan time and enhance the image quality. This allows the Z-spectrum to be acquired with whole-brain coverage at 1.7 x 1.7 x 3.0 mm^3 spatial resolution within 5.5 min.

4.2 Methods

4.2.1 Data acquisition

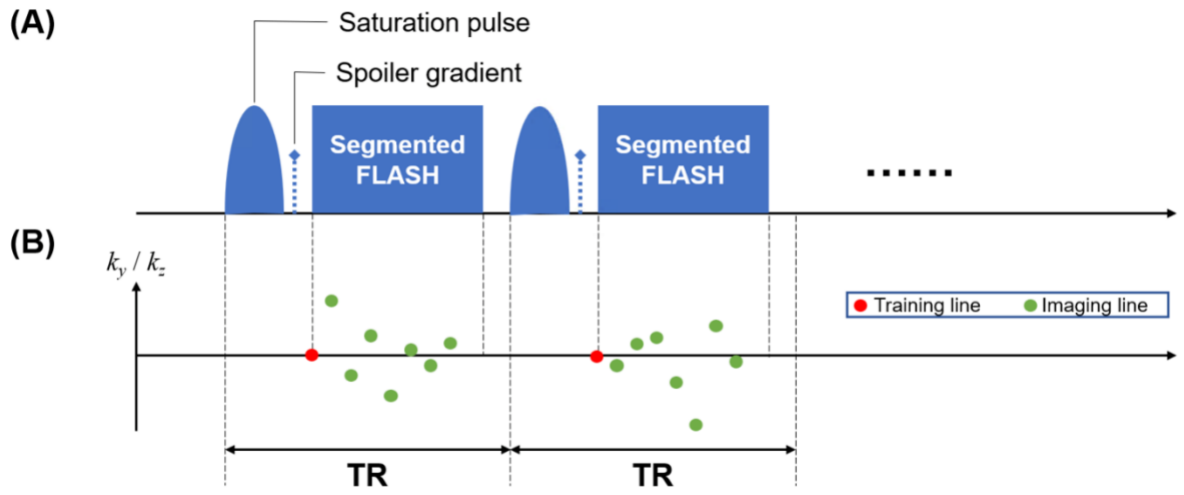

Figure 4.1: Illustration of the proposed Multitasking ss-CEST protocol. (a) Sequence design and (b) k-space sampling pattern.

Figure 4.1 illustrates the pulse sequence design and k-space sampling pattern of the proposed Multitasking ss-CEST protocol. The continuous-acquisition pulse sequence consists of repetitive ss-CEST modules. Each ss-CEST module contains a single-lobe Gaussian saturation pulse, followed by a spoiler gradient and eight fast low-angle shot (FLASH) readouts. The module repeated several times at each frequency offset in order to reach steady-state, and then switched to another frequency without any additional delay between modules. K-space lines were sampled using 3D Cartesian encoding. The center line ($k_y = k_z = 0$) was first sampled as "training data", and seven randomized lines with Gaussian distribution in k_y and k_z direction were then sampled as "imaging data" [104].

4.2.2 Image reconstruction

Images from the proposed protocol were represented in form as a 5D image $A(\mathbf{x}, \Delta\omega, \tau)$, where $\mathbf{x}$ is the voxel location in three spatial dimensions, $\Delta\omega$ indexes different frequency offsets of saturation pulses, and τ tracks the time within each frequency offset (indexing the approach to steady-state). The image was reshaped as a three-way tensor $\mathcal{A}$ (grouping together the three spatial dimensions into one mode and assigning $\Delta\omega$ and τ to the other two modes). Due to high correlation along each dimension, the tensor $\mathcal{A}$ can be modeled as low-rank and thus partially separable [105], e.g.

$$\mathcal{A} = \mathcal{G} \times_1 \mathbf{U}_\mathbf{x} \times_2 \mathbf{U}_{\Delta\omega} \times_3 \mathbf{U}_\tau \tag{4.1}$$

where $\times_i$ denotes the tensor i-mode product; $\mathbf{U}_\mathbf{x} \in \mathbb{C}^{J \times L_0}$ contains L_0 spatial basis functions with J voxels each, $\mathbf{U}_{\Delta\omega} \in \mathbb{C}^{K \times L_1}$ contains L_1 basis functions which characterize the Z-spectra, and $\mathbf{U}_\tau \in \mathbb{C}^{M \times L_2}$ contains L_2 temporal basis functions which characterize the signal evolution to reach steady-state within each frequency offset; $\mathcal{G} \in \mathbb{C}^{L_0 \times L_1 \times L_2}$

denotes the core tensor. The core tensor and temporal bases can be combined into a temporal factor tensor $\Phi = \mathcal{G} \times_2 \mathbf{U}_{\Delta\omega} \times_3 \mathbf{U}_{\tau}$, in which case Equation (4.1) simplifies to

$$\mathcal{A} = \Phi \times_1 \mathbf{U}_{\mathbf{x}} \tag{4.2}$$

Image reconstruction was done similarly to previous MR Multitasking works [106, 107, 7, 108], in two steps:

First, the components of the temporal factor tensor Φ were estimated from the training data $\mathbf{d}_{\mathrm{tr}}$. Using the known $\Delta\omega$ and τ indices, all the training data can also be reshaped into a three-way multichannel tensor $\mathcal{D}_{\mathrm{tr}}$ in $(\mathbf{k}, \Delta\omega, \tau)$-space, where the first mode comprises k-space locations $\mathbf{k}$ from all receiving coils. Then, $\mathcal{G}$, $\mathbf{U}_{\Delta\omega}$, and $\mathbf{U}_{\tau}$ were extracted from the higher-order singular value decomposition (HOSVD) of $\mathcal{D}_{\mathrm{tr}}$ [12].

Second, the spatial basis functions $\mathbf{U}_{\mathbf{x}}$ were determined from the imaging data $\mathbf{d}_{\mathrm{im}}$ by solving the following problem:

$$\widehat{\mathbf{U}}_{\mathbf{x}} = \arg\min_{\mathbf{U}_{\mathbf{x}}} \|\mathbf{d}_{\mathrm{im}} - \Omega(\Phi \times_1 \mathbf{E}\mathbf{U}_{\mathbf{x}})\|_2^2 + \lambda R(\mathbf{U}_{\mathbf{x}}) \tag{4.3}$$

where $\mathbf{E}$ is the signal encoding operator, including Fourier transform and coil sensitivity weightings; Ω is the undersampling operator; and $R(\cdot)$ is a regularization functional which was chosen here as a spatial total variation (TV) regularization term in order to additionally exploit compressed sensing.

4.2.3 CEST quantification

After the 5D image tensor $\mathbf{A}$ was fully reconstructed, a 4D image $\tilde{A}(\mathbf{x}, \Delta\omega)$ was extracted, consisting of the steady-state images at each frequency offset:

$$\tilde{A}(\mathbf{x}, \Delta\omega) = A(\mathbf{x}, \Delta\omega, \tau_{\max}) \tag{4.4}$$

where $\tau_{\max}$ is the last sampling time point at each frequency offset. $\tilde{A}(\mathbf{x}, \Delta\omega)$ was then used for further CEST analysis for each voxel $\mathbf{x}$ in the following steps:

1) Z-spectra generation. For each voxel $\mathbf{x} = \mathbf{x}_0$, the CEST signal $\tilde{A}(\mathbf{x}_0, \Delta\omega)$ was first normalized with the signal from unsaturated image $S_0(\mathbf{x}_0)$ (acquired at 300 ppm) to generate the Z-spectrum:

$$Z(\mathbf{x}_0, \Delta\omega) = \frac{\tilde{A}(\mathbf{x}_0, \Delta\omega)}{S_0(\mathbf{x}_0)} \tag{4.5}$$

2) B_0 correction. The central part of the Z-spectrum (nominal frequency offset $|\Delta\omega| < 1\text{ppm}$) was used to determine ΔB_0 with a Lorentzian model [109]. Z-spectra were then shifted for each voxel with corresponding ΔB_0.

3) Multi-pool Lorentzian fitting to generate isolated CEST contrasts. The four-pool model was employed, including APT (+3.5 ppm), rNOE (-3.5 ppm), semisolid magnetization transfer (MT, -1.0 ppm), and direct water saturation (DWS, 0 ppm) [63, 68]. The contribution of each pool is represented by a Lorentzian function:

$$L_i(\Delta\omega, A_i, W_i, C_i) = A_i \cdot \frac{W_i^2/4}{W_i^2/4 + (\Delta\omega - C_i)^2} \tag{4.6}$$

where $\Delta\omega$ is the frequency offset; A_i, W_i, C_i is the amplitude, width, and center frequency of the i-th Lorentzian curve ($i = 1, 2, 3, 4$). Then, the fitted Z-spectrum can be described as

$$f(\Delta\omega) = 1 - \sum_{i=1}^{4} L_i(\Delta\omega, A_i, W_i, C_i) \tag{4.7}$$

Eq. (7) was used to fit the Z-spectrum for each voxel using the MATLAB function *lsqnonlin*. The fitting parameters were listed in **Table 4.1**.

Table 4.1: Lorentzian fitting parameters. In this table, lb, ub, and x0 represent the lower bound, the upper bound, and the initial value of the fitting parameters correspondingly.

Pool i	DWS		rNOE		APT		MT	
Parameter	A_1	W_1	A_2	W_2	A_3	W_3	A_4	W_4
lb	0.6	0.5	0.0	1.0	0.0	1.0	0.0	30.0
ub	1.0	6.0	0.2	12.0	0.2	8.0	0.3	100.0
x0	0.8	2.3	0.1	4.0	0.05	3.0	0.15	60.0

4.2.4 In-vivo experiments

The experiment was approved by the institutional review board of Cedars-Sinai Medical Center. Written informed consent was obtained for all participating subjects. Data were acquired in six (n = 6) healthy volunteers on a 3.0 T MR system (MAGNETOM Vida, Siemens Healthcare, Erlangen, Germany) with a 1Tx/16Rx-channel head/neck coil.

For the proposed Multitasking ss-CEST protocol, CEST parameters were (**Figure 4.1**): TR = 70 ms, saturation pulse duration t_{sat} = 30 ms, saturation pulse flip angle = 500° (effective B_1 = 0.93 μT [110]), FA = 5° for FLASH readouts. The module was repeated 80 times at each frequency offset (5.6 sec in total), and then switched to another frequency without delay. Other parameters were: FOV = 220 x 220 x 120 mm^3, matrix size = 128 x 128 x 40, spatial resolution = 1.7 x 1.7 x 3.0 mm^3. Images of 53 frequency offsets (-100, -40, -30, -20, -15, -10, -9.0, -8.0, -7.0, -6.5, -6.0, -5.5, -5.0, -4.5, -4.0, -3.5, -3.0, -2.5, -2.0, -1.5, -1.0, -0.8, -0.6, -0.4, -0.2, -0.1, 0, 0.1, 0.2, 0.4, 0.6, 0.8, 1.0, 1.5, 2.0, 2.5, 3.0, 3.5, 4.0, 4.5, 5.0, 5.5, 6.0, 6.5, 7.0, 8.0, 9.0, 10, 15, 20, 30, 40, 100 ppm) were acquired from upfield to downfield, with two prolonged unsaturated acquisition S_0 (300 ppm) at the beginning and the end. The total imaging time was 5 min 30 s.

Single-slice single-shot FLASH CEST images were acquired as a reference. The frequency offsets were sampled as in ss-CEST. A train of 30 Gaussian pulses of t_{sat} = 30 ms (duty cycle = 50%) and flip angle = 200° were used for saturation. Other parameters were: slice thickness = 10 mm, TR/FA = 3000 ms/5°, 2 averages. The total imaging time was 5 min 54 s for one slice.

T1w images were also acquired with the same image center, FOV, and slice thickness with the 3D ss-CEST protocol for gray matter (GM) and white matter (WM) segmentation.

To test the intra-session repeatability of the protocol, the same Multitasking ss-CEST sequence were performed twice at the same location in four (n = 4) volunteers.

4.2.5 Image analysis

All image reconstruction and image processing were performed with MATLAB R2018a (MathWorks, Natick, Massachusetts, USA) on a Linux workstation with two 2.7-GHz 12-core Intel Xeon CPUs, one NVIDIA Quadro K6000 GPU, and 256 GB RAM.

CEST quantification was done for both 3D Multitasking ss-CEST images and 2D single-shot FLASH CEST images as described in previous sections. Segmented WM and GM in the central slice were selected as regions of interest (ROIs) for statistical analysis. WM/GM segmentation was performed with FSL [111] upon T1w images. The mean values of APT, rNOE, and MT maps of each subject within GM and WM regions were compared between the proposed 3D Multitasking ss-CEST method and 2D single-shot FLASH CEST method. Statistical graphs were generated with GraphPad Prism 8 (GraphPad Software, La Jolla, California, USA).

4.3 Results

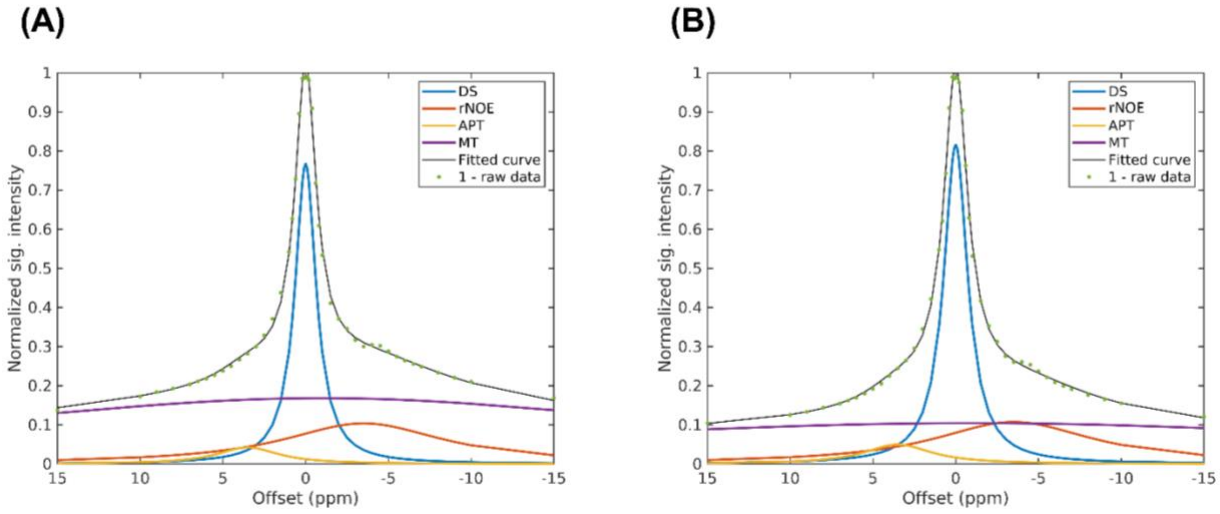

Figure 4.2: Representative Z-spectra from **(A)** the white matter (WM) region and **(B)** the grey matter (GM) region of a healthy volunteer. For convenience, raw data (the green dots in the figure) were plotted as $1 - Z(\Delta\omega)$.

Representative Z-spectra between -15 ppm and 15 ppm are shown in **Figure 4.2A, B** for WM and GM respectively. It can be clearly seen in the figure that the MT effect was more significant in WM than in GM, which is consistent with previous studies [67, 68].

Figure 4.3 shows representative **(A)** B_0 estimation result, **(B)** MT map, **(C)** rNOE map, and **(D)** APT maps of the proposed Multitasking ss-CEST method from one healthy volunteer. The image quality was consistent among different slices. **Figure 4.4** shows the comparison between rNOE, APT, and MT maps generated from the proposed Multitasking ss-CEST method and the 2D single-shot FLASH CEST method. While fitted rNOE, APT and MT values were generally consistent with each other (also see **Figure 4.5**), maps from the proposed method were less noisy than those from the reference 2D single-shot FLASH method.

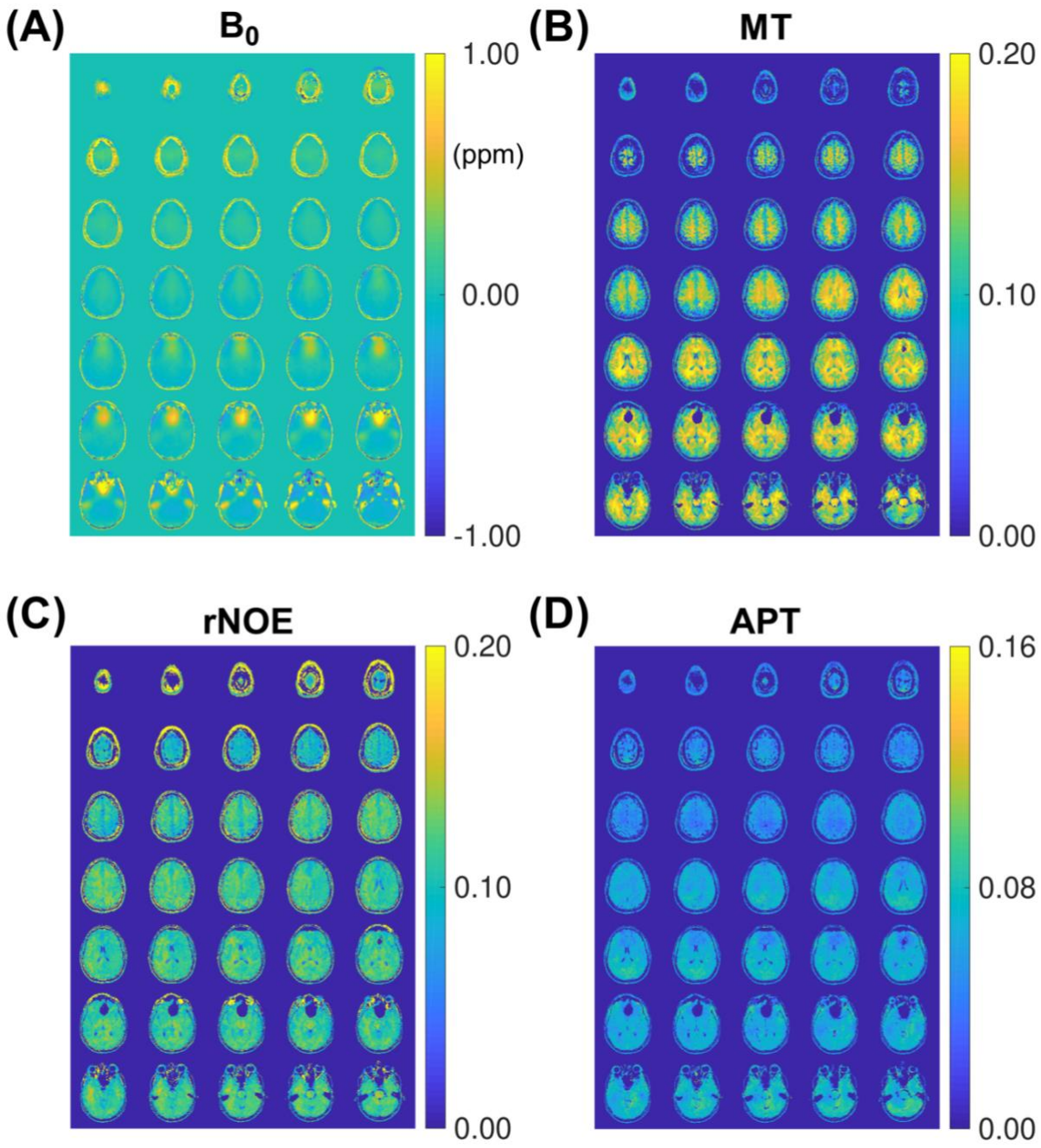

Figure 4.3: Representative B_0 estimation results and MT, rNOE, APT maps of the proposed Multitasking ss-CEST method (From A to D: B_0, MT, rNOE, APT). 35 out of 40 slices are presented here. The outermost 5 slices are discarded for display because the aliasing at the boundary makes the fitting result less reliable.

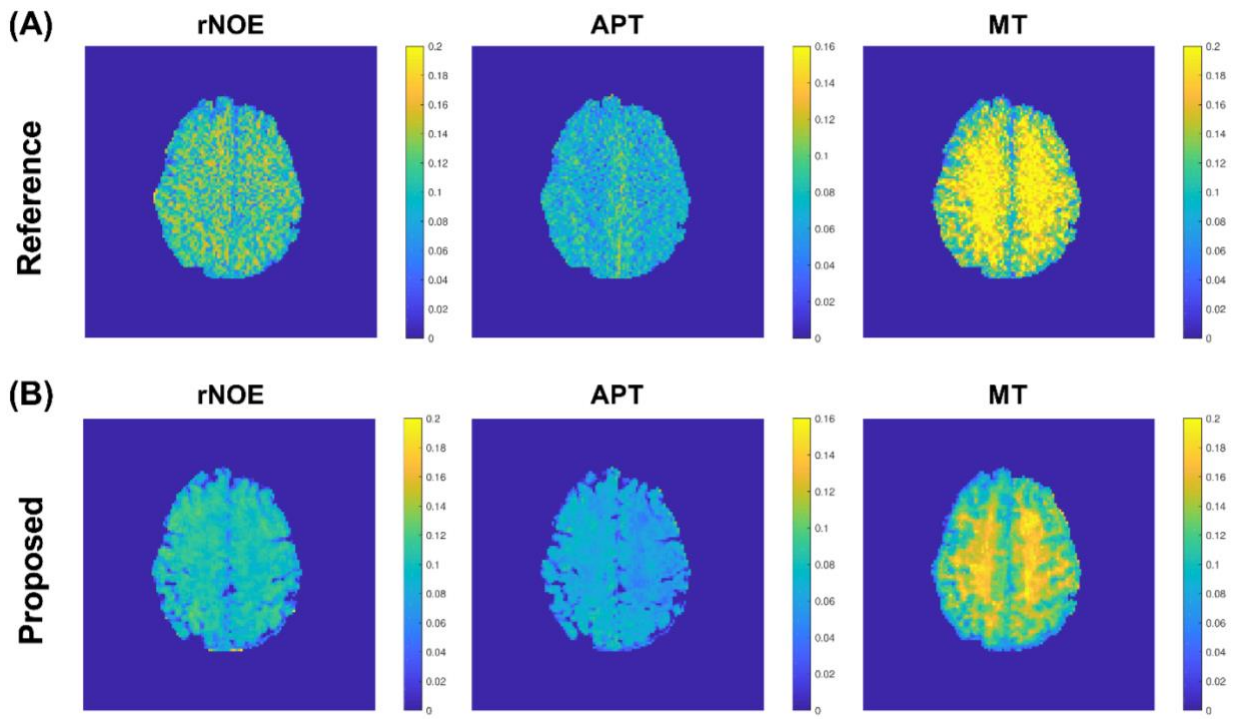

Figure 4.4: Comparison between maps generated from **(A)** the 2D single-shot FLASH method and **(B)** the proposed Multitasking ss-CEST method. Note that the slice thickness of 10mm used in the 2D single-shot FLASH CEST method was larger than 3mm in the proposed 3D Multitasking ss-CEST method. Therefore, though the center of the slice matched between (A) and (B), the spatial coverages were not completely the same.

Statistics of mean Lorentzian amplitudes within WM and GM regions among different volunteers are presented in **Figure 4.5**. As shown in **Figure 4.5A**, the mean amplitude was consistent among healthy subjects. Contrast ratios of WM:GM for rNOE, APT and MT amplitudes were 1.12, 1.07 and 1.31 from the proposed Multitasking ss-CEST method, near to the reference values of 1.13, 0.94, and 1.35 from the 2D single-shot FLASH CEST method. Note that the saturation powers used in the proposed Multitasking ss-CEST method (saturation pulse flip angle = 500°) and the reference the 2D single-shot FLASH CEST method (saturation pulse flip angle = 200°) were different, since a higher B_1 is usually needed in steady-state CEST acquisition to achieve comparable CEST effects in conventional CEST acquisition [35]. Even with the saturation

power adjustment, the established “steady state” at data acquisition were different between the proposed method and the reference method, which may contribute to the difference in fitted rNOE, APT, MT amplitudes and corresponding WM/GM contrast ratios. The mean values of fitted rNOE, APT and MT amplitudes in WM and GM regions for each volunteer are shown in **Figure 4.6**.

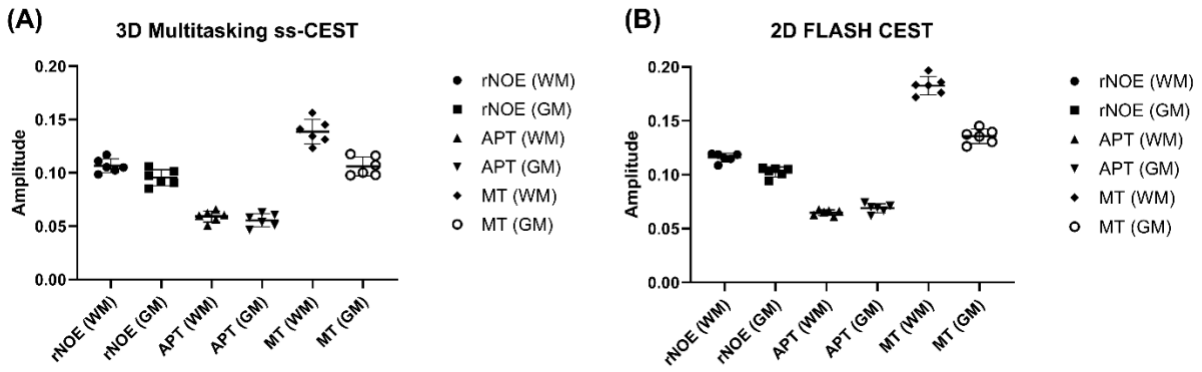

(C)

	rNOE		APT		MT	
(All in %)	WM	GM	WM	GM	WM	GM
Multitasking ss-CEST	10.66 ± 0.65	9.55 ± 0.76	5.92 ± 0.53	5.55 ± 0.62	13.86 ± 1.15	10.62 ± 0.89
Single-shot FLASH CEST	11.59 ± 0.41	10.25 ± 0.46	6.48 ± 0.26	6.89 ± 0.42	18.26 ± 0.85	13.57 ± 0.67

Figure 4.5: Average Lorentzian amplitudes within WM and GM regions among different volunteers. The mean amplitude is consistent among healthy subjects with **(A)** the proposed method and **(B)** the reference method. **(C)** Contrast ratios of WM:GM for rNOE/APT/MT: 1.12/1.07/1.31 (Multitasking ss-CEST) vs. 1.13/0.94/1.35 (2D single-shot FLASH CEST).

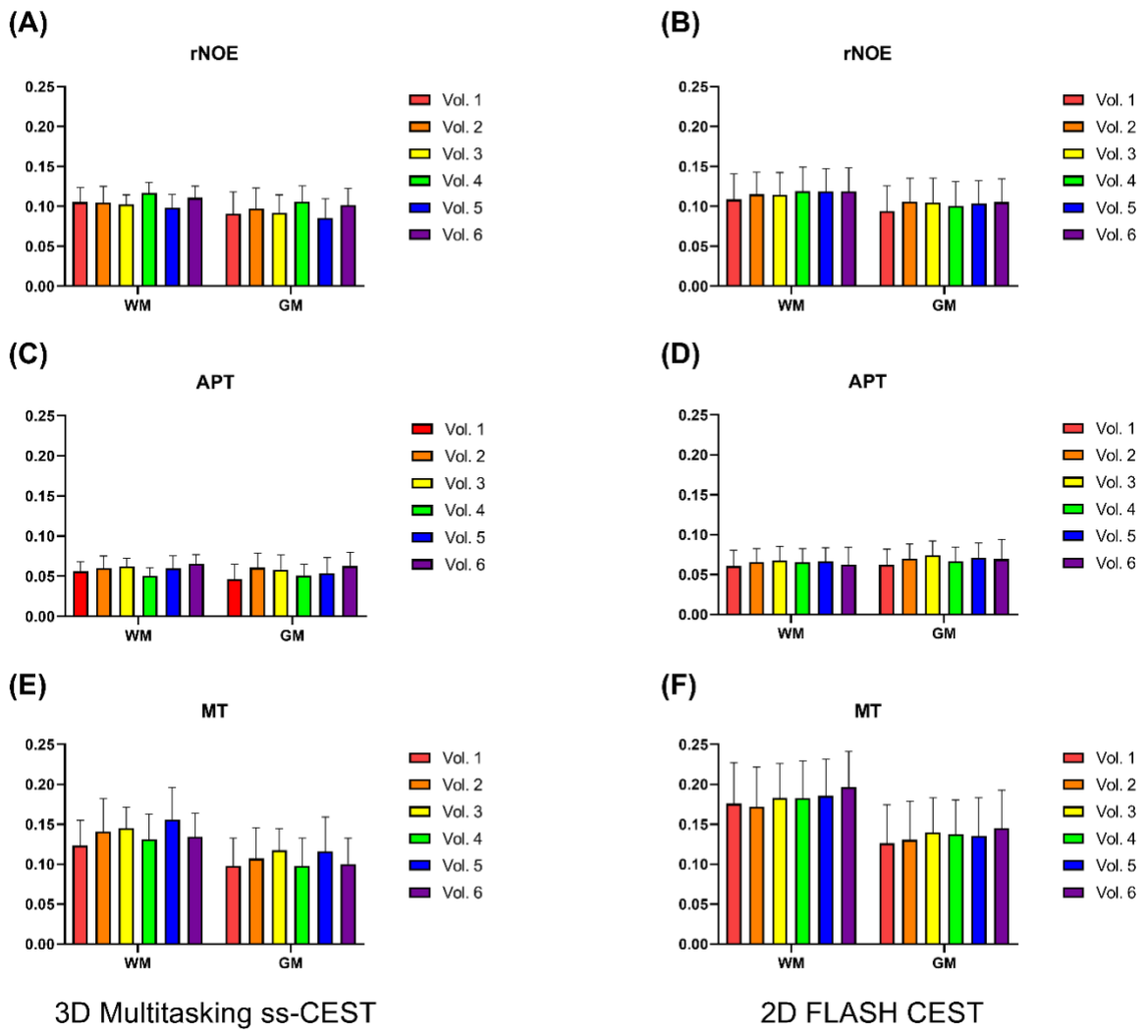

Figure 4.6: The mean and standard deviation of fitted amplitudes of rNOE, APT and MT for each volunteer. (A/C/E) are results from the proposed 3D Multitasking ss-CEST protocol, (B/D/F) are results from the reference 2D FLASH CEST protocol.

The intra-session repeatability results for each of the three volunteers are displayed in **Figure 4.7**. The Coefficient of Variation (CoV) of rNOE, APT, and MT (considering the values in both GM and WM) were 5.1%, 8.9%, and 9.2% [112].

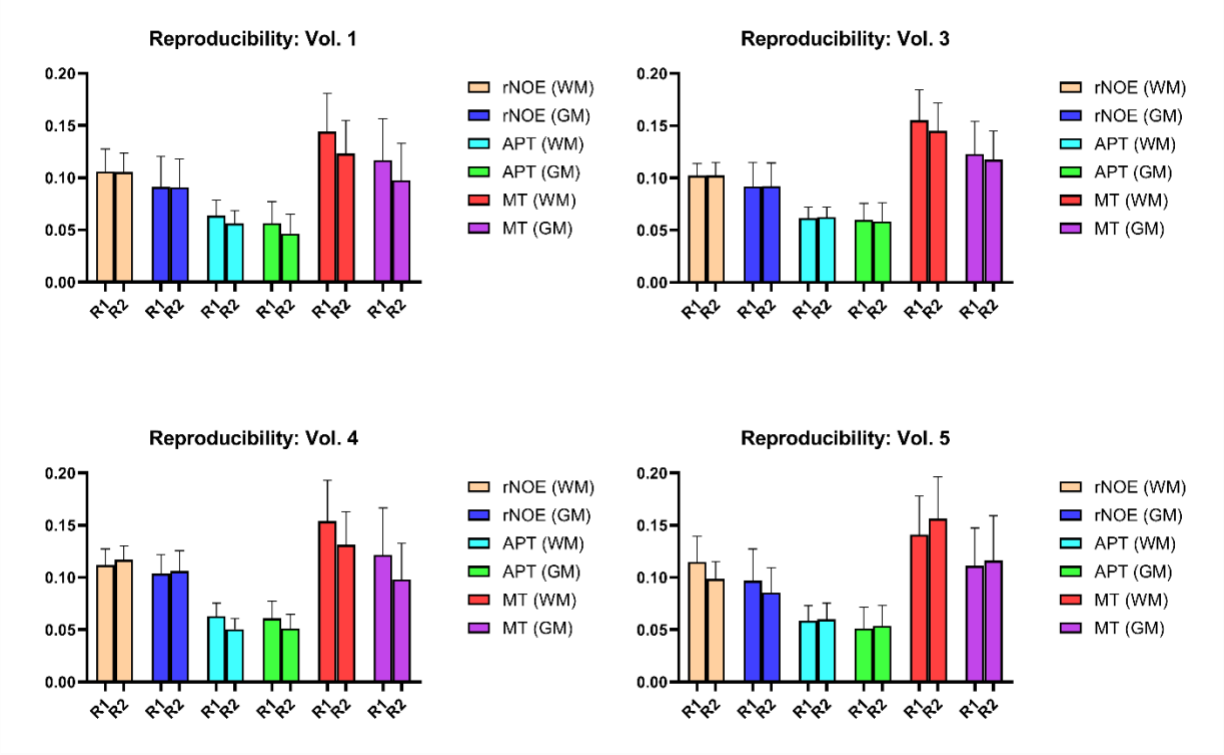

Figure 4.7: Comparison of fitted rNOE, APT, MT amplitudes (mean ± SD) from two scans (R1/R2) per subject in four subjects. The two scans were performed in the same day, and the sequence parameters and the imaging location were the same.

4.4 Discussion

We developed a novel 3D steady-state CEST method with whole-brain coverage using MR Multitasking. 3D Images of 55 different frequency offsets (including unsaturated ones) were acquired within 5.5 min covering an FOV of 220 x 220 x 120 mm^3 at a spatial resolution of 1.7 x 1.7 x 3.0 mm^3. The time to acquire the data for each frequency offset was 5.6 seconds. It is more time efficient than previous GRE based methods considering the spatial coverage and the spatial resolution [66, 67, 113].

In contrast to the single-shot acquisition method (or the pseudo-steady-state method) [35], the ss-CEST method ensures that the steady state of the chemical exchanging process is maintained during most of the acquisition time. It allows continuous

acquisition for more efficient traversal of k-space than the single-shot method. Nonetheless, the only additional source of acceleration in the original ss-CEST implementation was limited to parallel imaging.

Low-rankness in spatiospectral signals has been exploited in previous work such as the SPICE method [114] and the Multilinear Singular Value Decomposition (MLSVD) method [73]. In SPICE, the spectroscopic image is modeled as a low-rank matrix to accelerate image acquisition. It was designed for spectroscopic imaging but has not been explored for CEST imaging. The MLSVD method performs post-processing denoising of CEST images by enforcing low-rankness of individual spatial dimensions versus a frequency offset dimension. In contrast, the low-rank tensor model in MR Multitasking enforces low-rankness of a combined spatial dimension (thereby imposing no assumption on spatial structure) versus two individual sequence parameter dimensions: frequency offset and time since frequency increment. Furthermore, Multitasking imposes this model during image reconstruction to accelerate acquisition. In addition to accelerating the acquisition, the Multitasking ss-CEST method has two additional advantages: (1) the approach to the steady state at each frequency offset is modeled and the signal before the steady state is excluded, allowing uncorrupted steady-state values to be used for quantification; (2) the Z-spectra are automatically denoised with the low-rank constraint. Given enough spatiotemporal correlation, the only explicit limiting factor of acceleration becomes the time required to reach steady state at each frequency offset.

In this work, 53 different frequency offsets were sampled between -100 ppm and 100 ppm. In fact, though all the data were reconstructed jointly, not all the frequency offsets were needed in the multi-pool fitting process. The quantitative CEST maps

reported in this paper were fitted using only the data from -20 ppm to 20 ppm (after B_0 correction). However, those outer frequency offsets, even not used for fitting, are still important in this protocol. Note that the frequency offset is switched from one to another without water signal recovery during the continuous scan. Generally, the time to reach the steady state is shorter if the gap between two adjacent sampling frequency offsets is closer. Therefore, outer frequency offsets (e.g., ±30, ±40, and ±100 ppm) were sampled to “bridge the gap” between unsaturated images and saturated images, so that the steady state could be reached quickly at the following frequency offset [70].

Certain inhomogeneities are present in APT images (**Figure 4.3D**), correlated to B_0 inhomogeneities in **Figure 4.3A**. There is possibility of either incomplete B_0 correction or incorrect modeling of B_0 inhomogeneities in the low-rank model. A locally low-rank approach [115] may model the effects of smooth B_0 inhomogeneity more efficiently, which will be explored in future work. Furthermore, the use of advanced active shimming coils may potentially provide better B_0 shimming to reduce B_0 inhomogeneity during image acquisition [116, 117].

B_1 correction [118, 119] was not performed in this feasibility study. This may increase the variability of the CEST quantification results within the same tissue. Therefore, the influence of B_1 inhomogeneity on the reliability of quantitative CEST maps needs to be evaluated before exploring the clinical applications of the proposed technique.

A 4-pool Lorentzian fitting method was used to quantify the CEST effects, as in Mueller et al. [68]. Different fitting methods have been used previously, such as the Lorentzian difference (LD) method [67, 120, 121] or the PLOF method [72, 122]. Moreover, a different number of pools were fitted in the studies. Therefore, a standard fitting method

which is generally accepted is still not established. Also, in previous works at 3.0 T, different B_1 values were chosen. Some representative effective B_1 were 0.6 μT [67], 0.65 μT [68], 0.76 μT [72], and a peak B_1 of 2 μT was used in several studies [74, 123]. In this work, we use a Gaussian saturation pulse with flip angle = 500° (peak B_1 = 2.15 μT, effective B_1 = 0.93 μT), which is slightly higher to balance the SNR of the spatial subspace images in MR Multitasking reconstruction and the visibility of the CEST effect in the steady-state acquisition of Z-spectra. Both the choice of accurate CEST fitting method and the optimization of B_1 are important questions to explore, but are beyond the scope of this work.

There are several potential improvements to explore in the near future. First, advanced k-space sampling trajectories may be exploited. For instance, non-Cartesian trajectories such as spirals have the potential to improve the sampling efficiency and incoherence over Cartesian acquisition, further reducing the scan time and enhancing the image quality. Second, the sampling pattern of specific frequency offsets can be further optimized to reduce the total number of sampled frequencies, so that the total scan time may be reduced while maintaining the reliability and robustness of the multi-pool fitting. Also, given that the sampling pattern of one “training line” every 70 ms resembles self-gated acquisition used for MR Multitasking in the heart and abdomen, the current ss-CEST protocol has the potential to also be applied to moving organs, such as free-breathing abdominal CEST.

4.5 Conclusion

Three-dimensional steady-state CEST with whole-brain coverage can be done at 3.0 T with a total scan time of 5.5 min and a spatial resolution of 1.7 x 1.7 x 3.0 mm^3 using

MR Multitasking. Repeatable APT and rNOE maps were generated using the proposed method. This method has the potential to enable fast and high-quality 3D CEST imaging at clinical field strength.

This chapter previously appeared as an article in Magnetic Resonance in Medicine. The original citation is as follows:

Han P, Cheema K, Lee HL, Zhou Z, Cao T, Ma S, Wang N, Han H, Christodoulou AG†, Li D†. Whole-brain steady-state CEST at 3 T using MR Multitasking. Magnetic Resonance in Medicine. 2022 May;87(5):2363-71.

CHAPTER 5: Free-breathing 3D CEST MRI of Human Liver at 3.0 T

5.1 Background

Chemical exchange saturation transfer (CEST) imaging is a novel MRI technique that allows indirect detection of exchangeable protons in the water pool. In recent years, several studies have explored various CEST applications in the liver, such as amide proton transfer weighted (APTw) imaging [53, 54, 124, 125], glycogen CEST (glycoCEST) imaging [53, 54], glycogen NOE (glycoNOE) imaging [55], and extracellular pH measurement with Ioversol injection [126, 127], to list a few examples. However, CEST MRI of the liver in human studies is still challenging. Breath-holding is currently needed to reduce motion artifacts, which limits not only spatial resolution, but also scan volume coverage: even with multiple breath holds, 3D coverage would require an impractically long scan time.

Steady-state CEST (ss-CEST) is a method that performs pre-saturation and k-space sampling in an interleaved pattern with repeated modules [69, 70]. In the previous chapter, we developed a ss-CEST method in the brain using MR Multitasking to accelerate image acquisition and enhance image quality [133]. In this work, we propose a novel respiration-resolved 3D abdominal Multitasking ss-CEST technique at 3.0 T, which enables whole-liver coverage with free-breathing acquisition. The feasibility of the proposed technique was tested in healthy volunteers. The sensitivity of APTw and glycoCEST measurements between post-overnight-fasting and post-meal imaging were evaluated with fasting experiments.

5.2 Methods

5.2.1 Sequence design

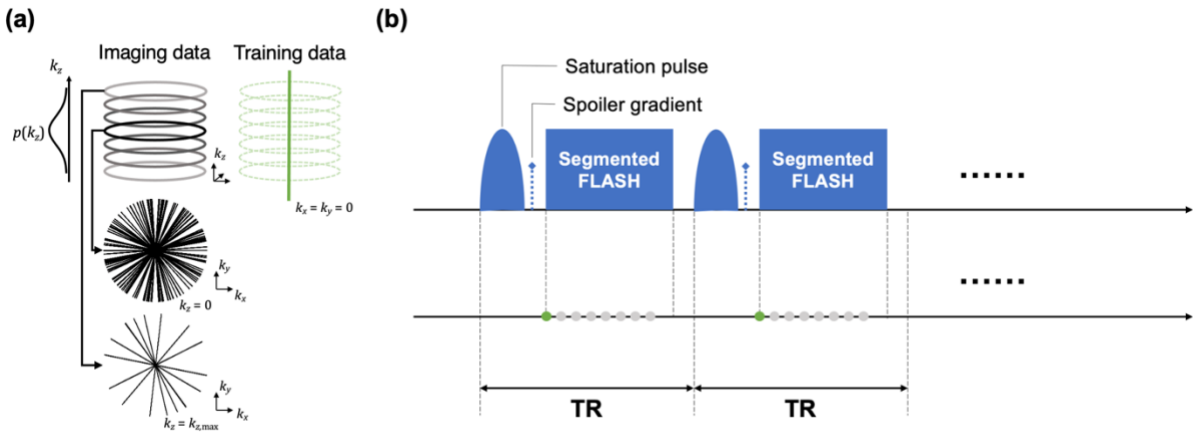

Figure 5.1: K-space sampling pattern and sequence structure of the abdominal Multitasking ss-CEST sequence. **(a)** The k-space is continuously sampled using a stack-of-stars FLASH sequence with golden angle ordering in the x-y plane and Gaussian-density randomized ordering in the z direction, interleaved with training data (central k-space line along z-direction) every 8th readout. **(b)** Each ss-CEST module contains a single-lobe Gaussian saturation pulse, followed by a spoiler gradient and eight readouts.

The continuous-acquisition pulse sequence consists of repetitive ss-CEST modules. Each ss-CEST module contains a single-lobe Gaussian saturation pulse, followed by a spoiler gradient and eight fast low-angle shot (FLASH) readouts, as in **Figure 5.1**. FLASH readout with the option 'water excitation only' was used for fat suppression. The total time of one ss-CEST module is 72 ms, consisting of 30 ms for the saturation pulse and 42 ms for right FLASH readouts. The module repeated several times at each frequency offset until the steady state is reached and maintained, and then switched to another frequency without any additional delay between modules.

Images were acquired in axial orientation covering the whole liver region. K-space lines were sampled using a stack-of-stars acquisition pattern. In each ss-CEST module,

the center k-space line was first sampled as “training data” to estimate temporal basis functions, and seven k-space lines with golden angle ordering in-plane and Gaussian-density randomized ordering in the partition direction were sampled as “imaging data” to recover spatial basis functions. In this work, the training data was acquired in the superior-inferior direction ($k_x = k_y = 0$) to detect respiratory motion with more sensitivity.

5.2.2 Image reconstruction

Image model

The abdominal CEST image is modeled as a 6D image $a(\mathbf{x}, z, \tau, r)$, where $\mathbf{x}$ is the voxel location in three spatial dimensions, z indexes the pre-saturation frequency offset, τ tracks the time within each frequency offset (indexing the approach to steady-state), and r represents the respiratory motion phase. Due to high correlation along all dimensions, the image can be modeled as a 4-way low-rank tensor $\mathcal{A}$:

$$\mathcal{A} = \mathcal{G} \times_1 \mathbf{U}_\mathbf{x} \times_2 \mathbf{U}_z \times_3 \mathbf{U}_\tau \times_4 \mathbf{U}_r \tag{5.1}$$

where $\times_i$ denotes the tensor i-mode product; $\mathbf{U}_\mathbf{x} \in \mathbb{C}^{J \times L_0}$ contains L_0 spatial basis functions with J voxels each, $\mathbf{U}_z \in \mathbb{C}^{K \times L_1}$ contains L_1 basis functions characterizing the Z-spectra, $\mathbf{U}_\tau \in \mathbb{C}^{M \times L_2}$ contains L_2 temporal basis functions characterizing the signal evolution to reach steady-state within each frequency offset, and $\mathbf{U}_r \in \mathbb{C}^{P \times L_3}$ contains L_3 temporal basis functions characterizing the respiratory motion; $\mathcal{G} \in \mathbb{C}^{L_0 \times L_1 \times L_2 \times L_3}$ denotes the core tensor. The core tensor and temporal bases can be combined into a temporal factor tensor $\Phi = \mathcal{G} \times_2 \mathbf{U}_z \times_3 \mathbf{U}_\tau \times_4 \mathbf{U}_r$, in which case Equation (5.1) simplifies to

$$\mathcal{A} = \Phi \times_1 \mathbf{U}_\mathbf{x} \tag{5.2}$$

Tensor subspace estimation

Components of the temporal factor tensor $\Phi = \mathcal{G} \times_2 \mathbf{U}_z \times_3 \mathbf{U}_\tau \times_4 \mathbf{U}_r$ were estimated from the training data $\mathbf{d}_{\mathrm{tr}}$ with tensor subspace estimation. The training data $\mathbf{d}_{\mathrm{tr}}$ can be reshaped into a three-way multichannel tensor $\mathcal{D}_{\mathrm{tr}}$ in $(\mathbf{k}, z, \tau, r)$-space, where the first mode comprises k-space locations $\mathbf{k}$ from all receiving coils, z and τ represent the temporal indices which can be read naturally from chronological order, and r indicates the respiratory motion state. In this work, the respiratory motion state was binned into 5 states with the help of recorded Siemens Physiologic Monitoring Unit (PMU) data, which was extracted from the raw data.

A dictionary of full-course signal curves was generated ahead of time with Bloch simulation. The dictionary consists of 41 T1 values of the water pool logarithmically spaced from 100 ms to 3000 ms and 18 exchange rates (k_{ex}) of the APT pool at 3.5 ppm linearly spaced from 100 ms to 3000 ms. The temporal factor $\mathbf{U}_\tau$ which characterizes the signal evolution to reach steady-state was predetermined from the SVD of this dictionary.

The undersampled tensor $\mathcal{D}_{\mathrm{tr}}$ was first completed by solving (also see Section 2.1.3):

$$\widehat{\mathcal{D}}_{\mathrm{tr}} = \arg \min_{\mathbf{D}_{\mathrm{tr},(2)} \in \mathrm{span}\{\mathbf{U}_z\}} \|\mathbf{d}_{\mathrm{tr}} - \Omega_{\mathrm{tr}}(\mathcal{D}_{\mathrm{tr}})\|_2^2 + \lambda \sum_{i=1,3,4} \left\|\mathbf{D}_{\mathrm{tr},(i)}\right\|_* \tag{5.3}$$

where $\mathbf{d}_{\mathrm{tr}}$ is the sampled training data, $\mathbf{D}_{\mathrm{tr},(i)}$ is the mode-*i* matricization of the tensor $\mathcal{D}_{\mathrm{tr}}$, d$\|\cdot\|_*$ denotes the nuclear norm, λ is the weighting parameter, and Ω_{tr} indicates that only the $\mathcal{D}_{\mathrm{tr}}$ with sampled index combinations are considered in the data fidelity term.

With the completed $\widehat{\mathcal{D}}_{\mathrm{tr}}$, the core tensor $\mathcal{G}$, respiratory basis functions $\mathbf{U}_r$, and Z-spectra characterization basis functions $\mathbf{U}_z$ can be extracted from the higher-order SVD (HOSVD) of $\mathcal{D}_{\mathrm{tr}}$, which finally recovers $\Phi = \mathcal{G} \times_2 \mathbf{U}_z \times_3 \mathbf{U}_\tau \times_4 \mathbf{U}_r$.

Spatial coefficient recovery

After recovering $\Phi = \mathcal{G} \times_2 \mathbf{U}_z \times_3 \mathbf{U}_\tau \times_4 \mathbf{U}_r$, the spatial basis functions $\mathbf{U}_\mathbf{x}$ were determined from the imaging data $\mathbf{d}_{\mathrm{im}}$ by solving the following problem:

$$\widehat{\mathbf{U}}_\mathbf{x} = \arg\min_{\mathbf{U}_\mathbf{x}} \|\mathbf{d}_{\mathrm{im}} - \Omega(\Phi \times_1 \mathbf{E}\mathbf{U}_\mathbf{x})\|_2^2 + \lambda R(\mathbf{U}_\mathbf{x}) \tag{5.4}$$

where $\mathbf{E}$ is the signal encoding operator, including Fourier transform and coil sensitivity weightings; Ω is the undersampling operator; and $R(\cdot)$ is a regularization functional which was chosen here as a spatial wavelet regularization term in order to additionally exploit compressed sensing.

5.2.3 CEST analysis

After the image tensor $\mathcal{A}$ was fully reconstructed, a 4D image $\tilde{A}(\mathbf{x}, z)$ was extracted, consisting of the steady-state images at each frequency offset:

$$\tilde{A}(\mathbf{x}, z) = A\big(\mathbf{x}, z, \tau_{\max}, r_{\mathrm{opt}}\big) \tag{5.5}$$

where $\tau_{\max}$ is the last sampling time point (or the average of all time points when the steady state is reached) at each frequency offset, and r_{opt} is the optimal respiratory phase. $\tilde{A}(\mathbf{x}, \Delta\omega)$ was then used for further CEST analysis for each voxel $\mathbf{x}$ in the following steps:

1) Z-spectra generation. For each voxel $\mathbf{x} = \mathbf{x}_0$, the CEST signal $\tilde{A}(\mathbf{x}_0, z)$ was first normalized with the signal from unsaturated image $S_0(\mathbf{x}_0)$ (acquired at 300 ppm) to generate the Z-spectrum:

$$Z(\mathbf{x}_0, z) = \frac{\tilde{A}(\mathbf{x}_0, z)}{S_0(\mathbf{x}_0)} \tag{5.6}$$

2) B_0 correction. The central part of the Z-spectrum (nominal frequency offset $|\Delta\omega| < 1\text{ppm}$) was used to determine ΔB_0 with a Lorentzian model [109]. Z-spectra were then shifted for each voxel with corresponding ΔB_0.

3) Asymmetry analysis. The CEST effect was quantified with the magnetization transfer asymmetry ratio (MTR_{asym}):

$$\text{MTR}_{\text{asym}}(\Delta\omega) = Z(-\Delta\omega) - Z(\Delta\omega) \tag{5.7}$$

where $\Delta\omega$ is the frequency offset. APTw values were quantified as MTR_{asym} at $\Delta\omega = 3.5\text{ ppm}$, while glycoCEST values were quantified as the average MTR_{asym} of 0.6, 0.8, 1.0, 1.2, and 1.4 ppm.

5.2.4 In-vivo experiments

The experiment was approved by the institutional review board of Cedars-Sinai Medical Center. Written informed consent was obtained for all participating subjects. Data were acquired in seven (n = 7) healthy volunteers (four males + three females, mean age = 37.1 y, age range 21–59 y). To test the sensitivity of the proposed CEST imaging protocol to fasting and compared with previous methods [55, 124, 54], two separate scans were done for each volunteer: a ‘post-meal’ scan which was done 1.5 hours after a full lunch, and a ‘post-fasting’ scan which was done after overnight (more than 12 hours) fasting.

MRI data were acquired on a Siemens 3T MR system (MAGNETOM Vida, Siemens Healthcare, Erlangen, Germany) with an 18-channel phase array body coil. Imaging parameters were: FOV = 512 x 512 x 192 mm^3, matrix size = 256 x 256 x 32, spatial resolution = 2.0 x 2.0 x 6.0 mm^3. CEST parameters were: saturation pulse flip angle = 500° (effective B_1 = 0.93 μT), FA = 5° for FLASH readouts. The module was

repeated 128 times at each frequency offset (9.2 sec in total), and then switched to another frequency without delay. Images of 53 frequency offsets (-40.0, -30.0, -20.0, -15.0, -10.0, -9.0, -8.0, -7.0, -6.0, -5.5, -5.0, -4.5, -4.0, -3.5, -3.0, -2.5, -2.0, -1.7, -1.4, -1.2, -1.0, -0.8, -0.6, -0.4, -0.2, -0.1, 0, 0.1, 0.2, 0.4, 0.6, 0.8, 1.0, 1.2, 1.4, 1.7, 2.0, 2.5, 3.0, 3.5, 4.0, 4.5, 5.0, 5.5, 6.0, 7.0, 8.0, 9.0, 10.0, 15.0, 20.0, 30.0, 40.0 ppm) were acquired from upfield to downfield, with prolonged unsaturated acquisition S_0 (300 ppm) at the beginning and the end. The total imaging time was 9 min.

5.2.5 Image analysis

All image reconstruction and image processing were performed with MATLAB R2018a (MathWorks, Natick, Massachusetts, USA) on a Linux workstation with two 2.7-GHz 12-core Intel Xeon CPUs, one NVIDIA Quadro K6000 GPU, and 256 GB RAM.

ROIs were manually drawn to include the liver region in the central slice of the imaging volume. The boundary of the liver was excluded from the ROIs to avoid severe B_0 inhomogeneities. For each scan, single APTw and glycoCEST values were reported as mean ± standard deviation (SD) within the ROI.

Wilcoxon signed rank test was performed to compare mean APTw and glycoCEST values in post-fasting and post-meal scans. A two-tailed value of $p < 0.05$ was considered to be statistically significant. The repeatability was evaluated by performing the Bland-Altman plot. Statistical graphs were generated using GraphPad Prism 8 (GraphPad Software, La Jolla, California, USA).

5.3 Results

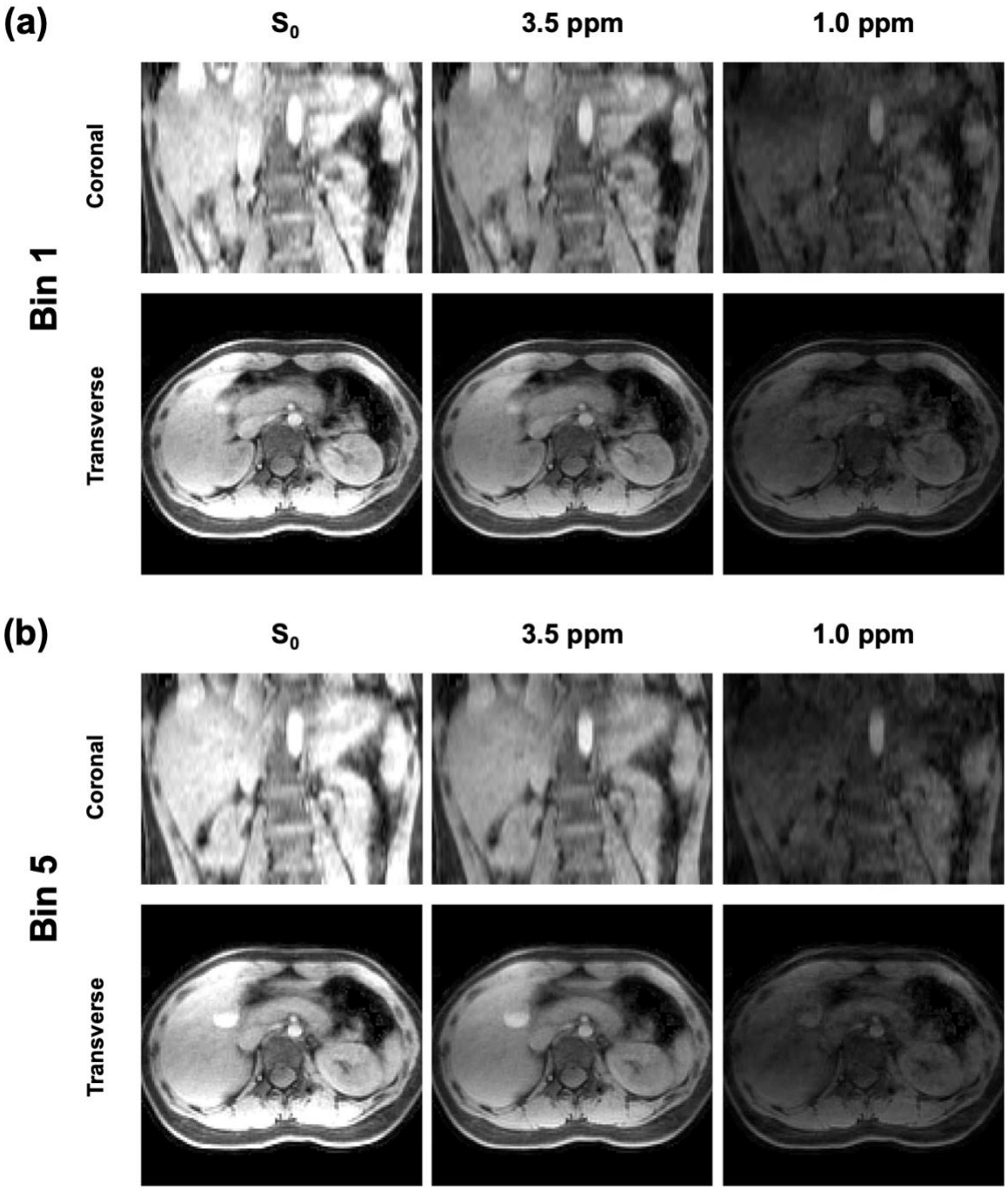

Figure 5.2: Representative 5D CEST images at steady-state of a healthy volunteer from a post-fasting scan, with 3 spatial dimensions, a frequency offset dimension, and a respiratory dimension. Images are displayed at unsaturated acquisition S_0, 3.5 ppm and 1.0 ppm (before B_0 correction). Bin 1 and Bin 5 correspond to end-expiration and end inspiration phases respectively.

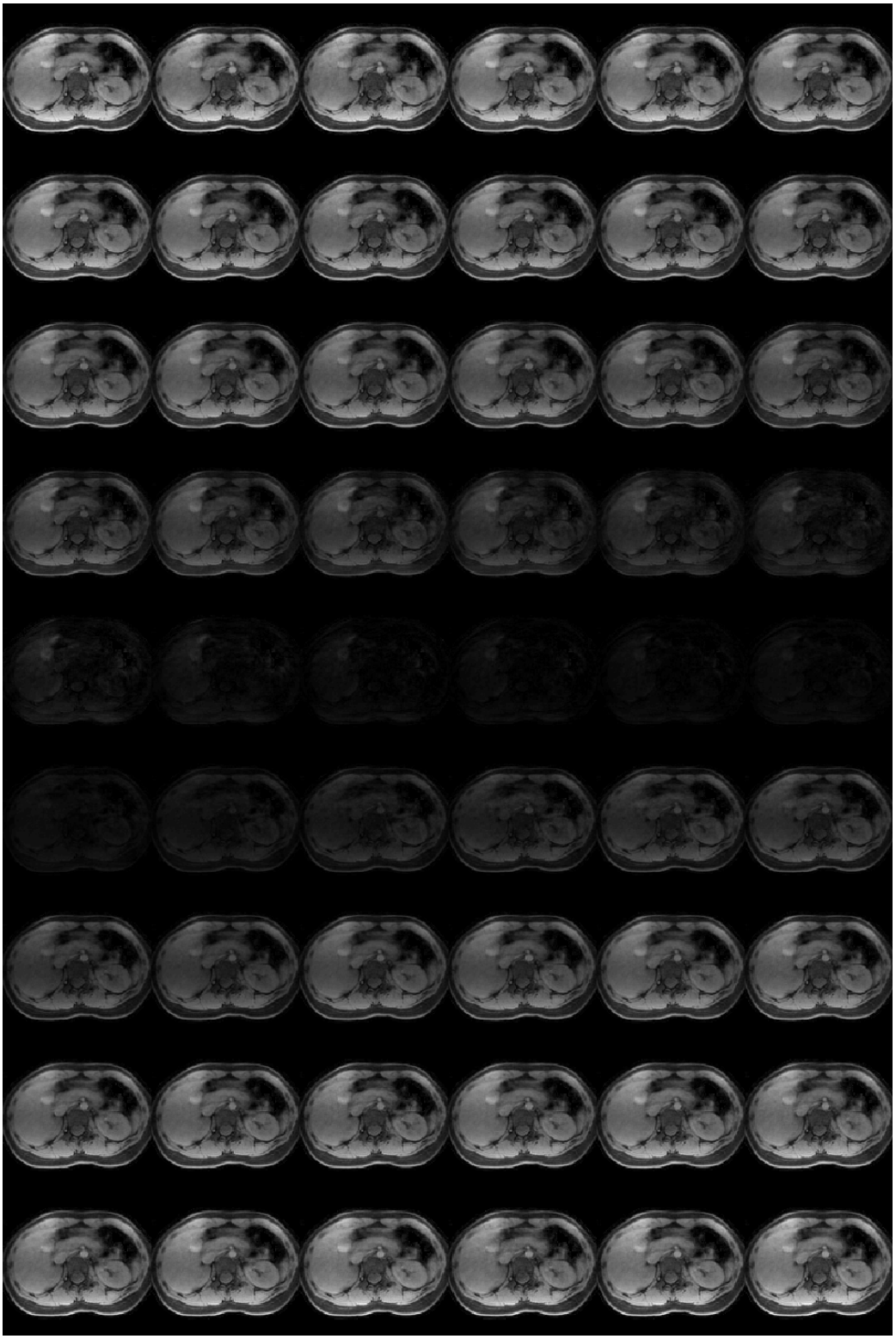

Figure 5.3: CEST images along the whole Z-spectrum from Bin 3 (in which the liver was positioned between end-inspiration and end-expiration phases) before B_0 correction, including the unsaturated one and 53 different frequency offsets from -40 to 40 ppm.

The proposed protocol with free-breathing acquisition was successfully applied to all healthy volunteers. Representative 5D CEST images at steady-state ($\tau = \tau_{\max}$) are shown in **Figure 5.2**. **Figure 5.2a** and **Figure 5.2b** represent respiratory bins corresponding to end-expiration and end inspiration phases respectively. Unsaturated images, CEST images acquired at 3.5 ppm, and CEST images acquired at 1.0 ppm are displayed from left to right.

Figure 5.3 shows all 54 CEST images (including S_0) along the whole Z-spectrum from a specific respiratory phase. In can be seen that the position of the liver is consistent in images of different frequency offsets.

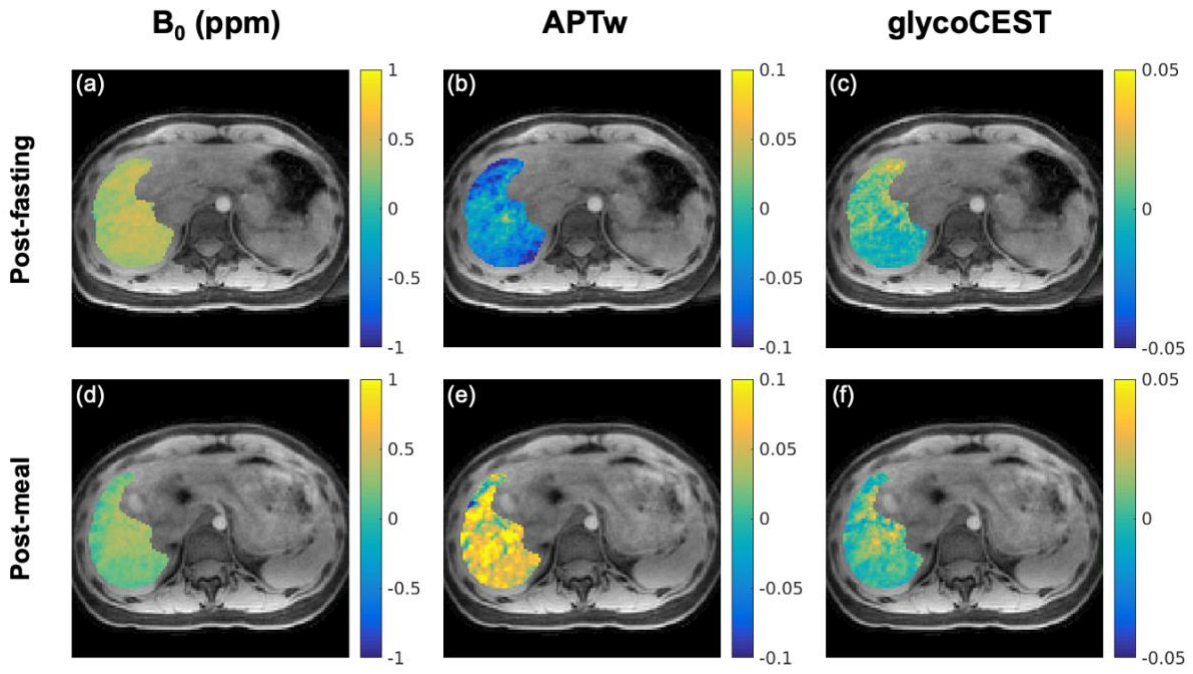

Figure 5.4: Representative B_0, APTw and glycoCEST maps of the liver region at the central slice from **(a-c)** post-fasting scan and **(d-f)** post-meal scan of the same volunteer.

Figure 5.4 presents B_0, APTw (MTR_{asym} at 3.5 ppm), and glycoCEST (MTR_{asym} at 1.0 ppm) maps in post-fasting and post-meal scans of a healthy volunteer. **Figure 5.5** shows the distribution of APTw and glycoCEST MTR_{asym} values within the liver region in the same volunteer.

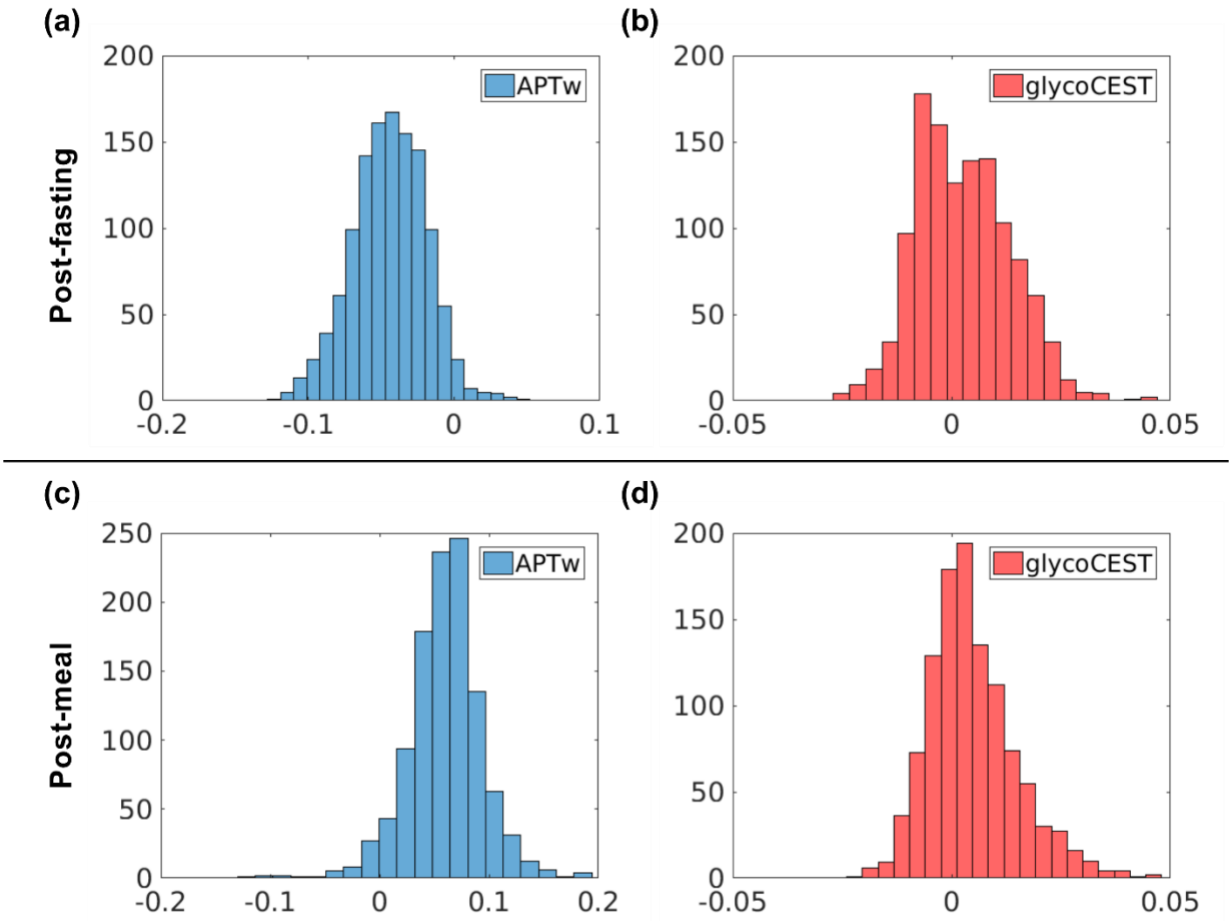

Figure 5.5: Histograms of MTR_{asym} values of APTw and glycoCEST in the same volunteer.

Results of average APTw and glycoCEST measurements from post-fasting and post-meal scans in all subjects are shown in **Figure 5.6a** and **Figure 5.6b** respectively. The upward trends of both APTw and glycoCEST values after meal can be clearly seen in the figure, which is consistent with previous study [54]. In all volunteers, both APTw

and glycoCEST signals from post-mean scans were significantly increased (APTw values: -0.022 ± 0.016 in post-fasting scans, 0.015 ± 0.023 in post-meal scans, $p < 0.02$; glycoCEST values: -0.008 ± 0.018 in post-fasting scans, -0.003 ± 0.065 in post-meal scans, $p < 0.02$).

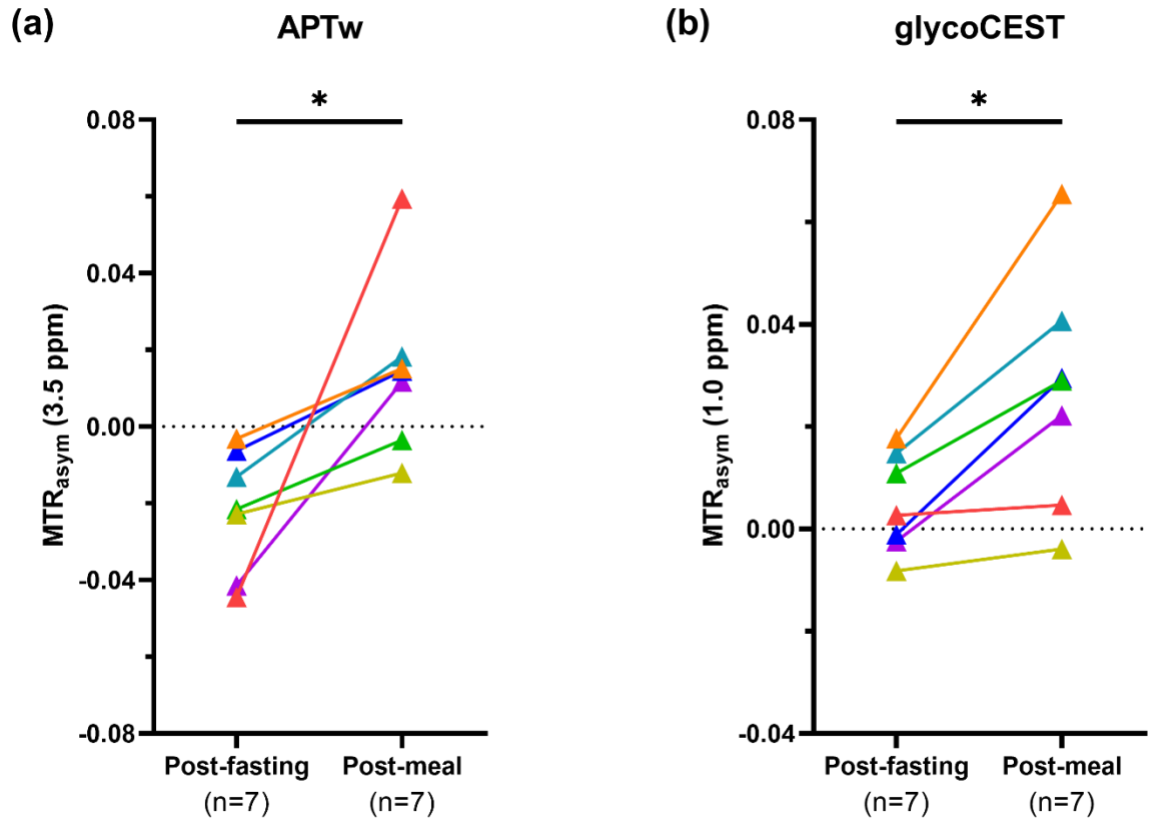

Figure 5.6: Line plot of mean MTR_{asym} values of APTw and glycoCEST in the liver region from post-fasting scans and post-meal scans.

The Bland-Altman plots of APTw and glycoCEST measurements from two intra-session scans are shown in **Figure 5.7a** and **Figure 5.7b** respectively. The 95% limits of agreement of the average APTw signal were -0.050 to 0.062, while the 95% limits of agreement of the average glycoCEST signal were -0.033 to 0.032.

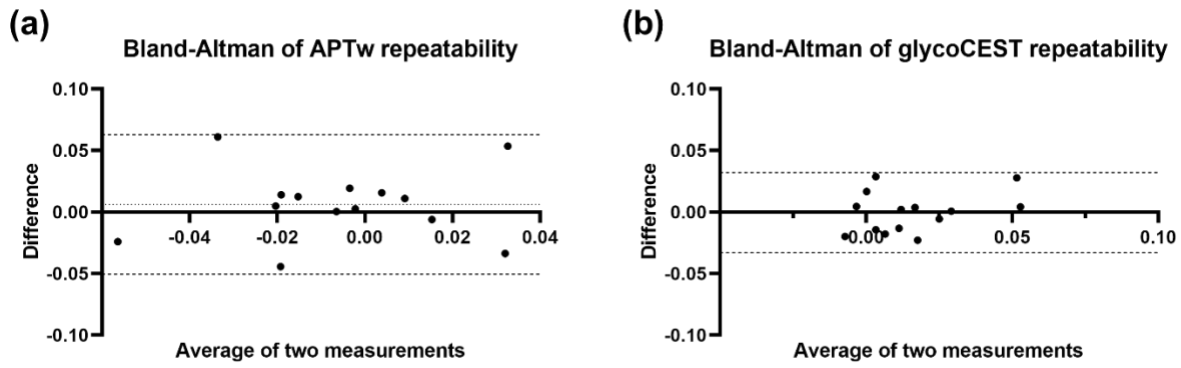

Figure 5.7: Bland-Altman plots for mean MTR_{asym} values of APTw and glycoCEST in two intra-session measurements. The dashed lines show 95% limits of agreement.

5.4 Discussion and conclusion

The Multitasking ss-CEST technique was able to acquire 3D liver CEST images without breath-holds. The in-plane spatial resolution of 2.0 mm was comparable with previous 2D studies [54, 124, 125], while the Multitasking 3D slice coverage of 192 mm was much larger, covering the whole liver.

In this work, k-space data were continuously acquired during free-breathing within the 9-min scan, and all the data were used for image reconstruction. Compared with breath-hold or navigator-gated acquisition, the proposed free-breathing method not only makes it possible to apply 3D abdominal CEST imaging in human studies for the first time, but also greatly improves the acquisition efficiency (equivalent to an 100% gating efficiency). In free-breathing acquisition, data need to be binned into different groups corresponding to real-time respiratory motion states, so that the tensor $\mathcal{D}_{\mathrm{tr}}$ can be correctly completed in the respiratory dimension. Respiratory binning is usually done only using image data (similar to self-gating strategies) in previous MR Multitasking

applications, either directly in the image domain [9] or from real-time temporal weighting functions. However, it is difficult to apply such binning methods in ss-CEST acquisition, because both real-time images and temporal weighting functions show very low signal intensities when the saturation frequency offset is close to 0 ppm. Therefore, the Siemens PMU data was used in our proposed protocol as auxiliary data to finish the respiratory binning process.

Motion handling is still not perfect in the current free-breathing ss-CEST protocol. First, the B_0 field is constantly changing during free-breathing acquisition, which can cause severe B_0 inhomogeneities, especially in the regions close to the liver dome. This will introduce error to final CEST analysis because of incomplete B_0 correction or incorrect modeling of B_0 inhomogeneities in the low-rank model. It can possibly explain those outliers shown in **Figure 5.7**. Advanced active shimming coils may potentially provide better B_0 shimming in future studies. Second, residual motion is still visible in some cases after respiratory binning, which can also introduce error to pixel-wise CEST analysis. This may be addressed in the future by developing more robust binning procedures. Last, the steady-state signal may be less stable, because the tissues at the boundary of the imaging volume are continuously moving in and out. Signal averaging can be used to replace the single time point $\tau = \tau_{\max}$ in Equation (5.5) to lessen this issue.

There are several limitations in this study. First, as an initial technical validation, only healthy volunteers were included in this study, and some variates were not strictly controlled in the fasting experiments (such as diet, actual duration of fasting, etc.). Even though clear upward trends can be seen in both APTw and glycoCEST values after meal for each subject, it is hard to compare among different subjects. Therefore, we are not

able to reach clinical conclusions at this stage from the results of current fasting experiments. Also, a single ROI was drawn in the liver region to report the average APTw and glycoCEST for each volunteer. Analysis was not performed in different sub-regions of the liver to explore possible signal difference of various liver tissues. A more systematic patient study will be performed in the future to investigate potential clinical applications of the proposed protocol.

Future work will also focus on optimizing the saturation power B_1 and developing application-specific frequency offset sampling patterns with clinical validations. Advanced CEST quantification methods, such as multi-pool fitting or the Lorentzian difference method, will also be investigated. Further reduction of total scan time and improvement of the spatial resolution will be explored as well.

In conclusion, the proposed 3D abdominal steady-state CEST method using MR Multitasking can generate CEST images of the entire liver during free breathing. It has the potential to push the liver CEST technique towards practical clinical use.

CHAPTER 6: Conclusions and Future Work

6.1 Summary of the work

In this dissertation, we focus on improvements of two important tissue characterization techniques using MR Multitasking: (1) ECG-free myocardial T1 and ECV mapping in small animals at 9.4 T; (2) Fast 3D CEST imaging for human studies at 3.0 T.

Chapter 3 presented an ECG-free myocardial T1 and ECV mapping technique in small animals at high heart rates. Phantom T1 mapping results from the proposed method showed excellent consistency with the scanner's built-in technique. Its feasibility to characterize diffuse myocardial fibrosis with ECV quantification was validated in a rat HFpEF model.

Chapter 4 introduced a fast whole-brain steady-state CEST method using MR Multitasking. Repeatable APT and rNOE maps with whole-brain coverage and a spatial resolution of 1.7 x 1.7 x 3.0 mm^3 were generated within a total scan time of 5.5 min. The mean amplitudes of APT and rNOE signals were consistent among healthy subjects.

Chapter 5 presented a free-breathing 3D abdominal steady-state CEST method using MR Multitasking. CEST images of 55 frequency offsets with entire-liver coverage and 2.0 x 2.0 x 6.0 mm^3 spatial resolution were generated within 9 min. Both APTw and glycoCEST signals showed high sensitivity between post-fasting and post-meal acquisitions.

6.2 Future directions

In general, we will continue to improve the steady-state CEST imaging technique using MR Multitasking.

6.2.1 Clinical validations

In Chapter 4 and 5, the technical feasibility of the MR Multitasking based steady-state CEST protocol was tested in healthy volunteers. However, there is no patient study in this work. With images of healthy volunteers only, it is hard to determine what specific CEST parameters (such as B_1) would be optimal for clinical diagnosis. Therefore, we are planning to perform future patient studies to further validate the technique and to optimize the imaging parameters.

For brain CEST, glioblastoma (GBM) patients will be recruited for further clinical validation [128, 129, 130]. For abdominal CEST, patients with focal liver lesions can be recruited for clinical validation [125]. CEST imaging has not been validated for the diagnosis of pancreatic ductal adenocarcinoma (PDAC) [131, 132], while it is also a potential application to explore. It can be expected that optimized CEST parameters might be different in different clinical diagnosis scenarios.

6.2.2 Further reduction of scan time

In Chapter 4, we have shown that the GRE based steady-state CEST imaging can be further accelerated using MR Multitasking. With low-rank tensor modeling, the correlations among images acquired at different frequency offsets are exploited to reduce the scan time and enhance the image quality. With the current protocol, CEST images of 55 different frequency offsets can be acquired within 5.5 min, allowing whole-brain coverage at a spatial resolution of 1.7 x 1.7 x 3.0 mm^3.

In the proposed MR Multitasking based ss-CEST protocol, the acceleration of imaging acquisition was achieved by reducing the acquisition time at each frequency offset. In other words, it further undersampled the k-space while maintaining the image

quality, with the help of low-rank tensor modelling. From another point of view, the total CEST scan time is directly proportional to the number of frequency offsets sampled. Therefore, another possible solution to reduce the total imaging time is to obtain CEST maps from undersampled Z-spectrum, i.e., to reduce the number of frequency offsets acquired. Previous studies have used deep learning methods to bypass the traditional CEST analysis methods such asymmetry analysis or multi-pool fitting, either from fully sampled CEST images [134, 135] or undersampled CEST images [136, 137]. Further investigation and exploration will be done towards this direction.

6.2.3 Moving towards free-breathing cardiac CEST imaging

Cardiac CEST techniques have been developed for myocardial tissue characterization in various applications, such as chronic myocardial infarction [138] and amyloid light-chain amyloidosis [139]. Currently, both ECG triggering and navigator gating were used to reduce the effects of cardiac and respiratory motion. However, respiratory phase mismatch can still happen with imperfect navigator gating, which leads to B_0 field variations [138]. In some cases, the navigator gating would completely fail [139]. Moreover, only 30% ~ 40% navigator efficiency can be achieved in successful cases, which reduces the efficiency of data utilization and makes the total scan time unpredictable.

Therefore, development of free-breathing cardiac CEST imaging using the Multitasking based steady-state CEST protocol will also be explored in the future.

REFERENCE

1. Weiskopf N, Edwards LJ, Helms G, Mohammadi S, Kirilina E. Quantitative magnetic resonance imaging of brain anatomy and in vivo histology. Nature Reviews Physics. 2021 Aug;3(8):570-88.

2. Seraphim A, Knott KD, Augusto J, Bhuva AN, Manisty C, Moon JC. Quantitative cardiac MRI. Journal of Magnetic Resonance Imaging. 2020 Mar;51(3):693-711.

3. Christodoulou AG, Shaw JL, Nguyen C, Yang Q, Xie Y, Wang N, Li D. Magnetic resonance multitasking for motion-resolved quantitative cardiovascular imaging. Nature biomedical engineering. 2018 Apr;2(4):215.

4. Shaw JL, Yang Q, Zhou Z, Deng Z, Nguyen C, Li D, Christodoulou AG. Free-breathing, non-ECG, continuous myocardial T1 mapping with cardiovascular magnetic resonance multitasking. Magnetic resonance in medicine. 2019 Apr;81(4):2450-63.

5. Hu Z, Christodoulou AG, Wang N, Shaw JL, Song SS, Maya MM, Ishimori ML, Forbess LJ, Xiao J, Bi X, Han F. Magnetic resonance multitasking for multidimensional assessment of cardiovascular system: Development and feasibility study on the thoracic aorta. Magnetic Resonance in Medicine. 2020 Nov;84(5):2376-88.

6. Nguyen CT, Christodoulou AG, Coll-Font J, Ma S, Xie Y, Reese TG, Mekkaoui C, Lewis GD, Bi X, Sosnovik DE, Li D. Free-breathing diffusion tensor MRI of the whole left ventricle using second-order motion compensation and multitasking respiratory motion correction. Magnetic Resonance in Medicine. 2021 May;85(5):2634-48.

7. Ma S, Nguyen CT, Han F, Wang N, Deng Z, Binesh N, Moser FG, Christodoulou AG, Li D. Three-dimensional simultaneous brain T1, T2, and ADC mapping with MR Multitasking. Magnetic resonance in medicine. 2020 Jul;84(1):72-88.

8. Cao T, Ma S, Wang N, Gharabaghi S, Xie Y, Fan Z, Hogg E, Wu C, Han F, Tagliati M, Haacke EM. Three-dimensional simultaneous brain mapping of T1, T2, and magnetic susceptibility with MR Multitasking. Magnetic Resonance in Medicine. 2022 Mar;87(3):1375-89.

9. Wang N, Gaddam S, Wang L, Xie Y, Fan Z, Yang W, Tuli R, Lo S, Hendifar A, Pandol S, Christodoulou AG. Six-dimensional quantitative DCE MR Multitasking of the entire abdomen: Method and application to pancreatic ductal adenocarcinoma. Magnetic resonance in medicine. 2020 Aug;84(2):928-48.

10. Stemkens B, Tijssen RH, de Senneville BD, Heerkens HD, van Vulpen M, Lagendijk JJ, van den Berg CA. Optimizing 4-dimensional magnetic resonance imaging data

sampling for respiratory motion analysis of pancreatic tumors. International Journal of Radiation Oncology* Biology* Physics. 2015 Mar 1;91(3):571-8.

11. Dasari P, Johnson K, Dey J, Lindsay C, Shazeeb MS, Mukherjee JM, Zheng S, King MA. MRI investigation of the linkage between respiratory motion of the heart and markers on patient's abdomen and chest: Implications for respiratory amplitude binning list-mode PET and SPECT studies. IEEE transactions on nuclear science. 2014 Jan 29;61(1):192-201.

12. De Lathauwer L, De Moor B, Vandewalle J. A multilinear singular value decomposition. SIAM journal on Matrix Analysis and Applications. 2000;21(4):1253-78.

13. Haaf P, Garg P, Messroghli DR, Broadbent DA, Greenwood JP, Plein S. Cardiac T1 mapping and extracellular volume (ECV) in clinical practice: a comprehensive review. Journal of Cardiovascular Magnetic Resonance. 2017 Jan;18(1):89.

14. Kim RJ, Wu E, Rafael A, Chen EL, Parker MA, Simonetti O, Klocke FJ, Bonow RO, Judd RM. The use of contrast-enhanced magnetic resonance imaging to identify reversible myocardial dysfunction. New England Journal of Medicine. 2000 Nov 16;343(20):1445-53.

15. Gulati A, Jabbour A, Ismail TF, Guha K, Khwaja J, Raza S, Morarji K, Brown TD, Ismail NA, Dweck MR, Di Pietro E. Association of fibrosis with mortality and sudden cardiac death in patients with nonischemic dilated cardiomyopathy. Jama. 2013 Mar 6;309(9):896-908.

16. Look DC, Locker DR. Time saving in measurement of NMR and EPR relaxation times. Review of Scientific Instruments. 1970 Feb;41(2):250-1.

17. Messroghli DR, Radjenovic A, Kozerke S, Higgins DM, Sivananthan MU, Ridgway JP. Modified Look-Locker inversion recovery (MOLLI) for high-resolution T1 mapping of the heart. Magnetic resonance in medicine. 2004 Jul;52(1):141-6.

18. Piechnik SK, Ferreira VM, Dall'Armellina E, Cochlin LE, Greiser A, Neubauer S, Robson MD. Shortened Modified Look-Locker Inversion recovery (ShMOLLI) for clinical myocardial T1-mapping at 1.5 and 3 T within a 9 heartbeat breathhold. Journal of cardiovascular magnetic resonance. 2010 Dec;12(1):1-1.

19. Iles L, Pfluger H, Phrommintikul A, Cherayath J, Aksit P, Gupta SN, Kaye DM, Taylor AJ. Evaluation of diffuse myocardial fibrosis in heart failure with cardiac magnetic resonance contrast-enhanced T1 mapping. Journal of the American College of Cardiology. 2008 Nov 4;52(19):1574-80.

20. Ng AC, Auger D, Delgado V, van Elderen SG, Bertini M, Siebelink HM, van der Geest RJ, Bonetti C, van der Velde ET, de Roos A, Smit JW. Association between diffuse myocardial fibrosis by cardiac magnetic resonance contrast-enhanced T1

mapping and subclinical myocardial dysfunction in diabetic patients: a pilot study. Circulation: Cardiovascular Imaging. 2012 Jan;5(1):51-9.

21. Arheden H, Saeed M, Higgins CB, Gao DW, Bremerich J, Wyttenbach R, Dae MW, Wendland MF. Measurement of the distribution volume of gadopentetate dimeglumine at echo-planar MR imaging to quantify myocardial infarction: comparison with 99mTc-DTPA autoradiography in rats. Radiology. 1999 Jun;211(3):698-708.

22. Messroghli DR, Nordmeyer S, Dietrich T, Dirsch O, Kaschina E, Savvatis K, O h-Ici D, Klein C, Berger F, Kuehne T. Assessment of diffuse myocardial fibrosis in rats using small-animal Look-Locker inversion recovery T1 mapping. Circulation: Cardiovascular Imaging. 2011 Nov;4(6):636-40.

23. Everett RJ, Stirrat CG, Semple SI, Newby DE, Dweck MR, Mirsadraee S. Assessment of myocardial fibrosis with T1 mapping MRI. Clinical radiology. 2016 Aug 1;71(8):768-78.

24. Mordi IR, Singh S, Rudd A, Srinivasan J, Frenneaux M, Tzemos N, Dawson DK. Comprehensive echocardiographic and cardiac magnetic resonance evaluation differentiates among heart failure with preserved ejection fraction patients, hypertensive patients, and healthy control subjects. JACC: Cardiovascular Imaging. 2017 Aug 16:2344.

25. Rommel KP, von Roeder M, Latuscynski K, Oberueck C, Blazek S, Fengler K, Besler C, Sandri M, Lücke C, Gutberlet M, Linke A. Extracellular volume fraction for characterization of patients with heart failure and preserved ejection fraction. Journal of the American College of Cardiology. 2016 Apr 19;67(15):1815-25.

26. Su MY, Lin LY, Tseng YH, Chang CC, Wu CK, Lin JL, Tseng WY. CMR-verified diffuse myocardial fibrosis is associated with diastolic dysfunction in HFpEF. JACC: Cardiovascular Imaging. 2014 Oct 1;7(10):991-7.

27. Messroghli DR, Nordmeyer S, Buehrer M, Kozerke S, Dietrich T, Kaschina E, Becher PM, Hucko T, Berger F, Klein C, Kuehne T. Small animal Look-Locker Inversion Recovery (SALLI) for simultaneous generation of cardiac T1 maps and cine and inversion recovery-prepared images at high heart rates: initial experience. Radiology. 2011 Oct;261(1):258-65.

28. Zhang H, Ye Q, Zheng J, Schelbert EB, Hitchens TK, Ho C. Improve myocardial T1 measurement in rats with a new regression model: application to myocardial infarction and beyond. Magnetic resonance in medicine. 2014 Sep;72(3):737-48.

29. Smit H, Guridi RP, Guenoun J, Poot DH, Doeswijk GN, Milanesi M, Bernsen MR, Krestin GP, Klein S, Kotek G. T1 mapping in the rat myocardium at 7 tesla using a modified CINE inversion recovery sequence. Journal of Magnetic Resonance Imaging. 2014 Apr;39(4):901-10.

30. Stäb D, Roessler J, O'Brien K, Hamilton-Craig C, Barth M. ECG triggering in ultra-high field cardiovascular MRI. Tomography. 2016 Sep;2(3):167.

31. Krug JW, Rose G, Clifford GD, Oster J. ECG-based gating in ultra high field cardiovascular magnetic resonance using an independent component analysis approach. Journal of Cardiovascular Magnetic Resonance. 2013 Dec 1;15(1):104.

32. Van Zijl PC, Yadav NN. Chemical exchange saturation transfer (CEST): what is in a name and what isn't?. Magnetic resonance in medicine. 2011 Apr;65(4):927-48.

33. Wu B, Warnock G, Zaiss M, Lin C, Chen M, Zhou Z, Mu L, Nanz D, Tuura R, Delso G. An overview of CEST MRI for non-MR physicists. EJNMMI physics. 2016 Dec;3(1):1-21.

34. Ward KM, Aletras AH, Balaban RS. A new class of contrast agents for MRI based on proton chemical exchange dependent saturation transfer (CEST). Journal of magnetic resonance. 2000 Mar 1;143(1):79-87.

35. Khlebnikov V, Geades N, Klomp DW, Hoogduin H, Gowland P, Mougin O. Comparison of pulsed three-dimensional CEST acquisition schemes at 7 tesla: steady state versus pseudosteady state. Magnetic resonance in medicine. 2017 Jun;77(6):2280-7.

36. Zhou J, Payen JF, Wilson DA, Traystman RJ, van Zijl PC. Using the amide proton signals of intracellular proteins and peptides to detect pH effects in MRI. Nature medicine. 2003 Aug;9(8):1085-90.

37. Zhou J, Heo HY, Knutsson L, van Zijl PC, Jiang S. APT-weighted MRI: Techniques, current neuro applications, and challenging issues. Journal of Magnetic Resonance Imaging. 2019 Aug;50(2):347-64.

38. Jiang S, Eberhart CG, Zhang Y, Heo HY, Wen Z, Blair L, Qin H, Lim M, Quinones-Hinojosa A, Weingart JD, Barker PB. Amide proton transfer-weighted magnetic resonance image-guided stereotactic biopsy in patients with newly diagnosed gliomas. European Journal of Cancer. 2017 Sep 1;83:9-18.

39. Togao O, Hiwatashi A, Yamashita K, Kikuchi K, Keupp J, Yoshimoto K, Kuga D, Yoneyama M, Suzuki SO, Iwaki T, Takahashi M. Grading diffuse gliomas without intense contrast enhancement by amide proton transfer MR imaging: comparisons with diffusion-and perfusion-weighted imaging. European radiology. 2017 Feb;27(2):578-88.

40. Choi YS, Ahn SS, Lee SK, Chang JH, Kang SG, Kim SH, Zhou J. Amide proton transfer imaging to discriminate between low-and high-grade gliomas: added value to apparent diffusion coefficient and relative cerebral blood volume. European radiology. 2017 Aug;27(8):3181-9.

41. Zou T, Yu H, Jiang C, Wang X, Jiang S, Rui Q, Mei Y, Zhou J, Wen Z. Differentiating the histologic grades of gliomas preoperatively using amide proton transfer-weighted (APTW) and intravoxel incoherent motion MRI. NMR in Biomedicine. 2018 Jan;31(1):e3850.

42. Yao J, Chakhoyan A, Nathanson DA, Yong WH, Salamon N, Raymond C, Mareninov S, Lai A, Nghiemphu PL, Prins RM, Pope WB. Metabolic characterization of human IDH mutant and wild type gliomas using simultaneous pH-and oxygen-sensitive molecular MRI. Neuro-oncology. 2019 Sep 6;21(9):1184-96.

43. Zhou J, Tryggestad E, Wen Z, Lal B, Zhou T, Grossman R, Wang S, Yan K, Fu DX, Ford E, Tyler B. Differentiation between glioma and radiation necrosis using molecular magnetic resonance imaging of endogenous proteins and peptides. Nature medicine. 2011 Jan;17(1):130-4.

44. Jiang S, Yu H, Wang X, Lu S, Li Y, Feng L, Zhang Y, Heo HY, Lee DH, Zhou J, Wen Z. Molecular MRI differentiation between primary central nervous system lymphomas and high-grade gliomas using endogenous protein-based amide proton transfer MR imaging at 3 Tesla. European radiology. 2016 Jan;26(1):64-71.

45. Park JE, Kim HS, Park KJ, Kim SJ, Kim JH, Smith SA. Pre-and posttreatment glioma: comparison of amide proton transfer imaging with MR spectroscopy for biomarkers of tumor proliferation. Radiology. 2016 Feb;278(2):514-23.

46. Desmond KL, Mehrabian H, Chavez S, Sahgal A, Soliman H, Rola R, Stanisz GJ. Chemical exchange saturation transfer for predicting response to stereotactic radiosurgery in human brain metastasis. Magnetic resonance in medicine. 2017 Sep;78(3):1110-20.

47. Jokivarsi KT, Gröhn HI, Gröhn OH, Kauppinen RA. Proton transfer ratio, lactate, and intracellular pH in acute cerebral ischemia. Magnetic Resonance in Medicine. 2007 Apr;57(4):647-53.

48. Sun PZ, Wang E, Cheung JS. Imaging acute ischemic tissue acidosis with pH-sensitive endogenous amide proton transfer (APT) MRI—correction of tissue relaxation and concomitant RF irradiation effects toward mapping quantitative cerebral tissue pH. Neuroimage. 2012 Mar 1;60(1):1-6.

49. Zong X, Wang P, Kim SG, Jin T. Sensitivity and source of amine-proton exchange and amide-proton transfer magnetic resonance imaging in cerebral ischemia. Magnetic resonance in medicine. 2014 Jan;71(1):118-32.

50. Guo Y, Zhou IY, Chan ST, Wang Y, Mandeville ET, Igarashi T, Lo EH, Ji X, Sun PZ. pH-sensitive MRI demarcates graded tissue acidification during acute stroke—pH specificity enhancement with magnetization transfer and relaxation-normalized amide proton transfer (APT) MRI. Neuroimage. 2016 Nov 1;141:242-9.

51. Lin G, Zhuang C, Shen Z, Xiao G, Chen Y, Shen Y, Zong X, Wu R. APT weighted MRI as an effective imaging protocol to predict clinical outcome after acute ischemic stroke. Frontiers in neurology. 2018:901.

52. Van Zijl PC, Jones CK, Ren J, Malloy CR, Sherry AD. MRI detection of glycogen in vivo by using chemical exchange saturation transfer imaging (glycoCEST). Proceedings of the National Academy of Sciences. 2007 Mar 13;104(11):4359-64.

53. Chen SZ, Yuan J, Deng M, Wei J, Zhou J, Wáng YX. Chemical exchange saturation transfer (CEST) MR technique for in-vivo liver imaging at 3.0 tesla. European radiology. 2016 Jun;26(6):1792-800.

54. Deng M, Chen SZ, Yuan J, Chan Q, Zhou J, Wáng YX. Chemical exchange saturation transfer (CEST) MR technique for liver imaging at 3.0 Tesla: an evaluation of different offset number and an after-meal and over-night-fast comparison. Molecular imaging and biology. 2016 Apr;18(2):274-82.

55. Zhou Y, van Zijl PC, Xu X, Xu J, Li Y, Chen L, Yadav NN. Magnetic resonance imaging of glycogen using its magnetic coupling with water. Proceedings of the National Academy of Sciences. 2020 Feb 11;117(6):3144-9.

56. Ling W, Regatte RR, Navon G, Jerschow A. Assessment of glycosaminoglycan concentration in vivo by chemical exchange-dependent saturation transfer (gagCEST). Proceedings of the National Academy of Sciences. 2008 Feb 19;105(7):2266-70.

57. Krishnamoorthy G, Nanga RP, Bagga P, Hariharan H, Reddy R. High quality three-dimensional gagCEST imaging of in vivo human knee cartilage at 7 Tesla. Magnetic resonance in medicine. 2017 May;77(5):1866-73.

58. Watkins LE, Rubin EB, Mazzoli V, Uhlrich SD, Desai AD, Black M, Ho GK, Delp SL, Levenston ME, Beaupré GS, Gold GE. Rapid volumetric gagCEST imaging of knee articular cartilage at 3 T: evaluation of improved dynamic range and an osteoarthritic population. NMR in Biomedicine. 2020 Aug;33(8):e4310.

59. Haneder S, Apprich SR, Schmitt B, Michaely HJ, Schoenberg SO, Friedrich KM, Trattnig S. Assessment of glycosaminoglycan content in intervertebral discs using chemical exchange saturation transfer at 3.0 Tesla: preliminary results in patients with low-back pain. European radiology. 2013 Mar;23(3):861-8.

60. Liu Q, Tawackoli W, Pelled G, Fan Z, Jin N, Natsuaki Y, Bi X, Gart A, Bae H, Gazit D, Li D. Detection of low back pain using pH level-dependent imaging of the intervertebral disc using the ratio of R1ρ dispersion and −OH chemical exchange saturation transfer (RROC). Magnetic resonance in medicine. 2015 Mar;73(3):1196-205.

61. Bez M, Zhou Z, Sheyn D, Tawackoli W, Giaconi JC, Shapiro G, Ben David S, Gazit Z, Pelled G, Li D, Gazit D. Molecular pain markers correlate with pH-sensitive MRI signal in a pig model of disc degeneration. Scientific reports. 2018 Nov 26;8(1):1-11.

62. Pelled G, Salas MM, Han P, Gill HE, Lautenschlager KA, Lai TT, Shawver CM, Hoch MB, Goff BJ, Betts AM, Zhou Z. Intradiscal quantitative chemical exchange saturation transfer MRI signal correlates with discogenic pain in human patients. Scientific Reports. 2021 Sep 28;11(1):1-9.

63. Zaiss M, Schmitt B, Bachert P. Quantitative separation of CEST effect from magnetization transfer and spillover effects by Lorentzian-line-fit analysis of z-spectra. Journal of magnetic resonance. 2011 Aug 1;211(2):149-55.

64. Desmond KL, Moosvi F, Stanisz GJ. Mapping of amide, amine, and aliphatic peaks in the CEST spectra of murine xenografts at 7 T. Magnetic resonance in medicine. 2014 May;71(5):1841-53.

65. Heo HY, Zhang Y, Lee DH, Hong X, Zhou J. Quantitative assessment of amide proton transfer (APT) and nuclear overhauser enhancement (NOE) imaging with extrapolated semi-solid magnetization transfer reference (EMR) signals: application to a rat glioma model at 4.7 Tesla. Magnetic resonance in medicine. 2016 Jan;75(1):137-49.

66. Zaiss M, Ehses P, Scheffler K. Snapshot-CEST: optimizing spiral-centric-reordered gradient echo acquisition for fast and robust 3D CEST MRI at 9.4 T. NMR in Biomedicine. 2018 Apr;31(4):e3879.

67. Deshmane A, Zaiss M, Lindig T, Herz K, Schuppert M, Gandhi C, Bender B, Ernemann U, Scheffler K. 3D gradient echo snapshot CEST MRI with low power saturation for human studies at 3T. Magnetic resonance in medicine. 2019 Apr;81(4):2412-23.

68. Mueller S, Stirnberg R, Akbey S, Ehses P, Scheffler K, Stöcker T, Zaiss M. Whole brain snapshot CEST at 3T using 3D-EPI: Aiming for speed, volume, and homogeneity. Magnetic resonance in medicine. 2020 Nov;84(5):2469-83.

69. Jones CK, Polders D, Hua J, Zhu H, Hoogduin HJ, Zhou J, Luijten P, Van Zijl PC. In vivo three-dimensional whole-brain pulsed steady-state chemical exchange saturation transfer at 7 T. Magnetic resonance in medicine. 2012 Jun;67(6):1579-89.

70. Jones CK, Huang A, Xu J, Edden RA, Schär M, Hua J, Oskolkov N, Zacà D, Zhou J, McMahon MT, Pillai JJ. Nuclear Overhauser enhancement (NOE) imaging in the human brain at 7 T. Neuroimage. 2013 Aug 15;77:114-24.

71. Heo HY, Jones CK, Hua J, Yadav N, Agarwal S, Zhou J, van Zijl PC, Pillai JJ. Whole-brain amide proton transfer (APT) and nuclear Overhauser enhancement (NOE) imaging in glioma patients using low-power steady-state pulsed chemical exchange saturation transfer (CEST) imaging at 7T. Journal of Magnetic Resonance Imaging. 2016 Jul;44(1):41-50.

72. Sui R, Chen L, Li Y, Huang J, Chan KW, Xu X, van Zijl PC, Xu J. Whole-brain amide CEST imaging at 3T with a steady-state radial MRI acquisition. Magnetic resonance in medicine. 2021 Aug;86(2):893-906.

73. Chen L, Cao S, Koehler RC, van Zijl PC, Xu J. High-sensitivity CEST mapping using a spatiotemporal correlation-enhanced method. Magnetic resonance in medicine. 2020 Dec;84(6):3342-50.

74. Lee H, Choi SH, Sohn CH, Kim SG, Lee J, Park J. Rapid three-dimensional steady-state chemical exchange saturation transfer magnetic resonance imaging. Magnetic resonance in medicine. 2021 Mar;85(3):1209-21.

75. Moon JC, Messroghli DR, Kellman P, Piechnik SK, Robson MD, Ugander M, Gatehouse PD, Arai AE, Friedrich MG, Neubauer S, Schulz-Menger J. Myocardial T1 mapping and extracellular volume quantification: A Society for Cardiovascular Magnetic Resonance (SCMR) and CMR Working Group of the European Society of Cardiology consensus statement. Journal of Cardiovascular Magnetic Resonance. 2013 Dec;15(1):92.

76. Puntmann VO, Peker E, Chandrashekhar Y, Nagel E. T1 mapping in characterizing myocardial disease: a comprehensive review. Circulation research. 2016 Jul 8;119(2):277-99.

77. Coolen BF, Geelen T, Paulis LE, Nauerth A, Nicolay K, Strijkers GJ. Three-dimensional T1 mapping of the mouse heart using variable flip angle steady-state MR imaging. NMR in biomedicine. 2011 Feb;24(2):154-62.

78. Doi R, Masuyama T, Yamamoto K, Doi Y, Mano T, Sakata Y, Ono K, Kuzuya T, Hirota S, Koyama T, Miwa T. Development of different phenotypes of hypertensive heart failure: systolic versus diastolic failure in Dahl salt-sensitive rats. Journal of hypertension. 2000 Jan 1;18(1):111-20.

79. Klotz S, Hay I, Zhang G, Maurer M, Wang J, Burkhoff D. Development of heart failure in chronic hypertensive Dahl rats: focus on heart failure with preserved ejection fraction. Hypertension. 2006 May 1;47(5):901-11.

80. Cho JH, Zhang R, Kilfoil PJ, Gallet R, de Couto G, Bresee C, Goldhaber JI, Marbán E, Cingolani E. Delayed repolarization underlies ventricular arrhythmias in rats with heart failure and preserved ejection fraction. Circulation. 2017 Nov 21;136(21):2037-50.

81. Hogg K, Swedberg K, McMurray J. Heart failure with preserved left ventricular systolic function: epidemiology, clinical characteristics, and prognosis. Journal of the American College of Cardiology. 2004 Feb 4;43(3):317-27.

82. Owan TE, Hodge DO, Herges RM, Jacobsen SJ, Roger VL, Redfield MM. Trends in prevalence and outcome of heart failure with preserved ejection fraction. New England Journal of Medicine. 2006 Jul 20;355(3):251-9.

83. Shah KS, Xu H, Matsouaka RA, Bhatt DL, Heidenreich PA, Hernandez AF, Devore AD, Yancy CW, Fonarow GC. Heart failure with preserved, borderline, and reduced ejection fraction: 5-year outcomes. Journal of the American College of Cardiology. 2017 Nov 13;70(20):2476-86.

84. Gallet R, de Couto G, Simsolo E, Valle J, Sun B, Liu W, Tseliou E, Zile MR, Marbán E. Cardiosphere-derived cells reverse heart failure with preserved ejection fraction in rats by decreasing fibrosis and inflammation. JACC: Basic to Translational Science. 2016 Mar 2;1(1-2):14-28.

85. Liang ZP. Spatiotemporal imaging with partially separable functions. In 2007 4th IEEE International Symposium on Biomedical Imaging: From Nano to Macro 2007 Apr 12 (pp. 988-991). IEEE.

86. Kolda TG, Bader BW. Tensor decompositions and applications. SIAM review. 2009 Aug 6;51(3):455-500.

87. Lustig M, Donoho D, Pauly JM. Sparse MRI: The application of compressed sensing for rapid MR imaging. Magnetic resonance in medicine. 2007 Dec;58(6):1182-95.

88. Wolf CM, Moskowitz IP, Arno S, Branco DM, Semsarian C, Bernstein SA, Peterson M, Maida M, Morley GE, Fishman G, Berul CI. Somatic events modify hypertrophic cardiomyopathy pathology and link hypertrophy to arrhythmia. Proceedings of the National Academy of Sciences. 2005 Dec 13;102(50):18123-8.

89. Grigorian-Shamagian L, Liu W, Fereydooni S, Middleton RC, Valle J, Cho JH, Marbán E. Cardiac and systemic rejuvenation after cardiosphere-derived cell therapy in senescent rats. European heart journal. 2017 Oct 14;38(39):2957-67.

90. Vandsburger MH, Janiczek RL, Xu Y, French BA, Meyer CH, Kramer CM, Epstein FH. Improved arterial spin labeling after myocardial infarction in mice using cardiac and respiratory gated look-locker imaging with fuzzy C-means clustering. Magnetic resonance in medicine. 2010 Mar;63(3):648-57.

91. Li W, Griswold M, Yu X. Rapid T1 mapping of mouse myocardium with saturation recovery look-locker method. Magnetic resonance in medicine. 2010 Nov;64(5):1296-303.

92. Kim PK, Hong YJ, Sakuma H, Chawla A, Park JK, Park CH, Hong D, Han K, Lee JY, Hur J, Lee HJ. Myocardial extracellular volume fraction and change in hematocrit level: MR evaluation by using T1 mapping in an experimental model of anemia. Radiology. 2018 Jul;288(1):93-8.

93. Arheden H, Saeed M, Higgins CB, Gao DW, Ursell PC, Bremerich J, Wyttenbach R, Dae MW, Wendland MF. Reperfused rat myocardium subjected to various durations of ischemia: estimation of the distribution volume of contrast material with echo-planar MR imaging. Radiology. 2000 May;215(2):520-8.

94. Christodoulou AG, Wu YL, Hitchens TK, Ho C, Liang ZP. Self-navigated low-rank MRI for MPIO-labeled immune cell imaging of the heart. In2014 36th Annual International Conference of the IEEE Engineering in Medicine and Biology Society 2014 Aug 26 (pp. 1529-1532). IEEE.

95. Serry FM, Ma S, Mao X, Han F, Xie Y, Han H, Li D, Christodoulou AG. Dual flip-angle IR-FLASH with spin history mapping for B1+ corrected T1 mapping: Application to T1 cardiovascular magnetic resonance multitasking. Magnetic resonance in medicine. 2021 Dec;86(6):3182-91.

96. Vinogradov E, Sherry AD, Lenkinski RE. CEST: from basic principles to applications, challenges and opportunities. Journal of magnetic resonance. 2013 Apr 1;229:155-72.

97. Jones KM, Pollard AC, Pagel MD. Clinical applications of chemical exchange saturation transfer (CEST) MRI. Journal of Magnetic Resonance Imaging. 2018 Jan;47(1):11-27.

98. Jones CK, Schlosser MJ, Van Zijl PC, Pomper MG, Golay X, Zhou J. Amide proton transfer imaging of human brain tumors at 3T. Magnetic resonance in medicine. 2006 Sep;56(3):585-92.

99. Longo DL, Cutrin JC, Michelotti F, Irrera P, Aime S. Noninvasive evaluation of renal pH homeostasis after ischemia reperfusion injury by CEST-MRI. NMR in Biomedicine. 2017 Jul;30(7):e3720.

100. Donahue MJ, Donahue PC, Rane S, Thompson CR, Strother MK, Scott AO, Smith SA. Assessment of lymphatic impairment and interstitial protein accumulation in patients with breast cancer treatment-related lymphedema using CEST MRI. Magnetic resonance in medicine. 2016 Jan;75(1):345-55.

101. Haris M, Nanga RP, Singh A, Cai K, Kogan F, Hariharan H, Reddy R. Exchange rates of creatine kinase metabolites: feasibility of imaging creatine by chemical exchange saturation transfer MRI. NMR in Biomedicine. 2012 Nov;25(11):1305-9.

102. Haase A. Snapshot FLASH MRI. Applications to T1, T2, and chemical-shift imaging. Magnetic resonance in medicine. 1990 Jan;13(1):77-89.

103. Breuer FA, Blaimer M, Heidemann RM, Mueller MF, Griswold MA, Jakob PM. Controlled aliasing in parallel imaging results in higher acceleration (CAIPIRINHA) for multi-slice imaging. Magnetic resonance in medicine. 2005 Mar;53(3):684-91.

104. Christodoulou AG, Shaw JL, Nguyen C, Yang Q, Xie Y, Wang N, Li D. Magnetic resonance multitasking for motion-resolved quantitative cardiovascular imaging. Nature Biomedical Engineering. 2018 Apr;2(4):215-226.

105. Liang ZP. Spatiotemporal imaging with partially separable functions. In Biomedical Imaging: From Nano to Macro, 2007. ISBI 2007. 4th IEEE International Symposium on 2007 Apr 12 (pp. 988-991). IEEE.

106. Han P, Zhang R, Wagner S, Xie Y, Cingolani E, Marban E, Christodoulou AG, Li D. Electrocardiogram-less, free-breathing myocardial extracellular volume fraction mapping in small animals at high heart rates using motion-resolved cardiovascular magnetic reesonance multitasking: a feasibility study in a heart failure with preserved ejection fraction rat model. Journal of Cardiovascular Magnetic Resonance. 2021 Feb;23(8):1-11.

107. Ma S, Wang N, Fan Z, Kaisey M, Sicotte NL, Christodoulou AG, Li D. Three-dimensional whole-brain simultaneous T1, T2, and T1ρ quantification using MR Multitasking: Method and initial clinical experience in tissue characterization of multiple sclerosis. Magnetic resonance in medicine. 2021 Apr;85(4):1938-52.

108. Wang N, Xie Y, Fan Z, Ma S, Saouaf R, Guo Y, Shiao SL, Christodoulou AG, Li D. Five-dimensional quantitative low-dose Multitasking dynamic contrast-enhanced MRI: Preliminary study on breast cancer. Magnetic resonance in medicine. 2021 Jun;85(6):3096-111.

109. Kim M, Gillen J, Landman BA, Zhou J, Van Zijl PC. Water saturation shift referencing (WASSR) for chemical exchange saturation transfer (CEST) experiments. Magnetic resonance in medicine. 2009 Jun;61(6):1441-50.

110. Zu Z, Li K, Janve VA, Does MD, Gochberg DF. Optimizing pulsed-chemical exchange saturation transfer imaging sequences. Magnetic resonance in medicine. 2011 Oct;66(4):1100-8.

111. Jenkinson M, Beckmann CF, Behrens TE, Woolrich MW, Smith SM. Fsl. Neuroimage. 2012 Aug 15;62(2):782-90.

112. Synek V. Evaluation of the standard deviation from duplicate results. Accreditation and quality assurance. 2008 Jun;13(6):335-7.

113. Krishnamoorthy G, Nanga RP, Bagga P, Hariharan H, Reddy R. High quality three-dimensional gagCEST imaging of in vivo human knee cartilage at 7 Tesla. Magnetic resonance in medicine. 2017 May;77(5):1866-73.

114. Lam F, Liang ZP. A subspace approach to high-resolution spectroscopic imaging. Magnetic resonance in medicine. 2014 Apr;71(4):1349-57.

115. Zhang T, Pauly JM, Levesque IR. Accelerating parameter mapping with a locally low rank constraint. Magnetic resonance in medicine. 2015 Feb;73(2):655-61.

116. Han H, Song AW, Truong TK. Integrated parallel reception, excitation, and shimming (iPRES). Magnetic resonance in medicine. 2013 Jul;70(1):241-7.

117. Cai Y, Yang H, Li X, Hu T, Huang Y, Shan Y, Lu M, Liu WS, Li D, Han H. Optimization of Multi-Coil Array Design for Efficient Human Brain Shimming at 3T. In Proceedings of the 28th Annual Meeting of ISMRM 2020 (p. 4229).

118. Windschuh J, Zaiss M, Meissner JE, Paech D, Radbruch A, Ladd ME, Bachert P. Correction of B1-inhomogeneities for relaxation-compensated CEST imaging at 7 T. NMR in biomedicine. 2015 May;28(5):529-37.

119. Schuenke P, Windschuh J, Roeloffs V, Ladd ME, Bachert P, Zaiss M. Simultaneous mapping of water shift and B1 (WASABI)—Application to field-inhomogeneity correction of CEST MRI data. Magnetic resonance in medicine. 2017 Feb;77(2):571-80.

120. Goerke S, Soehngen Y, Deshmane A, Zaiss M, Breitling J, Boyd PS, Herz K, Zimmermann F, Klika KD, Schlemmer HP, Paech D. Relaxation-compensated APT and rNOE CEST-MRI of human brain tumors at 3 T. Magnetic resonance in medicine. 2019 Aug;82(2):622-32.

121. Akbey S, Ehses P, Stirnberg R, Zaiss M, Stöcker T. Whole-brain snapshot CEST imaging at 7 T using 3D-EPI. Magnetic resonance in medicine. 2019 Nov;82(5):1741-52.

122. Chen L, Barker PB, Weiss RG, van Zijl PC, Xu J. Creatine and phosphocreatine mapping of mouse skeletal muscle by a polynomial and Lorentzian line-shape fitting CEST method. Magnetic resonance in medicine. 2019 Jan;81(1):69-78.

123. Heo HY, Zhang Y, Jiang S, Lee DH, Zhou J. Quantitative assessment of amide proton transfer (APT) and nuclear overhauser enhancement (NOE) imaging with extrapolated semisolid magnetization transfer reference (EMR) signals: II. Comparison of three EMR models and application to human brain glioma at 3 Tesla. Magnetic resonance in medicine. 2016 Apr;75(4):1630-9.

124. Cai K, Singh A, Grasley K, Haris M, Reddy D, Hariharan H, Reddy R. CEST MRI of Human Liver at 3T. In Proceedings of the 19th Annual Meeting of ISMRM, 2011 (p. 2773).

125. Seo N, Jeong HK, Choi JY, Park MS, Kim MJ, Chung YE. Liver MRI with amide proton transfer imaging: feasibility and accuracy for the characterization of focal liver lesions. European Radiology. 2021 Jan;31(1):222-31.

126. Tang Y, Xiao G, Shen Z, Zhuang C, Xie Y, Zhang X, Yang Z, Guan J, Shen Y, Chen Y, Lai L. Noninvasive detection of extracellular pH in human benign and malignant liver tumors using CEST MRI. Frontiers in oncology. 2020:2349.

127. Chen M, Chen C, Shen Z, Zhang X, Chen Y, Lin F, Ma X, Zhuang C, Mao Y, Gan H, Chen P. Extracellular pH is a biomarker enabling detection of breast cancer and liver cancer using CEST MRI. Oncotarget. 2017 Jul 11;8(28):45759.

128. Zaiss M, Windschuh J, Paech D, Meissner JE, Burth S, Schmitt B, Kickingereder P, Wiestler B, Wick W, Bendszus M, Schlemmer HP. Relaxation-compensated CEST-MRI of the human brain at 7 T: unbiased insight into NOE and amide signal changes in human glioblastoma. Neuroimage. 2015 May 15;112:180-8.

129. Regnery S, Adeberg S, Dreher C, Oberhollenzer J, Meissner JE, Goerke S, Windschuh J, Deike-Hofmann K, Bickelhaupt S, Zaiss M, Radbruch A. Chemical exchange saturation transfer MRI serves as predictor of early progression in glioblastoma patients. Oncotarget. 2018 Jun 19;9(47):28772.

130. Yao J, Tan CH, Schlossman J, Chakhoyan A, Raymond C, Pope WB, Salamon N, Lai A, Ji M, Nghiemphu PL, Liau LM. pH-weighted amine chemical exchange saturation transfer echoplanar imaging (CEST-EPI) as a potential early biomarker for bevacizumab failure in recurrent glioblastoma. Journal of neuro-oncology. 2019 May;142(3):587-95.

131. Farr N, Wang YN, D'Andrea S, Gravelle KM, Hwang JH, Lee D. Noninvasive characterization of pancreatic tumor mouse models using magnetic resonance imaging. Cancer medicine. 2017 May;6(5):1082-90.

132. Gao J, Huang X, Meng H, Zhang M, Zhang X, Lin X, Li B. Performance of multiparametric functional imaging and texture analysis in predicting synchronous metastatic disease in pancreatic ductal adenocarcinoma patients by hybrid PET/MR: initial experience. Frontiers in oncology. 2020 Feb 25;10:198.

133. Han P, Cheema K, Lee HL, Zhou Z, Cao T, Ma S, Wang N, Han H, Christodoulou AG, Li D. Whole-brain steady-state CEST at 3 T using MR Multitasking. Magnetic Resonance in Medicine. 2022 May;87(5):2363-71.

134. Huang J, Lai JH, Tse KH, Cheng GW, Liu Y, Chen Z, Han X, Chen L, Xu J, Chan KW. Deep neural network based CEST and AREX processing: Application in imaging a model of Alzheimer's disease at 3 T. Magnetic Resonance in Medicine. 2022 Mar;87(3):1529-45.

135. Chen L, Schär M, Chan KW, Huang J, Wei Z, Lu H, Qin Q, Weiss RG, van Zijl P, Xu J. In vivo imaging of phosphocreatine with artificial neural networks. Nature communications. 2020 Feb 26;11(1):1-10.

136. Li Y, Xie D, Cember A, Nanga RP, Yang H, Kumar D, Hariharan H, Bai L, Detre JA, Reddy R, Wang Z. Accelerating GluCEST imaging using deep learning for B0 correction. Magnetic resonance in medicine. 2020 Oct;84(4):1724-33.

137. Cheema K, Han P, Christodoulou AG, Xie Y, Li D. Amide Proton Transfer (APT) Mapping from Undersampled Z-spectra in the Brain Using Deep Learning. In Proceedings of the 30th Annual Meeting of ISMRM 2022 (p. 2524).

138. Zhou Z, Nguyen C, Chen Y, Shaw JL, Deng Z, Xie Y, Dawkins J, Marbán E, Li D. Optimized CEST cardiovascular magnetic resonance for assessment of metabolic activity in the heart. Journal of cardiovascular magnetic resonance. 2017 Dec;19(1):1-7.

139. Li X, Huang S, Han P, Zhou Z, Azab L, Lu M, Li J, An J, Cao Y, Jin Z, Li D. Nonenhanced Chemical Exchange Saturation Transfer Cardiac Magnetic Resonance Imaging in Patients With Amyloid Light-Chain Amyloidosis. Journal of Magnetic Resonance Imaging. 2022 Feb;55(2):567-76.